DISSERTATION

2-D D-BAR CONDUCTIVITY RECONSTRUCTIONS ON NON-CIRCULAR DOMAINS

Submitted by

Ethan Kane Murphy

Department of Mathematics

In partial fulfillment of the requirements

for the degree of Doctor of Philosophy

Colorado State University

Fort Collins, Colorado

Fall 2007

COLORADO STATE UNIVERSITY

October 25, 2007

WE HEREBY RECOMMEND THAT THE DISSERTATION PREPARED UNDER OUR SUPERVISION BY ETHAN MURPHY ENTITLED "2-D D-BAR CONDUCTIVITY RECONSTRUCTIONS ON NON-CIRCULAR DOMAINS" BE ACCEPTED AS FULFILLING IN PART REQUIREMENTS FOR THE DEGREE OF DOCTOR OF PHILOSOPHY.

Committee on Graduate Work

Dr. Paul Duchateau

Dr. Michael Kirby

Dr. Xianghong Qian

Adviser: Dr. Jennifer Mueller

Department Head: Dr. Simon Tavener

ABSTRACT OF DISSERTATION

2-D D-BAR CONDUCTIVITY RECONSTRUCTIONS ON NON-CIRCULAR DOMAINS

We study the 2-D Electrical Impedance Tomography problem, which is the problem of finding the conductivity inside a domain from knowledge of the Dirichlet-to-Neumann map. The focus of this dissertation is to improve the numerical implementation of the D-bar method. The D-bar method is a direct (non-iterative) method that solves the full nonlinear problem with no data fitting. The major contribution of this dissertation is the improvement in the calculation of the scattering transform. The scattering transform is an intermediate function, not directly measurable in experiments, that plays an important role in the conductivity reconstructions. The main focus of this work is to incorporate accurate domain modeling in the algorithm, such as the boundary of a cross-section of a human chest. We show good improvement from previous implementations, and provide a thorough study showing the effects of modeling assumptions and errors in data on conductivity reconstructions.

Ethan Kane Murphy
Department of Mathematics
Colorado State University
Fort Collins, Colorado 80523
Fall 2007

ACKNOWLEDGEMENTS

I'd like to thank my mom for all of her love and support. Also I'd like to thank my advisor, Jennifer Mueller, for providing plenty of help and guidance. I also would like to thank Megan, Jutta, and Chris for listening to my ideas and helping with looking at far too many reconstructions. I'd like to thank my committee, Paul Duchateau, Michael Kirby and Xianghong Qian for good questions and comments. Lastly, I'd like to thank the CSU Mathematics department for all of the financial support that I have accrued over the years here as a teaching assistant and most recently the Yates Fellowship this last semester without which I never would have finished.

TABLE OF CONTENTS

LIST OF FIGURES

Chapter 1

INTRODUCTION

In this dissertation we discuss solutions of the 2-D Electrical Impedance Tomography (EIT) problem using the D-bar method. The general idea of the problem of EIT is to determine the conductivity in the interior of a body given the voltages on the surface arising from a basis of current patterns applied on the boundary.

EIT has many applications in the medical fields such as monitoring ventilation and perfusion, diagnosis of pulmonary edema and pulmonary embolus, and breast cancer detection. The problem also has several industrial applications including subsurface flow monitoring and remediation, underground contaminant detection, and nondestructive evaluation.

The problem is modeled by the conductivity equation

$$\nabla \cdot (\gamma(x,y)\nabla u(x,y)) = 0, \quad (x,y) \in \Omega, \tag{1.1}$$

where Ω denotes a 2-D simply connected domain, γ represents the conductivity of the domain, and u is the electric potential. Applying a known voltage, f, on the boundary of the domain corresponds to a Dirichlet boundary condition

$$u(x,y) = f(x,y), \quad (x,y) \in \partial\Omega, \tag{1.2}$$

where $\partial\Omega$ is the boundary of the domain. Measuring the resulting current density distribution, j, on the boundary corresponds to knowing the Neumann boundary condition

$$\gamma(x,y)\frac{\partial u}{\partial \nu}(x,y) = j(x,y) \quad (x,y) \in \partial\Omega, \tag{1.3}$$

where ν is the outward normal on the boundary. The mapping that takes the given voltage distribution on $\partial\Omega$ to the current density distribution on $\partial\Omega$ is called the Dirichlet-to-Neumann map or the voltage-to-current density map and denoted as Λ_γ. Knowledge of the map Λ_γ enables the problem of EIT to be solved.

The application of the D-bar method to solve the EIT problem is relatively new. The D-bar method is a direct (non-iterative) method that solves the full nonlinear problem with no data fitting, discussed in Chapter 4. The first numerical results were published in 2000 by Siltanen, Mueller, and Isaacson, [71]. Since that time there have been publications of steady improvements in the method.

The focus of this dissertation is to improve the numerical implementation of the D-bar method. The major contribution of this dissertation is the improvement in the calculation of the scattering transform. The scattering transform is an intermediate function, not directly measurable in experiments, that plays an important role in the conductivity reconstructions. It is computed from an integral involving the Dirichlet-to-Neumann map for (1.1) and for a homogeneous conductivity distribution. In previous works the approximations to the scattering transform utilized the analytic solution of the forward problem with a constant conductivity on a circle with the continuous electrode model, trigonometric current patterns, and

assumed a constant conductivity on the boundary. In addition the scattering transform has only been computed on a circular domain. We study the scattering transform and how the forward problem, current patterns, and the conductivity on the boundary are involved in its calculation. These improvements result in more accurate conductivity reconstructions. We discuss below some details of the improvements that are made.

The forward problem is used to construct the Dirichlet-to-Neumann map for the homogeneous conductivity distribution which is used in the calculation of the scattering transform. The statement of the forward problem is to find $u|_{\partial\Omega}$ given (1.1) and (1.3). One straightforward improvement is the calculation of the forward problem on the particular domain in question. We look at both analytic and numerical calculations of this solution. Another improvement is proper electrode modeling. Large errors result if one doesn't model electrodes properly in the experiment of injecting a specified current through an electrode into a body. The amount of such errors and details of several electrode models introduced to overcome this problem are discussed in the next chapter.

Secondly, we look to improve/investigate current patterns. The reconstruction algorithm requires the knowledge of the voltage-to-current density map, Λ_γ. In practice this is calculated by injecting a set of currents on the electrodes, measuring the resulting voltages on the electrodes, and then numerically solving the inverse problem. The set of currents injected are called current patterns (CP). There are several standard CPs that are often used in EIT, discussed in Chapter 2. In addition to the standard types one can consider 'optimal' CPs. The 'optimal' definition is also discussed in Chapter 2. We construct these in a few different ways, described in Chapter 7. Lastly, we modify the calculation of the scattering transform so that

we can apply any set of CPs. Results of these reconstructions are shown in Chapter 7.

Third, we study a method called layer-stripping that enables us to construct γ and $\frac{\partial \gamma}{\partial \nu}$ on the boundary of the domain. The knowledge of these functions should improve the accuracy of the scattering transform if we include the initial step in the algorithm of slightly enlarging the modeled domain to include this information. We discuss some background of the method in the next chapter and show the method of implementation and some results in Chapter 10.

A practical improvement in regularization of the scattering transform is presented in Chapter 9. The calculation of the scattering transform is ill-posed so therefore some regularization is needed. It is shown in [54] that the truncation of the scattering transform serves as a method of regularization. We offer a more general truncation method than has been used in order to improve reconstructions.

The latter half of the dissertation is mainly dedicated to studying the effects of the improvements mentioned above on conductivity reconstructions. Data for the reconstructions is taken from an elliptical tank and from simulated chest data. The tank measurements were performed at Rensselaer Polytechnic Institute (RPI) using their ACT3 system. Details of their experimental system are discussed in Chapter 2. The results from the ACT3 data have been published in the Journal of Physiological Measurement, [62], and are presented in Chapter 6.1. The simulated data is constructed using the forward problem with proper electrode modeling, discussed in Chapter 3. The simulated data consists of a chest shaped domain with at most heart, lungs, ribs, skin, and aorta in the interior. We study various levels

of simulated realistic chests in Chapter 7 and study modeling errors and modeling assumptions from the simulated data in Chapter 8.

Chapter 2

LITERATURE REVIEW

Before we proceed into the details of the D-bar method we will present the following background information of the problem:

- Brief history of the mathematical theory behind EIT;
- Numerical methods involved in solving the problem;
- A review of difficulties that arise when applying the methods to realistic situations.

A detailed review of the history of the EIT problem is given in [11]. One can also find short summaries in, for instance, [4] and [64].

2.1 Brief history of the theory behind EIT

The first mathematical analysis of the EIT problem originated in 1980 by Calderón who considered the linearized problem, [14]. Calderón began the analysis by posing the question of whether γ, the conductivity, could be uniquely determined from the voltage-to-current density map, $\Lambda_\gamma : H^{1/2}(\partial\Omega) \to H^{-1/2}(\partial\Omega)$, defined by the inner product

$$\langle g, \Lambda_\gamma f \rangle = \int_\Omega \gamma \nabla v \cdot \nabla u dx, \tag{2.1}$$

where $f, g \in H^{1/2}(\partial\Omega)$, $u \in H^1(\Omega)$ is the weak solution of the Dirichlet problem, given by

$$\begin{aligned} \nabla \cdot (\gamma \nabla u) &= 0, \quad \text{in } \Omega, \\ u &= f, \quad \text{on } \partial\Omega, \end{aligned} \tag{2.2}$$

and v is any function in $H^1(\Omega)$ with $v|_{\partial\Omega} = g$. Stated explicitly, Calderón studied whether given any two maps such that $\Lambda_{\gamma_1} = \Lambda_{\gamma_2}$ if this implied that $\gamma_1 = \gamma_2$. Calderón proved injectivity (1-1) of the derivative at $\gamma =$ *constant* of the map $\gamma \mapsto \Lambda_\gamma$ and gave an approximate reconstruction of the conductivity.

The first general result on the nonlinear map $\gamma \mapsto \Lambda_\gamma$ was obtained by Kohn and Vogelius [48], who showed that boundary values of a smooth γ could be determined from knowledge of Λ_γ. Then they extended their work [49], to cover piecewise analytic conductivities.

In 1987 Sylvester and Uhlmann proved global uniqueness for the problem in 3D, and higher dimensions, [78]. The bounded domain was assumed to be smooth and the conductivity considered was smooth and isotropic. Then in 1988 Nachman gave a D-bar reconstruction method for isotropic conductivity in $C^{1,1}(\bar{\Omega})$ with $n \geq 3$ and domains with $C^{1,1}$ boundaries [63].

Results of continuous dependence and stability results were shown in [79] and [2] respectively. Sylvester gave results for anisotropic smooth conductivities in 1990 [76]. Instead of uniqueness it was found that if there were two conductivities that produced the same boundary measurements then the conductivities varied by a diffeomorphism. Sylvester's result had large constraints on the conductivity. This same result, but with $\gamma \in \mathbb{C}^3$, was shown in 2003 by Greenleaf, et al, [32].

In 1996 Nachman gave a constructive proof for the 2D problem [64]. The reconstruction method given in Nachman's proof is known as the D-bar

method and is the basis of the work in this dissertation. The conductivity, γ, was assumed to be in $W^{2,p}$ for some $p > 1$ and the bounded domain was assumed to have a Lipschitz boundary. The general $\bar{\partial}$-bar method comes from inverse scattering theory and evolution equations. The method originated in the work of Gardner, Greene, Kruskal, and Miura [26] on the Korteweg-de Vries (KdV) equation. The D-bar approach to inverse scattering seems to have originated from Beals and Coifman in [8]. A short summary, from the same authors, is given in [9] of the idea. They state, "in a broad outline, a nonlinear evolution equation and a linear spectral problem are associated in such a way that the nonlinear evolution corresponds to a trivial linear evolution of the 'scattering data' for the linear spectral problem." It associates the time dependent Schrödinger equation, an evolution equation, to the D-bar problem, a linear spectral problem, where the 'scattering data' is the scattering transform that we have mentioned before. We discuss how the solution of this gives us the conductivity from the generalized Laplace equation in Chapter 4.

In 1997 using the D-bar method Brown and Uhlmann sharpened Nachman's 1996 proof to $\gamma \in W^{1,p}$, $p > 2$ [13]. In 2000 Francini gave a proof for conductivity and permittivity in 2D, [25]. Francini's proof allows γ to be complex valued as long as the complex piece is small enough. In 2006 Astala and Päivärinta gave a proof showing that a nonsmooth, L^∞, anisotropic conductivity in 2D can be found up to a $W^{1,2}$-diffeomorphism, [4]. In addition if we have $\gamma \in L^\infty$ that is isotropic, it is determined uniquely by Λ_γ on a simply connected domain.

We see that the theory has come a long way since Calderón. The last proof by Astala and Päivärinta represents a large and important step

in the pursuit of the realistic situation because in a human chest there are jumps in conductivity values. Although we are using a method that assumes $\gamma \in W^{2,p}(\Omega)$, since $C^0(\Omega)$ is compactly embedded in $W^{2,p}(\Omega)$ we hope that it will work reasonably well with real data.

2.2 Numerical Methods

There is a wide variety of numerical methods used to recover conductivities from the Dirichlet-to-Neumann map. However in all the different schemes there are two basic approaches to EIT reconstructions; static (absolute) and dynamic (difference) images. We define each term below.

Definition 2.2.1. ***Static image***

A static image is produced using one set of 'measured' voltages to reconstruct static (true) conductivity values in the domain.

Definition 2.2.2. ***Difference image***

A difference image uses a set 'measured' voltages and a second set of 'measured' voltages referred to as a reference frame to reconstruct images.

In general, it has been found that static images are more sensitive to measurement error [7]. Difference images are stable, but they can not produce absolute conductivity values.

The numerical schemes can be split into five categories

- non-iterative linearization-based algorithms;
- iterative algorithms solving the full nonlinear problem;
- layer-stripping algorithms;
- statistical inversion;

- D-bar methods.

We will briefly review the literature of methods in each of these general categories.

2.2.1 Non-iterative linearization-based algorithms

The basic premise of the linearized models is that the conductivity varies a small amount from some known distribution. If the conductivity varies a large amount the model is no longer valid. Some lung problems can not be diagnosed using EIT without the actual conductivity values. However, difference images are useful, for example in determining which regions are begin ventilated or perfused. In contrast this method is not useful for scenarios with large variations where conductivity values are important to know, for instance, breast cancer detection. In this case knowing the conductivity values is, basically, the difference between knowing whether a tumor is benign or malignant.

Back-projection methods were introduced in 1983 and 1984 by Kim [44] and Barber and Brown [5], respectively. An implementation of Calderón's approach is shown in [10]. Other numerical schemes based on Calderón's approach [14] were developed in 1990 and 1991 by Cheney [16] and Isaacson [36], respectively. A moment method was used in 1991 by Allers, et al. [3].

A one-step Newton-Raphson algorithm, coined NOSER, was published in 1990 by Cheney, et al. [17]. This work was first done by Simske in a master's thesis [73]. This research group at Rensselaer Polytechnic Institute constructed a system called ACT3 which stands for Adaptive Current Tomograph 3 that measures voltages from applied currents. This is of interest to us because we show results reconstructed from data from this system later in this dissertation.

2.2.2 Iterative algorithms solving the full nonlinear problem

In 1985 Murai and Kagawa, [61], developed an iterative method involving the finite element method (FEM) based on the sensitivity theorem or lead theorem derived by Gesolowitz, [30], and Lehr, [55]. An iterative approach involving sensitivity coefficients was developed by Kotre in 1989 [53].

An iterative Newton's method emerged in 1987 by Yorkey, et al, [87]. This differed from NOSER by the fact that they let the Newton's method converge instead of just taking one step at each iteration. There have been improvements on the Newton's method. For example, in 1991 Hua, et al. presented a method using regularization and optimal current patterns combined with a Newton-Raphson algorithm, [34].

In 1998 Vauhkonen, et al. used Kalman filters to reconstruct conductivities, [82]. The method is based on the formulation of the EIT problem as a state estimation problem and the recursive solution to the problem with the Kalman filters. Kalman filters were also used in Kim et al,[43] and in 2004 by Trigo, Gonzalez-Lima, and Amato [80].

Many of these methods are very promising. Their efficiency is limited by each method's ability to converge and its rate of convergence. This is the main draw-back of these algorithms.

2.2.3 Layer-Stripping

Methods of reconstruction using layer-stripping have been published in [77] by Sylvester and [75] by Somersalo, et al. The method is non-iterative and it uses a discrete number of shells to reconstruct the conductivity on a circular domain working from the outside inward. The steps of the algorithm are clearly described in [75]. Unfortunately, this method has not

been considered recently due to unstable reconstructions with experimental data. However, we have used it to evaluate γ and $\frac{\partial \gamma}{\partial \nu}$ on the boundary of the domain. The details of the method will be described later in this dissertation.

2.2.4 Statistical Inversion

In 2000 a method called statistical inversion was introduced by Kaipio, et al. [42]. The EIT problem is considered in the framework of Bayesian statistics. The method uses, due to the high dimensionality of the problem, Markov chain Monte Carlo integration. Regardless, this relatively new method seems to be a viable strategy in reconstructing conductivities for the EIT problem. Other publications using this method include [33] in 2002 and [84] in 2004.

2.2.5 D-bar method

The D-bar algorithm considered here first appears in the 1996 uniqueness proof by Adrian Nachman, [64]. The first numerical implementation of this algorithm was published in 2000 by Siltanen, Mueller, and Isaacson, [71]. The implementation was performed on a circular domain and tested smooth, radially, symmetric conductivity distributions.

In [72], Siltanen, et al. extended the 2000 implementation to slightly more complicated and higher contrast radially symmetric conductivities. In 2002 Mueller, et al. published results of the D-bar method performed on phantom chests, [60]. The phantoms were simulated inside a unit disc and were given conductivities similar to the conductivities of the lungs and heart. This method assumed knowledge of the conductivity in the domain in order to construct an accurate calculation of the scattering transform.

Therefore this study mainly showed the accuracy of the solution of the D-bar equation. They found relative errors of the conductivity values to be 8.3% and 9.3% in the lungs and heart regions, respectively. In addition the location of the virtual lungs and heart were well approximated in the reconstructions.

Then in 2003 Knudsen, et al. [46], published work on a fast method for solving the D-bar equation. The implementation used a multigrid method developed by Vainikko, [81], adapted to the problem with FFT (fast fourier transform) implementation. Their method resulted in a convergence rate of $\mathcal{O}(h)$. In [59], Mueller, et al. considered several nonsymmetric examples and developed a regularization technique to handle the ill-posedness of the problem.

Reconstructions of chest phantoms were performed with experimental measurements in [37]. The results of the D-bar method were compared with that of the NOSER algorithm. Experimental data was measured on the boundary of a circular saline tank with $15cm$ radius and 32 electrodes. Static reconstructions produced by the D-bar method had a relative error of conductivity values of 12% and 23% in the heart and lung areas, respectively, compared with a 41% and 28% relative errors for the NOSER algorithm. The D-bar method was also able to detect better clarity of the difference objects in the saline tank. That is, the NOSER algorithm connected the two agar lungs in the reconstruction whereas D-bar showed them separated.

In 2006 Isaacson, et al. published conductivity reconstructions from voltage measurements taken on the circumference of a human chest, [38]. The chest was modeled by a circle with radius of $14.3cm$. Only difference

images were included i.e. reconstructions are relative to one particular reference frame chosen from the 100 frames of collected data. These difference images will be discussed in more detail later on. In the reconstructions one can clearly see the changes in one cardiac cycle. That is, one can observe high conductivity of the blood in the heart near the beginning of the cycle followed by a reduction of conductivity in the heart area and an increased conductivity in the lungs corresponding to blood flowing from the heart to the lungs.

There has been other work using the D-bar method. For instance, in 2004 Cornean, et al. published an article exploring EIT in 3D [19]. In addition Knudsen implemented the proof from Brown and Uhlmann for $\gamma \in W^{1,p}$ and produced some reconstructions on simulated data [47, 45].

2.3 Difficulties in applications of EIT

There are several difficulties arising with the applications of these numerical methods to human chest data. For instance, many methods described above, including D-bar, have assumed that the domain is circular. This assumption simplifies much of the mathematics and has produced good reconstructions on circular domains, but artifacts arise when the method is applied to, for instance, elliptic domains or actual experiments with chest data. Other issues include chest expansion and compression, electrode placement, current patterns, contact and skin impedance, etc. We will discuss some studies that directly focus on these issues below.

2.3.1 Non-circular domain

In 1996 Gersing, [28], studied the effects of deforming a circular region into a elliptic region on static reconstructions. They used an elastic material

to build a tank which began as a cylinder of $220mm$ diameter with 16 electrodes equally spaced. The diameter range varied by -10% to 5%. The reconstructions were performed using a back-projection method, [29], and the reference measurements were taken when the tank was cylindrical. In general they found that the more the domain was deformed, the more spatial artifacts appeared. The change in reconstructed conductivity values of objects in the domain are of the order of magnitude of 1% per percentage change in the axis length. Its interesting to note that this dependence was found to be just about linear.

In 1997 Jain, [41], also found large errors in the center of the domain for static images in a similar experiment as Gersing. Jain's study was simulated instead of measured. They experimented with an elliptic domain and a circular mesh. The reconstructed conductivity error in the center of the image was as much as 20% when the axis ratio was 0.73 and the error increased to 37% when the ratio was reduced to 0.64 for a homogeneous domain. Then when they used an elliptic mesh, i.e. matching the experimental setup, the error was reduced to within 0.5% of the actual values, thus showing accurate modeling of the domain is very important. The method used to get reconstructions of the conductivity was an iterative Newton's method.

There have been methods developed to overcome the questions about unknown domain shape. For instance Molebny in 1996, [58], developed a electromechanical method for the determination of the boundary shape. Their apparatus measures the subject's radius as a function of angular displacement by capacitive probes. The boundary is approximated using a Fourier series, in which coefficients are determined by collected data.

There has also been a method suggested by Seydnejad and Fahimi 1992, [69]. However, with the use of MRI or CT images the boundary shape and location of the electrodes can also be relatively easily found.

In 2005 Kolehmainen, et al, [51] a method was introduced that attempts to account for non-circular domains with the theory of Teichmüller spaces. The method was implemented numerically and it removed any large artifacts using simulated data.

2.3.2 Chest expansion

During real-time reconstructions the chest changes during respiratory activity, i.e. the domain changes. The anterior posterior (AP) dimension (or chest thickness) changes by up to 10%. The effect of chest expansion was studied in 1996 by Adler, [1], using simulated data from a FEM code, and reconstructions were produced by a regularized linear algorithm. The FEM implementation was actually modeled to account for chest expansion. It was found that chest expansion accounts for up to 20% of the reconstructed image amplitude. It also introduces an artifact in the center of the image, which moves the reconstructed lungs closer together. This effect was also observed in [38] for the NOSER algorithm.

It was found in [1] that the artifact in the center of the image is broad and accounts for 2% to 20% of the image magnitude. The amplitude changes significantly with changes in the lateral to AP expansion ratio. The percentage contribution to the total image due to conductivity change and chest expansion is relatively constant with increasing rib cage movement, that is up to 3%. This basically implies that difference images are very promising.

2.3.3 Electrode placement

In [7] errors are analyzed for incorrect electrode placement from reconstructions produced by the filtered back-projection method described in [6]. It is shown that with their particlular method the reconstructions are insensitive to electrode placement with difference images. Specific relative errors are not given. In their experiment they placed a circular object with radius 20% of the circular tank radius in the center of the tank and randomly displaced the electrodes around the inside boundary. The average error of the displacement of the electrodes was 1.2°, which represents a positioning error of about $3.3mm$ since the circumference of tank was $100cm$. The static images produced have many artifacts and it is hard to distinguish the circular object in the domain, whereas the difference images, using a reference frame of the randomly placed electrodes, are barely affected. This robustness of difference images and sensitivity of static images is found in a comparable test in [1].

2.3.4 Current patterns

In all the experiments there are current patterns (CP) applied to the boundary of the domain. The choice of the CP is based on ease of implementation, cost, and its effect on the reconstructions. Trigonometric CPs (TCP) are used in [17], [71], [60], [59], and [62]. Alternating CPs (ACP) are used in [23] and [50]. A research group in Brazil uses ACPs and skip 3 CPs [80]. These CPs are defined in this section. Reconstructions using each of these CPs are illustrated later on in this dissertation.

The TCPs are defined as

$$T_l^k = \begin{cases} Mcos(k\theta_l), & k = 1, ..., \frac{L}{2} \\ Msin((k - \frac{L}{2})\theta_l), & k = \frac{L}{2} + 1, ..., L - 1. \end{cases} \quad \text{where } \theta_l = \frac{2\pi l}{L} \quad , \quad (2.3)$$

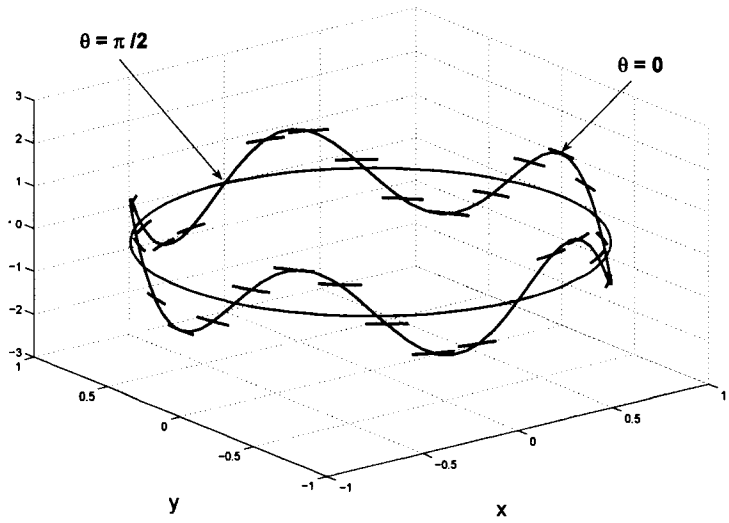

Figure 2.1: An illustration of a TCP, $cos(5\theta)$ around a unit disc on the right with amplitude of 1mA on a 32 electrode setup.

where T_l^k represents the k^{th} CP on the l^{th} electrode. We give an illustration of one TCP in Figure 2.1. It is a 32 electrode setup showing $T^5(\theta) = cos(5\theta)$ with an amplitude of 1mA. The red line represents the domain, the blue line is the continuous function of $cos(5\theta)$, and the black segments represent the currents that are injected on each of the 32 electrodes.

The ACPs inject a positive current on one electrode and a negative current of the same amplitude on an adjacent electrode. The full set is described by the following function

$$T_l^k = \begin{cases} M, & \text{if } l = k \\ -M, & \text{if } (l+1) mod\ L = (k+1) mod\ L, \\ 0, & \text{otherwise.} \end{cases} \tag{2.4}$$

The skip CPs inject a positive current into a specified electrode and injects a negative current s electrodes away. The skip type of CPs can be generalized by the following equation

$$T_l^k = \begin{cases} M, & \text{if } l = k \\ -M, & \text{if } (l+s) mod\ L = (k+s) mod\ L, \\ 0, & \text{otherwise,} \end{cases} \tag{2.5}$$

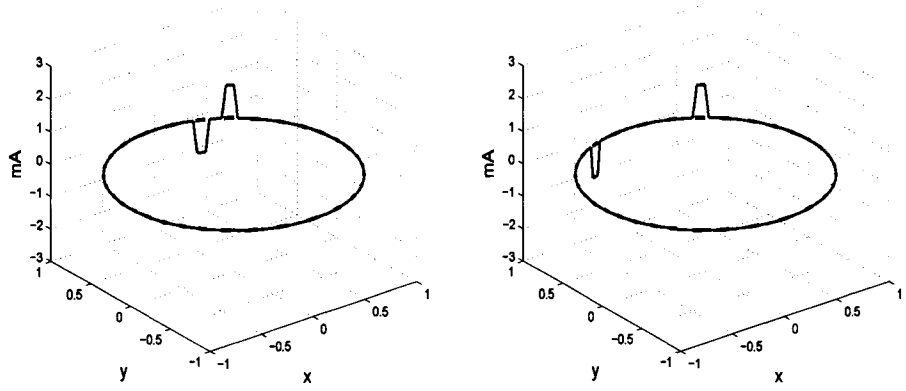

Figure 2.2: Illustrations of one CP of ACP's, on the left, and S3CP's, on the right. The red segments represent electrodes and the blue line represents the injected current. It is a 32 electrode system with a amplitude of 1mA.

where s is the number of electrodes skipped. We will refer to any set of CPs where we skip more than one electrode as SsCP, meaning skip s electrodes. We illustrate one CP from ACP and S3CP in Figure 2.2. The red line segments represent the electrodes and the blue line is the injected current. It is on a 32 electrode system with a current amplitude of 1mA.

A drawback of the skip CPs is that the number of independent electrodes is dependent on the numbers of electrodes skipped. So, there needs to be care taken in which skip CPs to use so that there are enough independent CPs. We will discuss the specifics for a 32 electrode setup later. Although, intuitively the more electrodes we skip the more we penetrate into the domain. Unfortunately, since our method is extremely dependent on our ability to have a good approximation for the Dirichlet-to-Neumann map, any reduction in the rank of this mapping is detrimental to complete knowledge of the map. This relation will be discussed in Section 7.2.

Another set of CPs that have been used is a based on Walsh functions [85]. Walsh functions do not form a large set of independent CPs and are

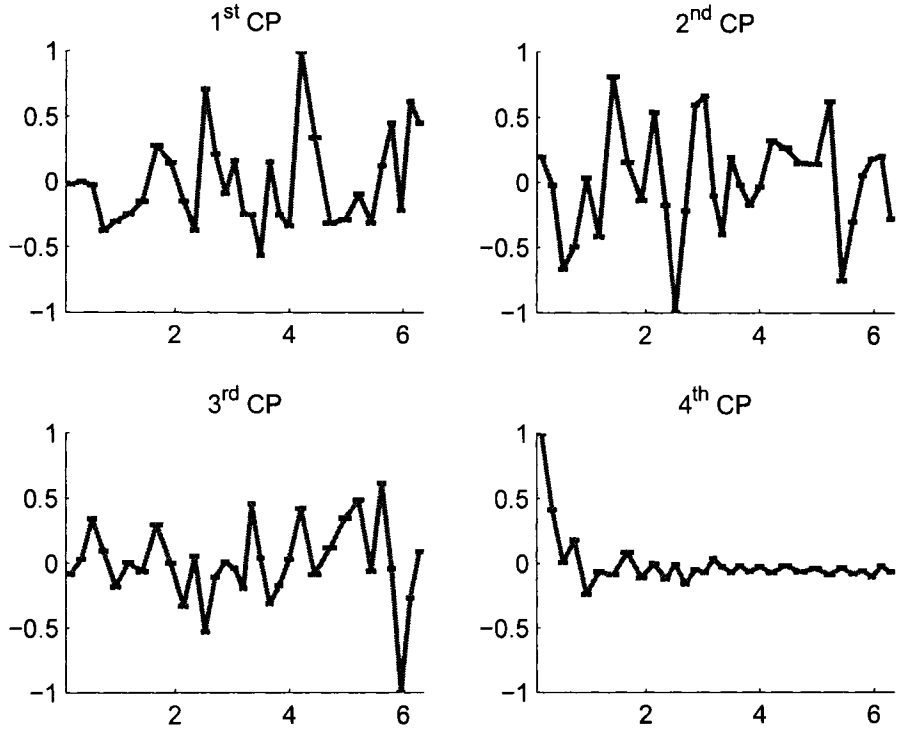

Figure 2.3: An illustration of the first 4 OHCPs on a setup with 32 electrodes and a amplitude of 1mA.

not orthonormal. Thus, as an approximation to Walsh functions, we use a set of CPs defined by a orthonormal Hadamard matrix of size $L \times L$. We specifically use Matlab's hadamard function to generate the matrix. Using the constraint that all the vectors must sum to zero we have L-1 vectors that are non-trivial. We call these OHCPs and several CPs for this set are shown in Figure 2.3.

There have been thorough studies of what CPs are best. It was found in [35] by Isaacson that for unknown radially symmetric conductivities on a circular domain TCPs are optimal. Isaacson's study included a new concept (measure) called distinguishability. It is used to measure how well the CPs

can distinguish an object in the domain; it is defined as

$$\delta \equiv \frac{\left[\sum_{l=1}^{L}\left(V_l^k(\sigma) - V_l^k(\tau)\right)^2\right]^{\frac{1}{2}}}{\left[\sum_{l=1}^{L}(J_l^k)^2\right]^{\frac{1}{2}}} \tag{2.6}$$

where σ and τ are two different conductivities, $V_l^k(\sigma)$ and J_l^k are the voltages and currents, respectively, for the k^{th} current pattern on the l^{th} electrode. In addition in [31] Gisser and Isaacson proposed an iterative scheme to find the best current pattern when the conductivity distribution is unknown. This will be discussed later.

However, ACPs have also been argued to be optimal in the same case in [23] and [50]. Then in 1994 Dobson and Santosa [20] found that TCPs resulted in more accurate and stable reconstructions than ACPs with numerical simulations.

2.3.5 Electrode/Contact Impedance

The electrode-skin interface is an important aspect to understand when simulating the forward problem. Experimentally it has been found that a straightforward implementation of FEM that does not consider electrode effects differs greatly from experimental measurements [18]. For this reason the contact impedance must be considered in order to get more accurate results. The contact impedance can be viewed as two distinct problems. The first is the electrochemical impedance that exists at the interface between electrode and skin, [52]. A simple electrical method for assessment of this has been presented by Newell et al, [66]. The second is the impedance of the skin. This can be modeled rather simply with lumped models, and examples of this are shown in Panescu, [67] and McAdams [57].

In order to overcome this problem electrode models have been developed. The electrode model that has shown the best results is called the complete electrode model (CEM) originally described in 1989 by Cheng et al [18]. Existence and uniqueness of the results of the model are discussed in [74]. An implementation of the FEM code for the CEM was described in [83]. The details of several electrode models including CEM are discussed below.

Continuous Model

The continuous model assumes that the current density on the boundary of the tank is described by

$$J^n = \frac{T^n(\theta)}{A},$$

where A is the area of an electrode and $T^n(\theta)$ is defined as a current pattern. In [18], it was shown that this model overestimates the 'characteristic resistivity' on electrodes of experimental data by as much as 25%. This is because no electrode effect is taken into account. The 'characteristic resistivity' is defined as the voltage divided by the current on the electrodes.

Gap Model

The first logical correction for the electrode effect is to input a current density only on the electrodes. This is done in the gap model with the current densities described as follows:

$$J^n = \begin{cases} \frac{T^n(\theta_l)}{A}, & \theta \in e_l,\ l = 1, 2, ..., L \\ 0, & \theta \notin e_l,\ \forall l. \end{cases} \tag{2.7}$$

where $e_l \equiv [\theta_l - \frac{\delta\theta}{2}, \theta_l + \frac{\delta\theta}{2}]$ represents the angular values for the l^{th} electrode. This model assumes that the current density is uniform across the whole electrode. Experiments have shown that this model also overestimates the characteristic resistivities, [18].

Shunt Model

The shunt model takes into account the shunting effect of the electrode. This is done by eliminating the assumption that the current density is a constant on the electrode and then assuming that the potential on the electrode is constant. Thus, we replace the boundary conditions with more reliable ones,

$$\int_{e_l} \gamma \frac{\partial u}{\partial \nu} dS = T_l^n, \ l = 1, 2, ..., L, \tag{2.8}$$

i.e. the overall current across the electrode. The following boundary condition is really where we take into account the shunting effect,

$$u = U_l, \ x \in e_l, \ l = 1, 2, ..., L, \tag{2.9}$$

where U_l is the measured voltage on the l^{th} electrode. This model underestimates the characteristic resistivity of the electrodes since the contact impedances are ignored, [74].

Complete Model

The complete electrode model, CEM, takes into account both the shunting effect of the electrodes and the contact impedances between the electrodes and tissue. The complete electrode model consists of the conductivity equation and the following boundary conditions:

$$u + z_l \gamma \frac{\partial u}{\partial \nu} = U_l^n, \quad x \in e_l, \ l = 1, 2, ..., L \tag{2.10}$$

$$\int_{e_l} \gamma \frac{\partial u}{\partial \nu} dS = T_l^n, \quad x \in e_l, \ l = 1, 2, ..., L \tag{2.11}$$

$$\gamma \frac{\partial u}{\partial \nu} = 0, \quad x \in \partial\Omega \backslash \cup_{l=1}^{L} e_l, \tag{2.12}$$

where z_l is effective contact impedance between the l^{th} electrode and tissue. In addition, the following two conditions for the injected current and

measured voltages are needed to ensure existence and uniqueness of the result:

$$\sum_{l=1}^{L} T_l^n = 0, \tag{2.13}$$

$$\sum_{l=1}^{L} U_l^n = 0. \tag{2.14}$$

This model has been shown to predict the measured voltages at the precision of the measurement system, [74].

2.3.6 Concluding remarks of application problems

After reviewing the difficulties in the EIT problem we have several concerns: accurate modeling of the domain, the effect CPs have on the reconstructions, electrode modeling, and effects of experimental errors. The first conclusion is to model the domain as accurately as possible. Our overall goal is to construct good static images that reproduce accurate conductivity values in the domain. Thus, we will spend a good deal of this dissertation modifying different aspects of the method to the specific domain we are interested in. The second point is that the D-bar method has not been tested with CPs other than the TCPs. The review of literature on CPs left us with ambiguous answers to which CPs are the best. Therefore, we determine empirically the best CPs for the D-bar method. This includes testing against optimal CPs defined in [35]. The construction of optimal CPs is discussed in Chapter 7. We found the that the problem of correctly modeling the electrodes has been practically overcome by the CEM. Thus we implement FEM combined with the CEM. The details of this are described in Chapter 3. Illustrations showing the usefulness of CEM are in Chapter 8. The final point, measurement error will be discussed in Chapter 8.

Chapter 3

FORWARD PROBLEM

In this chapter we present solutions of the forward problem for a general domain using analytic and numerical methods. We need to solve the forward problem to simulate voltage data. This data is used for testing purposes and in the reconstructions of conductivities using the D-bar method.

In the forward problem, we assume that the conductivity, γ, is known throughout the domain, we inject certain currents along the boundary, and our goal is to find the voltages, u, throughout the domain and on the boundary. In mathematical terms, we want to solve the conductivity equation,

$$\nabla \cdot \gamma \nabla u = 0, \text{ on } \Omega, \tag{3.1}$$

$$\gamma \left. \frac{\partial u}{\partial \nu} \right|_{\partial\Omega} = \frac{1}{A} T(\theta), \tag{3.2}$$

with a goal of finding $u|_{\partial\Omega}$, where T is the current and A is the area of an electrode. The way the boundary condition is written, (3.2), represents the continuous model.

3.1 Analytic solution on a general domain

In this section we demonstrate the analytic solution to (3.1)-(3.2) on a general domain with a smooth boundary for a homogeneous conductivity and for a domain shaped inclusion. We begin the derivation by switching to

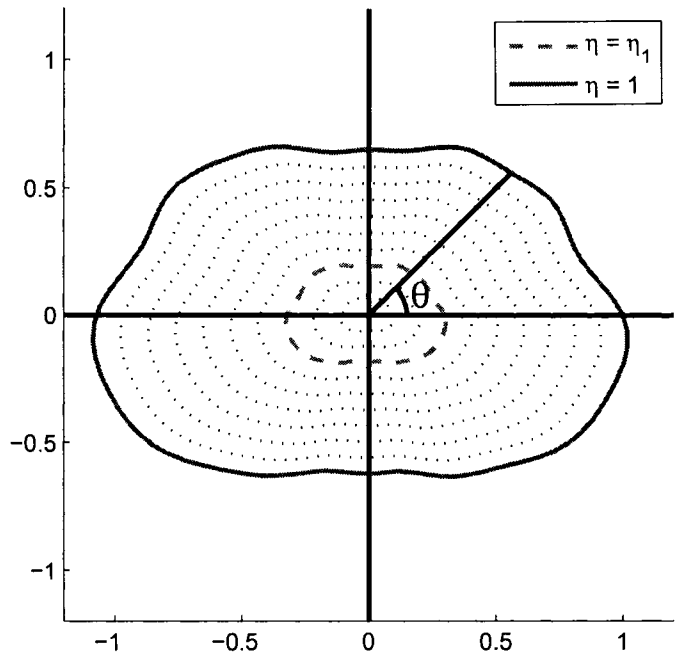

Figure 3.1: Illustration of chest-coordinates.

general domain-shape coordinates (GDSC) defined by the coordinate pair (η, θ). The θ is the standard angle from 0 to 2π from the x-axis, and η is described by (3.3) and illustrated in Figure 3.1. The relation between cartesian and the general domain-shape coordinates is

$$\begin{aligned} x &= \eta r(\theta) cos(\theta), \\ y &= \eta r(\theta) sin(\theta), \end{aligned} \tag{3.3}$$

where $r(\theta)$ describes the boundary of the domain. We only require in our derivation that r is a single-valued $C^1(\partial\Omega)$ function. As a practical illustration we see in Figure 3.1 the GDSCs for a chest-shaped domain. The first step is to transform our problem into this new coordinate system. We find the Laplacian in GDSCs defined from (3.3) using a standard approach

[56]. We get

$$\nabla \cdot \nabla u = p\frac{\partial}{\partial \eta}\left(\eta u_\eta\right) + \frac{1}{\eta}\frac{\partial}{\partial \theta}\left(\frac{1}{p}u_\theta\right) = 0, \tag{3.4}$$

where we define

$$p(\theta) = \frac{\sqrt{(r')^2 + r^2}}{r}. \tag{3.5}$$

The details of the computation are shown in Appendix B.1. The boundary condition becomes

$$\gamma \left.\frac{\partial u}{\partial \eta}\right|_{\partial\Omega} = \frac{1}{A}T(\theta). \tag{3.6}$$

3.1.1 Homogeneous solution

In this section we use separation of variables to solve the Laplacian equation expressed in the new variables assuming a homogeneous conductivity throughout the domain. That is, we assume the form of our solution to be $u = f(\eta)g(\theta)$. We have

$$\frac{\eta\left(f' + \eta f''\right)}{f} = -\frac{\frac{d}{d\theta}\left(\frac{1}{p}g'\right)}{pg} = \mu^2.$$

This gives us two ordinary differential equations (ODE)

$$\eta^2 f'' + \eta f' - \mu^2 f = 0, \tag{3.7}$$

$$-\frac{d}{d\theta}\left(\frac{1}{p}g'\right) = \mu^2 p g. \tag{3.8}$$

The first one, (3.7), is a Euler-Cauchy type ODE and the second equation, (3.8), is a Sturm-Liouville equation.

Let's begin with the Sturm-Liouville type equation (3.8). If we rewrite (3.8) in the form

$$-\left[\frac{1}{p}\frac{d}{d\theta}\left(\frac{1}{p}\frac{d}{d\theta}\cdot\right)\right] g = \mu^2 g,$$

it is apparent that if g has the property that $\frac{d}{d\theta}g(\theta) = \mu ip(\theta)g(\theta)$ then the equation is satisfied. Thus our solution is

$$g(\theta) = e^{inv(\theta)}, \tag{3.9}$$

where

$$v(\theta) = \alpha \int_{\theta_0}^{\theta} p(\theta)d\theta. \tag{3.10}$$

Plugging (3.9) into (3.8) gives us the requirement that $\mu \equiv \pm\alpha n$. Furthermore, we would like to show that this solution (3.9) is an orthogonal set of functions according to the weighted inner product and weighted norm,

$$(h_1, h_2)_p \equiv \int_{-\pi}^{\pi} p(\theta)h_1 h_2 d\theta \quad \text{and} \quad \|g(\theta)\|_p \equiv \sqrt{(g,g)_p}. \tag{3.11}$$

That is, we want the following

$$(g(\theta;n), g(\theta;m)) = \int_{-\pi}^{\pi} e^{inv(\theta)}e^{imv(\theta)}p(\theta)d\theta = \begin{cases} 0, & \text{if } m \neq n \\ \|g(\theta;n)\|_p, & \text{if } n = m \end{cases}.$$

If we require $v(\pi) - v(-\pi) = 2\pi$ then α needs to be defined as

$$\alpha \equiv 2\pi \left(\int_{-\pi}^{\pi} p(s)ds \right)^{-1} \tag{3.12}$$

and the orthogonality argument follows easily.

Next, in order to solve (3.7) we assume $f = \eta^m$. If we consider the case of $\eta^m = 0$ to be degenerate then our solution is when $m = \pm\mu = \pm\alpha n$. We discount the solution when μ is negative to eliminate singularities at the origin. Therefore the solution of (3.7) is

$$f(\eta) = C_n \eta^{\alpha n}. \tag{3.13}$$

Putting (3.13), (3.9), and (3.10) together gives us our overall solution to the problem,

$$u(\eta, \theta) = \sum_{n=1}^{\infty} C_n \eta^{\alpha n} e^{inv(\theta)}. \tag{3.14}$$

The particular solution we are interested in needs to incorporate the boundary condition (3.6). We can express (3.6) as

$$T(\theta) = \sum_{n=1}^{\infty} T_n g_n(\theta), \quad \text{where,} \quad T_n = \frac{1}{\|g_n(\theta)\|_p} \int_{-\pi}^{\pi} T(\theta) g_n(\theta) p(\theta) d\theta.$$

Thus when we use (3.14) to obtain C_n, we get

$$u(\eta, \theta) = \frac{1}{\alpha A} \sum_{n=1}^{\infty} \frac{T_n}{n} \eta^{\alpha n} e^{inv(\theta)}. \tag{3.15}$$

3.1.2 Inhomogeneous solution

Now let us assume we have a domain with a chest-shaped inclusion in the center of the domain, $\eta < \eta_1$, with γ_1 and $\gamma_0 = 1$ outside the inclusion, illustrated in Figure 3.1. We will denote the solution outside the inclusion as w_2 and inside the inclusion as w_1. This problem imposes the conditions

$$w_1(\eta_1, \theta) = w_2(\eta_1, \theta) \tag{3.16}$$

and

$$-\gamma_1 \frac{\partial w_1}{\partial \eta}(\eta_1, \theta) = -1 \frac{\partial w_2}{\partial \eta}(\eta_1, \theta), \tag{3.17}$$

in addition to our previous boundary condition (3.6). We have solutions

$$w_1(\eta, \theta) = \sum_{n=1}^{\infty} D_n \eta^{\alpha n} e^{inv(\theta)} \tag{3.18}$$

and

$$w_2(\eta, \theta) = \sum_{n=1}^{\infty} \left(E_n \eta^{\alpha n} + H_n \eta^{-\alpha n} \right) e^{inv(\theta)}. \tag{3.19}$$

The second solution includes $\eta^{-\alpha n}$ since there are no singularities. The values and method of finding the constants are discussed in Appendix B.2. An interesting note is that if the domain is a circle then $\eta = r$, $v(\theta) = \theta$, and $\alpha = 1$. Hence, one could easily check that the analytic solution on a circle matches the one found here.

3.2 Finite element method

This section describes the FEM implementation used in our research. The FEM approach has advantages over the analytic solution because of the well studied electrode models. A proper implementation of the complete electrode model (CEM) can greatly increase the accuracy of the simulated voltages. This was discussed earlier in Section 2.3.5.

Contents of this section

- Short summary of some theory behind FEM,
- Discussion on implementation of the CEM,
- Investigation into parameter values.

3.2.1 Some FEM details

The FEM method begins with the variational (weak) formulation of the problem. For instance, given our problem described by (3.1,3.2) we would have the following weak form:

$$-\int_{\Omega} \gamma \nabla u \cdot \nabla v dx + \int_{\partial\Omega} T v ds = 0. \tag{3.20}$$

The next step is to discretize the domain into triangles, which can be viewed in Figure 3.2. At each node, N_i, of this triangulation, we assign a linear basis element, φ_j, such that

$$\varphi_j(N_i) = \begin{cases} 1 & \text{if } i = j \\ 0 & \text{if } i \neq j \end{cases}. \tag{3.21}$$

An illustration of a linear basis element is presented in Figure 3.3. The

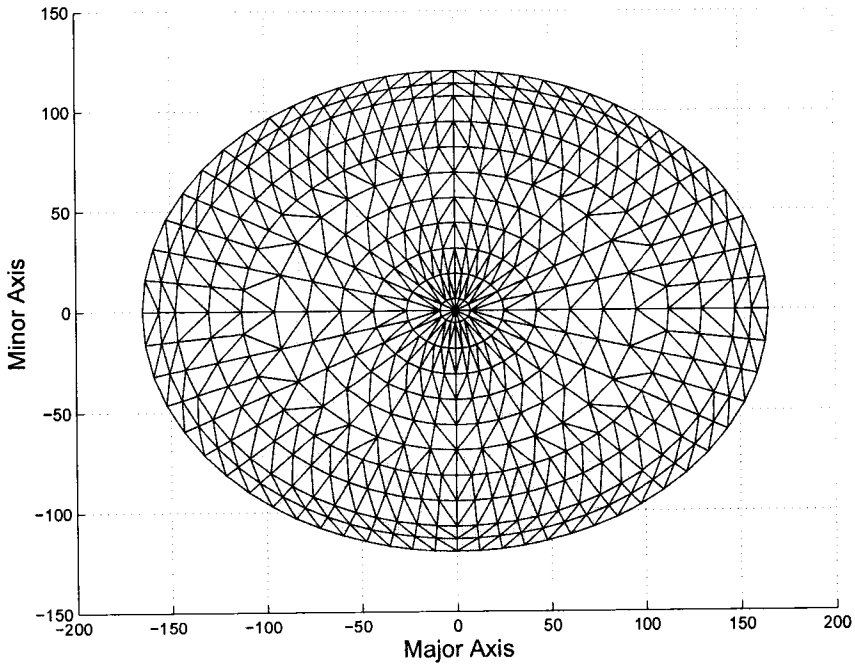

Figure 3.2: A triangulation of an elliptic domain.

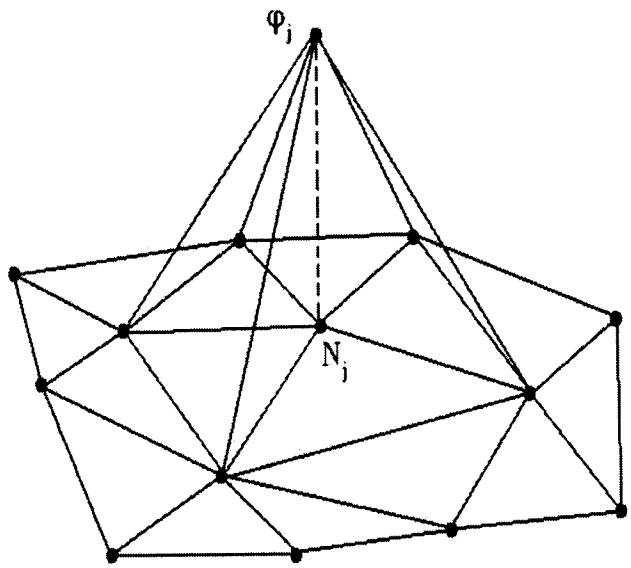

Figure 3.3: Linear basis element φ_j depicted on the FEM mesh.

discretized solution can be written as

$$u^h = \sum_{i=1}^{N_n} \alpha_i \varphi_i, \tag{3.22}$$

where we assume the number of nodes is N_n. Looking back to the weak formulation (3.20), we now want to solve the problem

$$\int_\Omega \gamma \nabla \left(\sum_{i=1}^{N_n} \alpha_i \varphi_i \right) \cdot \nabla \varphi_j dx = \int_{\partial\Omega} T \varphi_j ds, \quad \text{for } j = 1...N_n. \tag{3.23}$$

This is commonly written in the more concise form,

$$A\alpha = f, \tag{3.24}$$

where A is called the stiffness matrix and defined by

$$A_{ij} = \int_\Omega \gamma \nabla \varphi_i \cdot \nabla \varphi_j dx$$

and

$$f_j = \int_{\partial\Omega} T \varphi_j ds.$$

The elegance of FEM is that it reduces the problem of finding the solution of a PDE to that of solving a linear algebra problem, (3.24). The solution, α, will be the voltage value at each node of the mesh.

3.2.2 Implementation of the CEM

An implementation of the FEM for the conductivity equation with the CEM is given in [83]. It states that for any (v, V), $v \in H^1(\Omega)$, $V \in \mathbb{R}^L$,

$$B_s((u, U), (v, V)) = \sum_{l=1}^{L} T_l V_l, \tag{3.25}$$

where B_s is the bilinear form associated with the complete model, given by

$$B_s((u, U), (v, V)) = \int_\Omega \gamma \nabla u \cdot \nabla v dx + \sum_{l=1}^{L} \frac{1}{z_l} \int_{e_l} (u - U_l)(v - V_l) dS. \tag{3.26}$$

Next, we define the solution to our FEM problem as (u^h, U^h), which approximates the solution, (u, U), and are defined as

$$u^h = \sum_{i=1}^{N_n} \alpha_i \varphi \tag{3.27}$$

and

$$U^h = \sum_{j=1}^{L-1} \beta_j n_j, \tag{3.28}$$

where $n_1 = [1, -1, 0, ..., 0]^T$, $n_2 = [1, 0, -1, 0, ..., 0]^T \in \mathbb{R}^L$, etc. This guarantees that (2.14) is not violated.

Thus, in order to implement the FEM code we need to expand (3.25) with respect to our approximation functions, (3.27) and (3.28). We can do this in several steps. First, let us notice that if $1 \leq i \leq N_n$, then U^h is defined to be zero and if $N_n < i \leq N_n + L - 1$, then u^h is zero. Let us first look at the region with $1 \leq i, j \leq N_n$, which, from (3.25), gives us

$$\int_\Omega \gamma \nabla \varphi_i \cdot \nabla \varphi_j dx + \sum_{l=1}^{L} \frac{1}{z_l} \int_{e_l} \varphi_i \varphi_j dS = 0. \tag{3.29}$$

Next, if $1 \leq i \leq N_n$ and $j > N_n$, then (3.25) gives us

$$\begin{aligned} -\textstyle\sum_{l=1}^{L} \frac{1}{z_l} \int_{e_l} \varphi_i (n_j)_l dS &= \textstyle\sum_{l=1}^{L} T_l (n_j)_l \\ -\left(\frac{1}{z_1} \int_{e_1} \varphi_i dS - \frac{1}{z_{j+1}} \int_{e_{j+1}} \varphi_i dS \right) &= \textstyle\sum_{l=1}^{L} T_l (n_j)_l. \end{aligned} \tag{3.30}$$

We have a similar case if $i > N_n$ and $1 \leq j \leq N_n$ in which we get

$$-\left(\frac{1}{z_1} \int_{e_1} \varphi_j dS - \frac{1}{z_{i+1}} \int_{e_{i+1}} \varphi_j dS \right) = 0. \tag{3.31}$$

Lastly, we have the case when $i, j > N_n$, which gives

$$\sum_{l=1}^{L} \frac{1}{z_l} \int_{e_1} (n_i)_l (n_j)_l dS = \sum_{l=1}^{L} T_l (n_j)_l. \tag{3.32}$$

We can combine the equations (3.29), (3.30), (3.31), and (3.32) into a system linear equations written as

$$Ab = f, \tag{3.33}$$

where $b = (\alpha,\ \beta)^T \in \mathbb{R}^{N_n+L-1}$ and $A \in \mathbb{R}^{(N_n+L-1)\times(N_n+L-1)}$ is the sparse matrix of the form

$$A = \begin{pmatrix} B & C \\ C^T & D \end{pmatrix} \tag{3.34}$$

and the data vector is defined by

$$f = \begin{pmatrix} \mathbf{0} \\ \sum_{l=1}^{L} T_l (n_j)_l \end{pmatrix}, \tag{3.35}$$

where $\mathbf{0} = (0, 0, ..., 0)^T \in \mathbb{R}^{N_n}$. The matrices from (3.34) are found from (3.29), (3.30), (3.31), and (3.32) and are presented below:

$$\begin{aligned} B_{ij} = &\ \int_\Omega \gamma \nabla\varphi_i \cdot \nabla\varphi_j dx + \sum_{l=1}^{L} \tfrac{1}{z_l} \int_{e_l} \varphi_i \varphi_j dS, \\ &\text{for } i, j = 1, 2, ..., N_n, \\ C_{ij} = &\ -\left(\tfrac{1}{z_1} \int_{e_1} \varphi_i dS - \tfrac{1}{z_{j+1}} \int_{e_{j+1}} \varphi_i dS \right), \\ &\text{for } i = 1, 2, ..., N_n \text{ and } j = 1, 2, ..., L-1, \\ D_{ij} = &\ \sum_{l=1}^{L} \tfrac{1}{z_l} \int_{e_l} (n_i)_l (n_j)_l dS, \\ = &\ \begin{cases} \frac{|e_1|}{z_1}, & i \neq j, \\ \frac{|e_1|}{z_1} + \frac{|e_{j+1}|}{z_{j+1}}, & i = j, \end{cases} , i, j - 1, 2, ..., L-1. \end{aligned} \tag{3.36}$$

Solving (3.33) gives us the solution of the forward problem. The first N_n values from b, i.e. α, give the voltages throughout the domain and the last $L-1$ values, i.e. β, give the voltages on the electrodes after the following operation,

$$U^h(\gamma, z) = \mathcal{C}\beta,$$

where

$$\mathcal{C} = \begin{pmatrix} 1 & 1 & \cdots & 1 \\ -1 & 0 & \cdots & 0 \\ 0 & -1 & \cdots & 0 \\ & & \ddots & \\ 0 & 0 & \cdots & -1 \end{pmatrix}, \tag{3.37}$$

where $\mathcal{C}$ is size $L \times (L-1)$. Throughout the rest of the paper, we use the abbreviation FEMCEM for the finite element method using the complete electrode model.

3.2.3 Finding Parameter Values

The parameters values that need to be discussed further are γ and $\mathbf{z}$. In our reconstruction method it is an important step to match homogeneous simulated voltages with a set of measured voltages. We do this by finding a best constant conductivity approximation, γ_{best}, to the measured data. The reasoning for this is discussed further in the next chapter. The problem of fitting is made easier by the observation that

$$U(\gamma_0, \mathbf{z}) = \frac{1}{\gamma_{best}} V(1, \tau), \tag{3.38}$$

where $\tau = \gamma_{best}\mathbf{z}$ and $U(\gamma_0, \mathbf{z})$ is an assumed simulated vector of voltage of size $L \times 1$. We present here a straightforward least squares method shown in [37] to find γ_{best}. The problem is to minimize

$$\frac{1}{2}\|U_{meas} - U(\rho_{best}, \mathbf{z})\|^2 = \frac{1}{2}(U_{meas} - \rho_{best}V(1,\tau))^T(U_{meas} - \rho V(1,\tau)), \tag{3.39}$$

with respect to $\rho_{best} \equiv 1/\gamma_{best}$, where U_{meas} are measured voltages with size $L \times 1$. Note that τ is assumed a constant in this equation. If we differentiate (3.39) with respect to ρ_{best} and set it to zero, we get

$$\begin{aligned} (U_{meas} - \rho_{best}V(1,\tau))^T V(1,\tau) &= 0, \\ \frac{U_{meas}^T V(1,\tau)}{V(1,\tau))^T V(1,\tau)} &= \rho_{best}. \end{aligned}$$

Since we want to solve for γ_{best} and we have $L-1$ CPs, we calculate the following

$$\gamma_{best} = \frac{\sum_{i=1}^{L-1} \left(V^{(i)}(1,\tau)\right)^T V^{(i)}(1,\tau)}{\sum_{i=1}^{L-1} \left(U_{meas}^{(i)}\right)^T V^{(i)}(1,\tau)},$$

Table 3.2.3: Conductivity and contact impedance values from [18].

γ_{best} in mS/m	z in m^2/mS	τ in mm
352.1	$5.8 \cdot 10^{-6}$	2.0422
715.8	$3.5 \cdot 10^{-6}$	2.5053
1605.1	$1.5 \cdot 10^{-6}$	2.4076
3389.8	$7.5 \cdot 10^{-7}$	2.5424
	Average:	2.374

where $V^{(i)}(1,\tau)$ and $U^{(i)}_{meas}$ are the voltages, vectors, corresponding to the i^{th} current pattern.

The parameter τ has been studied in [18] for different tank salinities which are illustrated in Table 3.2.3. It was found to be approximately $2.4mm$. There currently are no real guidelines on what τ values to use for the skin-electrode interface. It should be noted that in reality the z or τ parameter is different on each electrode. Unless otherwise stated in the remainder of this dissertation the τ is assumed to be $2.4mm$. Now that the forward problem is well understood we proceed to the inverse problem.

Chapter 4

INVERSE PROBLEM: THE D-BAR METHOD

We present here a general introduction and a detailed outline of Adrian Nachman's conductivity reconstruction method [64]. After presenting the method we will discuss what has been implemented numerically with this method, and the steps we will take to account for the shape of the domain.

It is an important feature of Nachman's proof that it gives a constructive procedure for recovering γ from knowledge of Λ_γ. The idea behind the algorithm is to transform the conductivity equation to the Schrödinger equation and use the D-bar method of inverse scattering to solve the resulting inverse problem.

4.1 Details of the D-bar method

We transform the conductivity equation (1.1) to the Schrödinger equation by letting q be a bounded potential, $q \in L^p(\mathbb{R}^2)$, $1 < p < 2$, and assuming $q = \gamma^{-\frac{1}{2}}\Delta\gamma^{\frac{1}{2}}$ and $\tilde{u} = \gamma^{\frac{1}{2}}u$, to get

$$(-\Delta + q)\tilde{u} = 0 \quad \text{in } \Omega. \tag{4.1}$$

The details of this calculation are shown in Appendix B.3.

The exponentially behaving solutions of (4.1) introduced by Faddeev [24] are the key to the reconstruction, [71]. This is illustrated in *Theorem 1.1* of [64] which states that for any $k \in \mathbb{C}\backslash 0$ there is a unique solution $\psi(x,k)$ of

$$(-\Delta + q)\psi(x,k) = 0 \quad \text{in } \mathbb{R}^2 \tag{4.2}$$

satisfying $e^{-ikx}\psi(\cdot,k) - 1 \in W^{1,\tilde{p}}$ for any $2 < \tilde{p} < \infty$. Note we identify x with $x_1 + ix_2 \in \mathbb{C}$ so this is complex multiplication in the exponent. Details of this function space, $W^{1,\tilde{p}}$, and several others are discussed in Appendix A.

Notice (4.2) is defined on $\mathbb{R}^2$ and (4.1) is defined only in Ω. The solution, $\tilde{u}$, is extended by extending γ to all of $\mathbb{R}^2$. The conductivity, γ, is first extended by analytic continuation to be a constant in a neighborhood $\Omega_2 \supseteq \Omega$. Then γ is extended as a constant outside of Ω_2. This results in $q \equiv 0$ outside of Ω_2 and (4.1) to be defined on the whole plane. Finally, since k has been introduced in (4.2) to get back to (4.1) we just let $k = 0$, i.e. $\tilde{u}(x,0) = \psi(x,0)$.

Next, we denote

$$\mu(x,k) \equiv e^{-ikx}\psi(x,k), \quad x \in \mathbb{R}^2 \quad k \in \mathbb{C}\backslash 0, \tag{4.3}$$

and note that the condition $\mu - 1 \in W^{1,\tilde{p}}$ and the Sobolev imbedding theorem yield that μ is continuous and tends to one asymptotically when $|x| \to \infty$.

With these assumptions in place, let us begin with the steps of the D-bar method [64]. The first step is to determine $\gamma|_{\partial\Omega}$ and $\frac{\partial\gamma}{\partial\nu}|_{\partial\Omega}$ from the following formulas:

$$\langle h, \gamma f\rangle = \lim_{\substack{|\eta| \to \infty, \\ \eta \in \mathbb{R}^{n-1} \times \{0\}}} \langle h_\eta, R\Lambda_\gamma e^{-i\langle\cdot,\eta\rangle} f\rangle, \tag{4.4}$$

and

$$\left\langle g, \frac{\partial \gamma}{\partial \nu} f \right\rangle = \lim_{\substack{|\eta| \to \infty, \\ \eta \in \mathbb{R}^{n-1} \times \{0\}}} \langle g, e^{-i\langle \cdot, \eta \rangle}(2\Lambda_\gamma - \gamma\Lambda_1 - \Lambda_1\gamma)e^{\langle \cdot, \eta \rangle} f \rangle. \quad (4.5)$$

In (4.4) R is the current-to-voltage map of the Laplacian, $f \in H^{\frac{1}{2}}(\partial\Omega) \cap C(\partial\Omega)$, and $h \in L^2(\partial\Omega)$ are assumed to be supported in $U \cap \partial\Omega$ and h_η is defined by

$$h_\eta(x) = h(x)e^{-ix\cdot\eta} - \frac{1}{|\partial\Omega|}\int_{\partial\Omega \cap U} h(y)e^{-iy\cdot\eta} d\sigma(y). \quad (4.6)$$

Furthermore, in (4.5) we assume $\gamma \in W^{2,p}(\Omega)$ for some $p > \frac{n}{2}$; then for any continuous functions f, g in $H^{\frac{1}{2}}(\partial\Omega)$ with support in $U \cap \partial\Omega$ (4.5) is valid. We also introduced Λ_1 in (4.5), which denotes the Dirichlet-to-Neumann map corresponding to a homogeneous conductivity, $\gamma \equiv 1$.

The second step is to constructively reduce the problem to $\gamma \equiv 1$ near the boundary, as mentioned above. Nachman describes this process in section 6 of [64]. The importance of this step is that it results in making (4.1) and (4.2) equivalent. Hence the conductivity equation is equivalent to (4.2) for the class of functions mentioned above.

The next step in the reconstruction of γ is to determine the scattering transform, $t(k)$. The scattering transform is a non-physical object, which cannot directly be measured in experiments:

$$t(k) \equiv \int_{\mathbb{R}^2} e_k(x)\mu(x,k)q(x)dx, \quad k \in \mathbb{C}\backslash 0, \quad (4.7)$$

where

$$e_k(x) \equiv exp(i(kx + \bar{k}\bar{x})).$$

Note that since μ is asymptotically close to one and $kx + \bar{k}\bar{x} = 2k_1x_1 - 2k_2x_2$, $t(k)$ is approximately the Fourier transform of $q(x)$ evaluated at the point

$(-2k_1, 2k_2) \in \mathbb{R}^2$. The scattering transform in (4.7) cannot be computed as it's stated because q is unknown.

We define a single-layer operator S_k for $k \in \mathbb{C}\backslash 0$ by

$$(S_k\phi)(x) \equiv \int_{\partial\Omega} G_k(x-y)\phi(y)d\sigma(y), \tag{4.8}$$

where $G_k(x)$ is the Faddeev Green's function [24].

$$G_k(x) \equiv e^{ikx}g_k(x), \tag{4.9}$$

$$-\Delta G_k = \delta, \tag{4.10}$$

$$g_k(x) \equiv \frac{1}{(2\pi)^2}\int_{\mathbb{R}^2} \frac{e^{ix\cdot\xi}}{\xi(\bar{\xi}+2k)}d\xi, \tag{4.11}$$

$$(-\Delta - 4ik\bar{\partial})g_k = \delta, \tag{4.12}$$

where $\bar{\partial} = (\frac{\partial}{\partial x_1} + i\frac{\partial}{\partial x_2})/2$ and $x\cdot\xi = x_1\xi_1 + x_2\xi_2$. More information and properties of the functions listed above can be found in [71] and Siltanen's PhD thesis, [70]. We can connect some ideas here by noting that [64] shows us that μ satisifies the D-bar equation

$$(-\Delta - 4ik\bar{\partial})\mu = -q\mu. \tag{4.13}$$

Then if we substitute μ from (4.3) into (4.13) we get the Schrödinger equation (4.1).

Nachman gives a relation between the maps Λ_q and Λ_γ defined as

$$\Lambda_q = \gamma^{-\frac{1}{2}}\left(\Lambda_\gamma + \frac{1}{2}\frac{\partial\gamma}{\partial\nu}\right)\gamma^{-\frac{1}{2}}. \tag{4.14}$$

An explanation of this equation is shown in Appendix B.4. Since $\gamma \equiv 1$ in a neighborhood of $\partial\Omega$, the maps Λ_γ and the Dirichlet-to-Neumann map Λ_q of the Schrödinger problem are the same.

By *Theorem 5* of [64] the trace on $\partial\Omega$ of the function $\psi(\cdot, k)$ satisfies the integral equation

$$\psi(\cdot, k)|_{\partial\Omega} = e^{ikx} - S_k(\Lambda_q - \Lambda_0)\psi(\cdot, k) \tag{4.15}$$

for any $k \in \mathbb{C}\backslash 0$. One way of understanding (4.15) is from Alessandrini's identity. A discussion on this and Alessandrini's identity can be found in Appendix B.5. The operator $I + S_k(\Lambda_\gamma - \Lambda_1)$ is invertible on $H^{\frac{1}{2}}(\partial\Omega)$, so we can solve (4.15). Furthermore, if $\psi(\cdot, k)|_{\partial\Omega}$ has been determined, then $t(k)$ can be recovered from the formula

$$t(k) = \int_{\partial\Omega} e^{i\bar{k}\bar{x}}(\Lambda_q - \Lambda_0)\psi(\cdot, k)d\sigma, \tag{4.16}$$

which is given in *Theorem 5* from [64].

This bring us to the fourth step, defining and solving the D-bar equation which relates the scattering transform to the Faddeev solution (4.3). *Theorem 2.1* of [64] gives us the form of the D-bar equation that we need

$$\frac{\partial}{\partial\bar{k}}\mu(x, k) = \frac{1}{4\pi\bar{k}}t(k)e_{-k}(x)\overline{\mu(x, k)}, \quad k \neq 0, \tag{4.17}$$

which is the differential for the Lippmann-Schwinger equation. Next, *Theorem 4.1* of [64] shows that (4.17) is uniquely solvable and the solution satisfies

$$\mu(x, k) = 1 + \frac{1}{(2\pi)^2}\int_{\mathbb{R}^2} \frac{t(k')}{(k - k')\bar{k}'}e_{-x}(k')\overline{\mu(x, k')}dk_1'dk_2' \tag{4.18}$$

for all $k \in \mathbb{C}\backslash 0$, $x \in \mathbb{R}^2$. Note that the integral is taken over the k-plane, so to solve (4.18), $\mu(x, k)$ is needed for all values of $k \in \mathbb{C}\backslash 0$.

The final step in [64] is to evaluate the (absolutely convergent) integral formula

$$\gamma^{\frac{1}{2}}(x) = 1 + \frac{1}{8\pi^2 i}\int_{\mathbb{C}} \frac{t(k)}{|k|^2}e_{-x}(k)\overline{\mu(x, k)}(-2i)dk_1dk_2. \tag{4.19}$$

In practice we skip this step by noting that we can just take the limit as $k \to 0$ of (4.18) to recover γ, i.e.

$$\lim_{k \to 0} \mu(x,k) = \gamma^{\frac{1}{2}}(x). \tag{4.20}$$

Note that in the solution of the D-bar equation x is kept fixed, so the computation can be carried out only in the region of interest. Further, discussion on the limit in (4.20) is shown in Appendix B.6.

4.2 Summary: The Steps

In summary, the main steps of our algorithm based on the algorithm of A. Nachman [64] are:

1. Compute γ and $\frac{\partial \gamma}{\partial \nu}$ on the boundary, and reduce the problem to one with $\gamma \equiv 1$ in neighborhood of the boundary.

2. Compute the trace on $\partial\Omega$ of the function $\psi(\cdot, k)$ from the boundary data using equation (4.15).

3. Compute the scattering transform $t(k)$ using equation (4.16).

4. Compute $\mu(x,k)$ by using (4.18) to solve the D-bar equation (4.17).

5. Reconstruct $\gamma(x)$ using equation (4.20).

We see that the only steps involving boundary information are steps 1, 2 & 3. Therefore we have only studied these steps and used previous implementations of steps 4 and 5 in order to get reconstructions. Specifically, we use results from [46].

4.3 Discussion on Steps 1 & 2

In this dissertation we do not implement Nachman's first to steps. This section discusses the reasons and methods used in their place.

4.3.1 Step 1: Conductivity on the boundary

The vast majority of the results shown assume as in [71], [60], [59], and [62] that $\gamma \equiv const$ in a neighborhood of the boundary. The assumption clearly implies $\frac{\partial \gamma}{\partial \nu} = 0$. This simplification has provided good results in the works cited above.

Currently, there has been no implementation of Nachman's first step, i.e. the calculation of (4.4) and (4.5). An approximation of γ and $\frac{\partial \gamma}{\partial \nu}$ is given in [65]. In Chapter 10 we use the method of layer-stripping to construct the conductivity and its normal derivative at the boundary. In the remainder of this section we will assume that $\gamma \equiv const$.

4.3.2 Step 2: ψ on the boundary

In order to find ψ on the boundary we look to *Theorem 5* of [64] which states that $\psi(x,k)$ satisfies the following integral equation

$$\psi(\cdot,k)|_{\partial\Omega} = e^{ikx} - S_k(\Lambda_\gamma - \Lambda_1)\psi(\cdot,k). \tag{4.21}$$

The operator $I + S_k(\Lambda_\gamma - \Lambda_1)$ is invertible and therefore $\psi(\cdot,k)$ can be calculated on the boundary. The numerical solution of (4.21) is not stable if the data is noisy [59]. Thus we instead approximate ψ in some stable way.

We observe by *Theorem 1.1* from [64] we have that for any $k \in \mathbb{C}\backslash 0$, there is a unique solution of ψ of

$$(-\Delta + q)\psi(\cdot,k) = 0 \tag{4.22}$$

satisfying

$$e^{-ikx}\psi(x,k) - 1 \in W^{1,\tilde{p}}. \tag{4.23}$$

In the sense of (4.23), ψ is asymptotic to e^{ikx} for large $|x|$. Therefore, we choose $\psi \approx e^{ikx}$ for $x \in \partial\Omega$. This assumption on ψ was used in [60], [59], [46], [37], [38], and [62]. It has been shown to provide good conductivity reconstructions, and we therefore are confident with taking the assumption in this study as well.

Chapter 5

COMPUTATION OF THE SCATTERING TRANSFORM

In this section, we want to derive an approximation to the scattering transform from experimental data. The following derivation is based on the work from [37] in which the domain was chosen to be a circle. In this derivation we allow the boundary to be a parameterized single-valued function. This boundary function is valid as long as it is Lipschitz continuous, but our numerical implementation requires C^1 boundaries. We begin with

$$t^{exp}(k) := \frac{1}{\gamma_b} \int_{\partial\Omega} e^{i\bar{k}\bar{z}} \left(\Lambda_\gamma - \Lambda_1\right) e^{ikz} d\sigma(z)., \tag{5.1}$$

γ_b refers to a constant guess for the boundary conductivity and the exp refers to the assumption of $\psi \approx exp(ikx)$ that we use.

We first scale the boundary. This is just a numerical concern. Experimentally it has been found if the radius is too big or too small the calculations break down. We can use the relation $\tilde{\Lambda}_\gamma = b\Lambda_\gamma$ in order to scale the domain, $\tilde{\Lambda}_\gamma$ is the Dirichlet-to-Neumann map for the scaled domain and Λ_γ is the map for the experiment/simulated domain. The details of the calculation are shown in Appendix B.7. Our scaled scattering transform can be written as

$$t_{sc}^{exp}(k) = \frac{b}{\gamma_b} \int_{\partial\tilde{\Omega}} e^{i\bar{k}\bar{z}} \left(\Lambda_\gamma - \Lambda_1\right) e^{ikz} d\sigma(z). \tag{5.2}$$

As in [37], we expand e^{ikz} in a Fourier series with $z = r(\theta)e^{i\theta}$ to obtain

$$e^{ikz} = \sum_{n=-\infty}^{\infty} a_n(k) r^n(\theta) e^{in\theta} \text{ with } a_n(k) = \begin{cases} \frac{(ik)^n}{n!}, & n \geq 0 \\ 0, & n < 0 \end{cases}.$$

We can see that this equation makes sense by writing down the Taylor expansion for e^{ikz} where $z = re^{i\theta}$. Next we define the inner product $\langle f, g \rangle$ by

$$\langle f, g \rangle = \int_0^{2\pi} \overline{f(\theta)} g(\theta) d\theta. \tag{5.3}$$

In order to express $d\theta$ we use the relation

$$d\sigma(z) = s(\theta)d\theta = \sqrt{(r(\theta))^2 + (r'(\theta))^2}\, d\theta,$$

bearing in mind the $r(\theta)$ refers to the scaled domain. We then substitute the series for e^{ikz} into (5.2) which gives

$$t_{sc}^{exp}(k) = \frac{b}{\gamma_b} \sum_{n=0}^{\infty} \sum_{n=0}^{\infty} a_m(\bar{k}) a_n(k) \langle s(\theta) r^m(\theta) e^{im\theta}, (\Lambda_\gamma - \Lambda_1)(r^n(\cdot)e^{in\cdot})(\theta) \rangle. \tag{5.4}$$

Since $\Lambda_{\gamma,r} = R_{\gamma,r}^{-1}$,we have that

$$\begin{aligned} \langle s(\theta) r^m(\theta) e^{im\theta}, \Lambda_\gamma (r^n(\cdot)e^{in\cdot})(\theta) \rangle &= \tfrac{1}{A} \langle s(\theta) r^m(\theta) e^{im\theta}, A\Lambda_\gamma (r^n(\cdot)e^{in\cdot})(\theta) \rangle \\ &= \tfrac{1}{A} \langle s(\theta) r^m(\theta) e^{im\theta}, A R_\gamma^{-1} (r^n(\cdot)e^{in\cdot})(\theta) \rangle \\ &= \tfrac{1}{A} \langle s(\theta) r^m(\theta) e^{im\theta}, \left(\tfrac{R_\gamma}{A}\right)^{-1} (r^n(\cdot)e^{in\cdot})(\theta) \rangle, \end{aligned}$$

where A is the area of an electrode.

For the functions u,w of $\theta, u, w : \mathbb{R} \to \mathbb{R}$, let $(u(\cdot), w(\cdot))_L$ denote the discrete inner product defined by

$$(u(\cdot), w(\cdot))_L = \sum_{l=1}^{L} \overline{u(\theta_l)} w(\theta_l).$$

Using the discrete inner product we have

$$\langle s(\theta) r^m(\theta) e^{im\theta}, \Lambda_\gamma (r^n(\cdot)e^{in\cdot})(\theta) \rangle \approx \frac{\Delta\theta}{A} (s(\cdot) r^m(\cdot) e^{im\cdot}, \left(\frac{R_\gamma}{A}\right)^{-1} (r^n(\cdot)e^{in\cdot}))_L, \tag{5.5}$$

where $\Delta\theta = \frac{2\pi}{L}$. The division of the Neumann-to-Dirichlet map by A and the use of discrete inner product treats the electrodes in the gap model sense.

Using Euler's formula $e^{in\theta_l} = cos(n\theta_l) + isin(n\theta_l)$ gives

$$(s(\cdot)r^m(\cdot)e^{im\cdot}, \left(\frac{R_\gamma}{A}\right)^{-1}(r^n(\cdot)e^{in\cdot}))_L =$$

$$\left(s(\cdot)r^m cos(m\cdot) + is(\cdot)r^m sin(m\cdot), \left(\frac{R_\gamma}{A}\right)^{-1}[r^n cos(n\cdot) + ir^n sin(n\cdot)]\right)_L \tag{5.6}$$

One can expand (5.6) into four terms where each term is calculated in the same basic way. Therefore, we will only show details for the term

$$(s(\cdot)r^m(\cdot)cos(m\cdot), \left(\frac{R_\gamma}{A}\right)^{-1}[r^n(\cdot)cos(n\cdot)])_L, \tag{5.7}$$

in the following two subsections.

5.1 Unit Circle Model with TCPs

In this subsection we assume the boundary is a circle as in [37] and the CPs applied are TCPs. The TCPs, denoted $T^k(\theta)$ are defined by (2.3) in Section 2.3.4. In terms of the calculation all we do is set $r \equiv 1$ and continue computing. Effects of this assumption on a non-circular domain will be discussed later. This assumption/model is called the unit circle model, UCM.

The derivation for this assumption proceeds as follows. We will use normalized vectors in the derivation defined as

$$\phi^k \equiv \frac{T^k(\theta)}{||\mathbf{T}^k||_2}, \tag{5.8}$$

where we define the vectors

$$\mathbf{T}^k = [T^k(\theta_1) \ ... \ T^k(\theta_L)]^T. \tag{5.9}$$

Now let us consider the term (5.7). We get

$$\begin{aligned}(cos(m\cdot), \left(\frac{R_\gamma}{A}\right)^{-1}(cos(n\cdot)))_L &= (\frac{T^m}{M}, \left(\frac{R_\gamma}{A}\right)^{-1}\frac{T^n}{M})_L, \\ &= (\frac{\phi^m\|\mathbf{T}^m\|_2}{M}, \left(\frac{R_\gamma}{A}\right)^{-1}\frac{\phi^n\|\mathbf{T}^n\|_2}{M})_L, \\ &= \frac{\|\mathbf{T}^m\|_2\|\mathbf{T}^n\|_2}{M^2}(\phi^m, \left(\frac{R_\gamma}{A}\right)^{-1}\phi^n)_L.\end{aligned}$$

We define

$$(\phi^m, \left(\frac{R_\gamma}{A}\right)^{-1}\phi^n)_L \equiv \left(R_\gamma^M\right)^{-1}(m,n) = L_\gamma(m,n). \tag{5.10}$$

The expression (5.10) represents our numerical approximation to the Dirichlet-to-Neumann map. Considering there are $L-1$ independent CPs, the map L_γ is rank $L-1$. Overall we have

$$(cos(m\cdot), \left(\frac{R_\gamma}{A}\right)^{-1}(cos(n\cdot)))_L \approx \frac{\|\mathbf{T}^m\|_2\|\mathbf{T}^n\|_2}{M^2}L_\gamma(m,n) \tag{5.11}$$

We show further details of the calculation of $L_\gamma(m,n)$ from measured voltages in Appendix B.8.

5.2 Parameterized Boundary Model

In this approximation we will now take into account the radius term. We will call this method PBM denoting the parameterized boundary model. We can include the radius term by using a Fourier series for the terms $r^n(\theta)cos(n\theta)$ or $r^n(\theta)sin(n\theta)$ and $s(\theta)r^m(\theta)cos(m\theta)$ or $s(\theta)r^m(\theta)sin(m\theta)$. Note that this calculation allows for any CPs to be used. The CPs will still be referred to as T. The Fourier series allows us to pull out constants giving us the ability to get the same form of the Dirichlet-to-Neumann map, (5.10), for the specified applied current.

Let's look at the first of the terms, (5.7). The Fourier series is given by

$$s(\theta)r^m(\theta)cos(m\theta) = \sum_{j=1}^{\infty} a_{m,j}T(j\theta), \tag{5.12}$$

and

$$r^n(\theta)cos(n\theta) = \sum_{k=1}^{\infty} c_{n,k}T(k\theta), \tag{5.13}$$

where we define

$$a_{m,j} = \frac{1}{\|T(j\theta)\|^2_{L^2([-\pi,\pi])}} \int_{-\pi}^{\pi} \left(s(\theta)r^m(\theta)cos(m\theta)\right) T(j\theta)d\theta,$$

$$c_{n,k} = \frac{1}{\|T(k\theta)\|^2_{L^2([-\pi,\pi])}} \int_{-\pi}^{\pi} \left(r^n(\theta)cos(n\theta)\right) T(k\theta)d\theta.$$

It should be noted that in order for existence and uniqueness of the problem the zeroth order coefficients are set to zero. If we look back to the first term of (5.6) we have that

$$(s(\cdot)r^m(\cdot)cos(m\cdot), \left(\frac{R_\gamma}{A}\right)^{-1} (r^n(\cdot)cos(n\cdot)))_L$$

$$= \left(\sum_{j=1}^{\infty} a_{m,j}T(j\theta), \left(\frac{R_\gamma}{A}\right)^{-1} \left(\sum_{k=1}^{\infty} c_{n,k}T(k\theta)\right)\right)_L.$$

We know that the operator $\left(\frac{R_\gamma}{A}\right)^{-1}$ is independent of any constant. This will allow the operator to act on the CPs. We will also approximate the infinite sum with finite sums based on the number of CPs, N_{CP}, for the specific CPs used. Thus, these constraints gives us the definition $\hat{L}_\gamma$

$$\hat{L}_\gamma(m,n) \equiv \left(\sum_{j=1}^{N_{CP}} a_{m,j}\|\mathbf{T}^j\|_2\phi^j, \sum_{k=1}^{N_{CP}} c_{n,k}\|\mathbf{T}^k\|_2 \left(\frac{R_\gamma}{A}\right)^{-1} \phi^k\right) \tag{5.14}$$

In order to compute $\hat{L}_\gamma$ we want to express it with respect to L_γ. Thus we get

$$\hat{L}_\gamma(m,n) = \sum_{j=1}^{N_{CP}} \sum_{k=1}^{N_{CP}} \left(a_{m,j}\|\mathbf{T}^j\|_2\right) \left(\phi^j, \left(\frac{R_\gamma}{A}\right)^{-1} \phi^k\right) \left(c_{n,k}\|\mathbf{T}^k\|_2\right)$$

$$= \sum_{j=1}^{N_{CP}} \sum_{k=1}^{N_{CP}} \left(a_{m,j}\|\mathbf{T}^j\|_2\right) L_\gamma(j,k) \left(c_{n,k}\|\mathbf{T}^k\|_2\right)$$

In order to simplify computation and notation we define two matrices A and C both of size $N_{CP} \times N_{CP}$ as

$$A(i,j) = a_{i,j}\|T^j\|_2 \quad \text{and} \quad C(i,j) = c_{i,j}\|T^j\|_2. \tag{5.15}$$

This leads to a very concise matrix equation,

$$\hat{L}_\gamma = AL_\gamma C^T. \tag{5.16}$$

In summary we have

$$(s(\cdot)r^m(\cdot)cos(m\cdot), \left(\frac{R_\gamma}{A}\right)^{-1}(r^n(\cdot)cos(n\cdot)))_L \approx \hat{L}_\gamma = AL_\gamma C^T.$$

5.3 Conclusion of the calculation of t^{exp}

In this section we conclude the calculation of the scattering transform t^{exp}. We let

$$\delta L_{m,n} \equiv \begin{cases} \frac{\|\mathbf{T}^m\|_2 \|\mathbf{T}^n\|_2}{M^2}\left(L_\gamma(m,n) - L_1(m,n)\right), & \text{for UCM,} \\ \left(\hat{L}_\gamma(m,n) - \hat{L}_1(m,n)\right), & \text{for PBM.} \end{cases} \tag{5.17}$$

Then from (5.4),(5.5), and (5.17) we have

$$\begin{aligned} t_{sc}^{exp}(k) &\approx \frac{b\Delta\theta}{A\gamma_b}\sum_{m=0}^{\infty}\sum_{n=0}^{\infty} a_m(\bar{k})a_n(k)\left(s(\cdot)r^m(\cdot)e^{im\theta}, \left[\left(\frac{R_\gamma}{A}\right)^{-1} - \left(\frac{R_1}{A}\right)^{-1}\right](r^n(\cdot)e^{in\cdot})\right)_L \\ &= \frac{b\Delta\theta}{A\gamma_b}\sum_{m=0}^{\infty}\sum_{n=0}^{\infty} a_m(\bar{k})a_n(k)\delta L_{m,n}. \end{aligned}$$

After somewhat lengthy calculations, shown in Appendix B.9, we arrive at our approximation of the scattering transform

$$\begin{aligned} t_{sc}^{exp}(k) = \frac{b\Delta\theta}{A\gamma_b}\Bigg(&\sum_{m=1}^{\frac{L}{2}-1}\sum_{n=1}^{\frac{L}{2}-1} a_m(\bar{k})a_n(k)\left(\delta L_{m,n} + \delta L_{m+\frac{L}{2},n+\frac{L}{2}}\right. \\ &\left. + i\left(\delta L_{m,n+\frac{L}{2}} - \delta L_{m+\frac{L}{2},n}\right)\right) + \sum_{n=1}^{\frac{L}{2}-1} a_{\frac{L}{2}}(\bar{k})a_n(k)\left(\delta L_{\frac{L}{2},n} + i\delta L_{\frac{L}{2},n+\frac{L}{2}}\right) \\ &+ \sum_{m=1}^{\frac{L}{2}-1} a_m(\bar{k})a_{\frac{L}{2}}(k)\left(\delta L_{m,\frac{L}{2}} - i\delta L_{m+\frac{L}{2},\frac{L}{2}}\right) + a_{\frac{L}{2}}(\bar{k})a_{\frac{L}{2}}(k)\delta L_{\frac{L}{2},\frac{L}{2}}\Bigg). \end{aligned} \tag{5.18}$$

Let us now summarize. We have found a computable form of t^{exp} defined as (5.18), although we are in fact computing a scaled version, t_{sc}^{exp}. Thus leads to a numerical solution of (4.16) and it is now possible to compute the solution of the D-bar equation, (4.18). Since we compute a scaled scattering transform we need only reconstruct the D-bar equation on that corresponding domain.

5.4 Note on Difference and Static images

In the context of the D-bar method difference and static images differ from the conventional definitions. Assuming that Λ_γ is constructed from measured data, we make the following definitions.

Definition 5.4.1. ***Static Image*** *is a reconstruction that results from Λ_1 constructed from simulated voltages corresponding to a homogeneous domain.*

Definition 5.4.2. ***Difference Image*** *is a reconstruction that results from Λ_1 constructed from measured voltages. The voltages correspond to a homogeneous or inhomogeneous conductivity. We denote the resulting scattering transform t_{diff}^{exp}.*

In the conventional definition of the static image, Definition 2.2.1, there is no reference to simulated data. In Definition 5.4.1 we explicitly note that we use simulated data to produce Λ_1.

The main point of this section is to clarify the distinction between the definitions for difference images. In Definition 2.2.2 it is assumed the differencing happens after the reconstruction process, i.e. $\gamma_1^{recon} - \gamma_2^{recon}$. Comparatively, in the context of the D-bar method the differencing occurs

earlier, specifically in our scattering transform. When we refer to difference images in this dissertation we will be referring to Definition 5.4.2 unless explicitly stated.

Chapter 6

NON-CIRCULAR RECONSTRUCTIONS

In this chapter we illustrate three series of conductivity reconstructions. The first set is reconstructions on an oval tank from ACT 3 data. The second series is of simulated reconstructions on a simulated chest. The final reconstructions are performed on a human chest from ACT 3 data. We show limited success in this final set. One major setback is the lack of boundary information from the measured voltages. It should be noted, in this chapter, all reconstructions use TCPs. Nevertheless, the reconstructions presented here show improvements from previous works.

6.1 Reconstructions of an oval tank from ACT 3 data

The following section presents the first reconstructions that we attempted, the results were published in the journal of Physiological Measurement [62]. The reconstructions show the improvement of proper domain modeling and the benefit of using the CEM with FEM. There are two subsections. We describe the experimental setup first, and then illustrate our results in the following subsection.

6.1.1 Description of experiment

In this section difference and static conductivity images are presented for copper (conducting) and PVC (insulating) targets in an elliptical tank using UCM and PBM. One should note that the domain was not a mathematical ellipse, but only an approximation to one. The tank had a major axis of 330 mm and a minor axis of 240 mm. The electrodes were of length 25.4 mm and height of about 46 mm with equal gaps ($\approx$ 2.76 mm) around the inner edge of the tank. The conductivity of the saline was measured to be 383.4 mS/m. The data collection was performed on the ACT3 system [21], a 32-electrode system operating at 28.8 kHz that applies current and measures the real and quadrature components of the voltage on all 32 electrodes simultaneously. The CPs used in the measurements were TCPs. The experimental setup can be seen in Figure 6.1.

6.1.2 Conductivity Reconstructions

A copper pipe of diameter $31mm$ and a PVC pipe of diameter $33mm$ were placed in several locations inside the saline filled tank. Figures 6.3 through 6.8 display difference and static images with the UCM and the PBM for a copper pipe placed $80mm$ on the major axis (Figure 6.3), a PVC pipe placed $60mm$ on the minor axis (Figure 6.5), a PVC pipe placed in the center (Figure 6.7, and a PVC pipe placed $60mm$ on the minor axis and a copper pipe placed $80mm$ on the major axis (Figure 6.8). The actual location of the target is superimposed on the images by plotting a circle of the correct diameter the correct distance from the origin. In the case of the reconstructions on the circle, this gives the location where the target should appear relative to the origin.

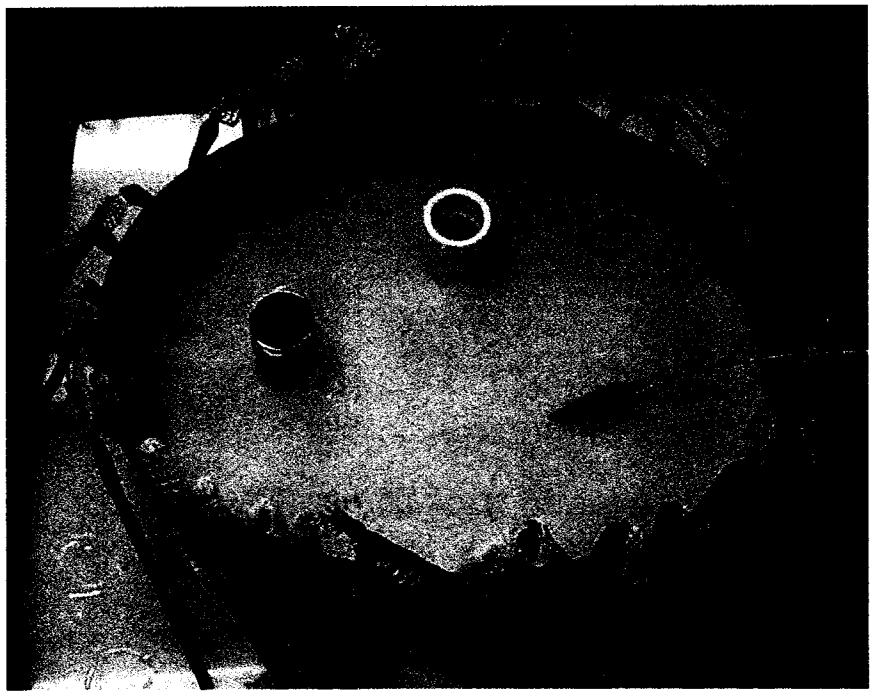

Figure 6.1: ACT 3 experimental setup.

We see consistently that in the difference images using the UCM the targets are visible and are reconstructed in approximately the correct location with some blurring, but substantial artifacts are present. The vertical distortion of the target can be explained by the fact that the current travels through a shorter path in the y-direction than is modeled by the circular domain, and so conductive targets appear in the image to offset this effect. In the difference images using the PBM there are fewer artifacts, the reconstructed target locations are more accurate, and the target shape is more circular in each.

The results are not as consistent for the static images. We see for the UCM in Figure 6.5(c) and Figure 6.8(c) that the reconstructions are successful in obtaining the correct targets, but they have a fair amount of artifacts. However, in Figures 6.3(c) and 6.7(c) one cannot distinguish

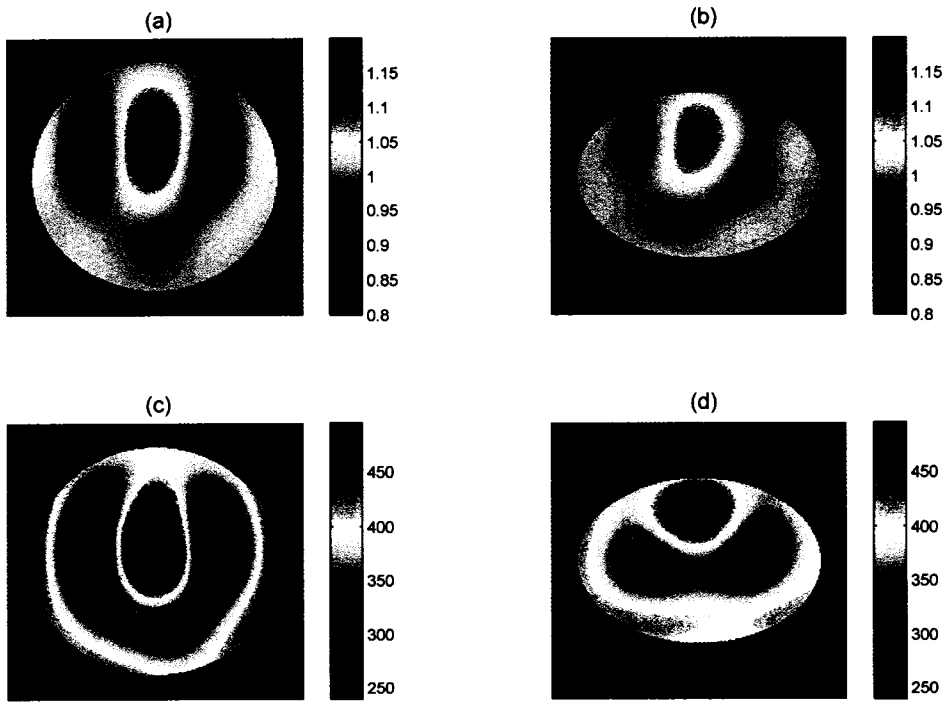

Figure 6.2: In this experiment a copper pipe is placed $60mm$ on the minor axis, represented by the dashed line, (a) and (b) are difference images, (c) and (d) are static images, with conductivity in mS/m, (a) and (c) are UCM results, and (b) and (d) are PBM results.

the targets with any degree of certainty. In the PBM reconstructions the target is visible in each case, but with a blurred shape and some loss of spatial resolution. Artifacts are present in each example, particularly near the boundary, and in Figure 6.3(d) we see a substantial artifact close to the center of the domain. The relative error in L^2 norm between the measured homogeneous tank voltages and the simulated homogeneous tank voltages from the CEM is 3.03%. This discrepancy can be attributed to both modeling and experimental factors and is the cause for these artifacts.

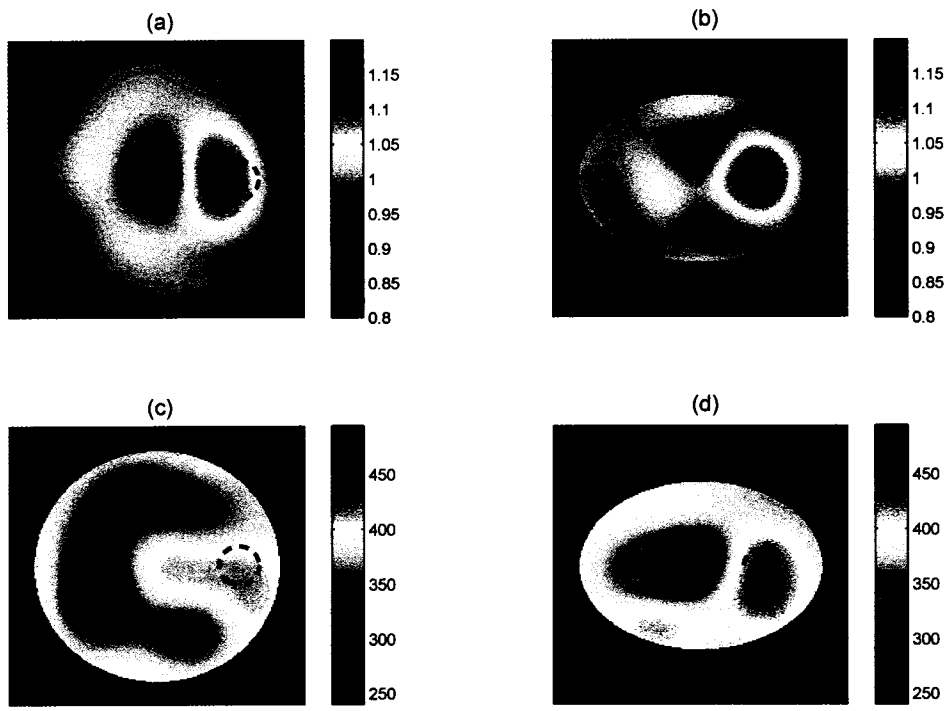

Figure 6.3: In this experiment a copper pipe is placed $80mm$ on the major axis, represented by the dashed line, (a) and (b) are difference images, (c) and (d) are static images, with conductivity in mS/m, (a) and (c) are UCM results, and (b) and (d) are PBM results.

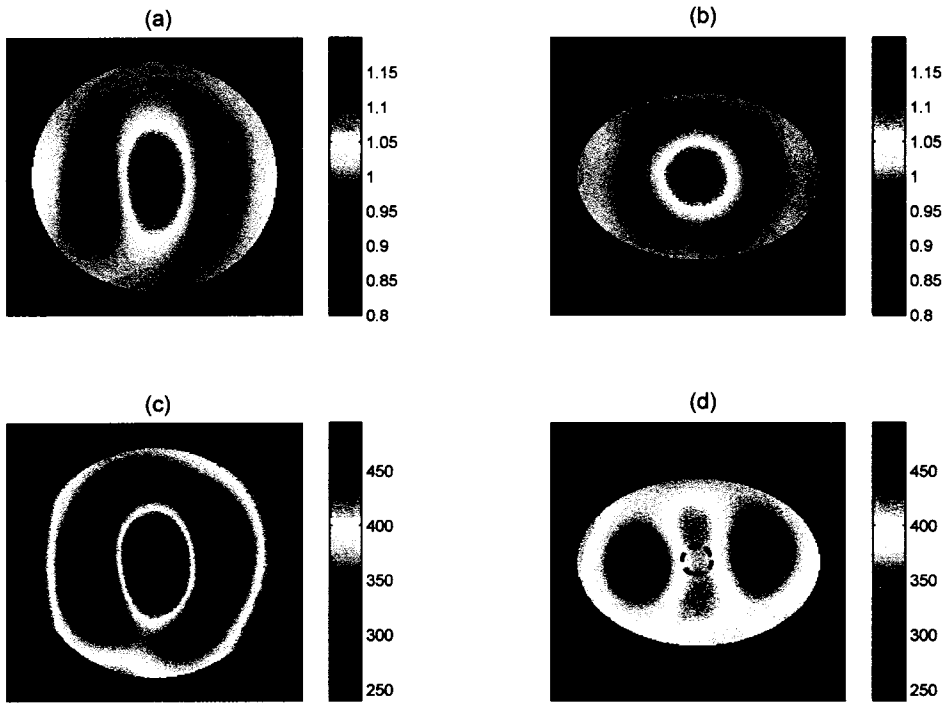

Figure 6.4: In this experiment a PVC pipe placed in the center of the domain, represented by the dashed line, (a) and (b) are difference images, (c) and (d) are static images, with conductivity in mS/m, (a) and (c) are UCM results, and (b) and (d) are PBM results.

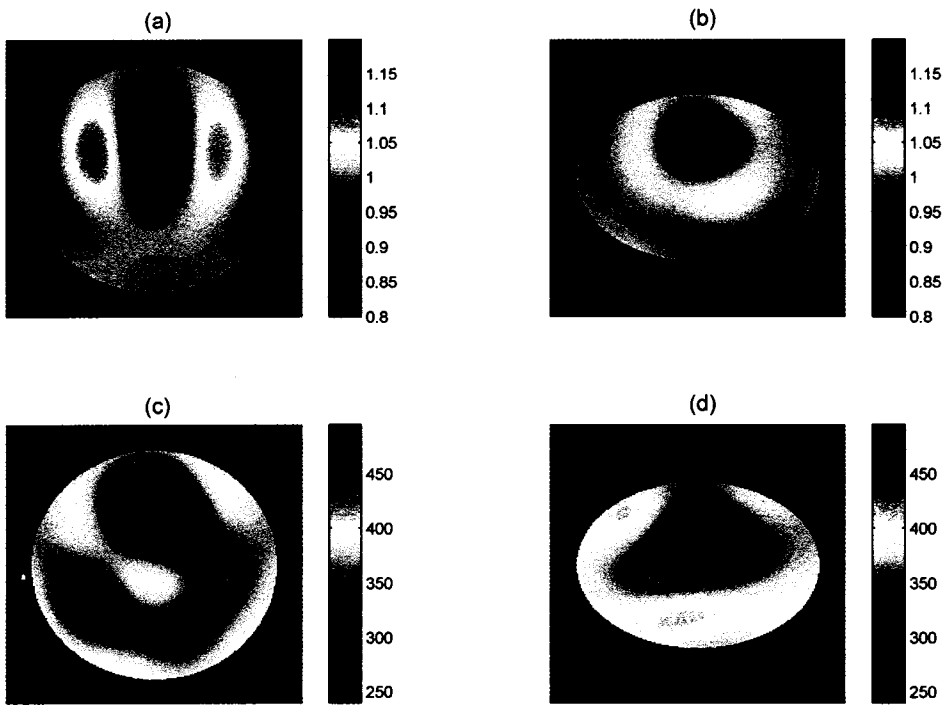

Figure 6.5: In this experiment a PVC pipe is placed $60mm$ on the minor axis, represented by the dashed line, (a) and (b) are difference images, (c) and (d) are static images, with conductivity in mS/m, (a) and (c) are UCM results, and (b) and (d) are PBM results.

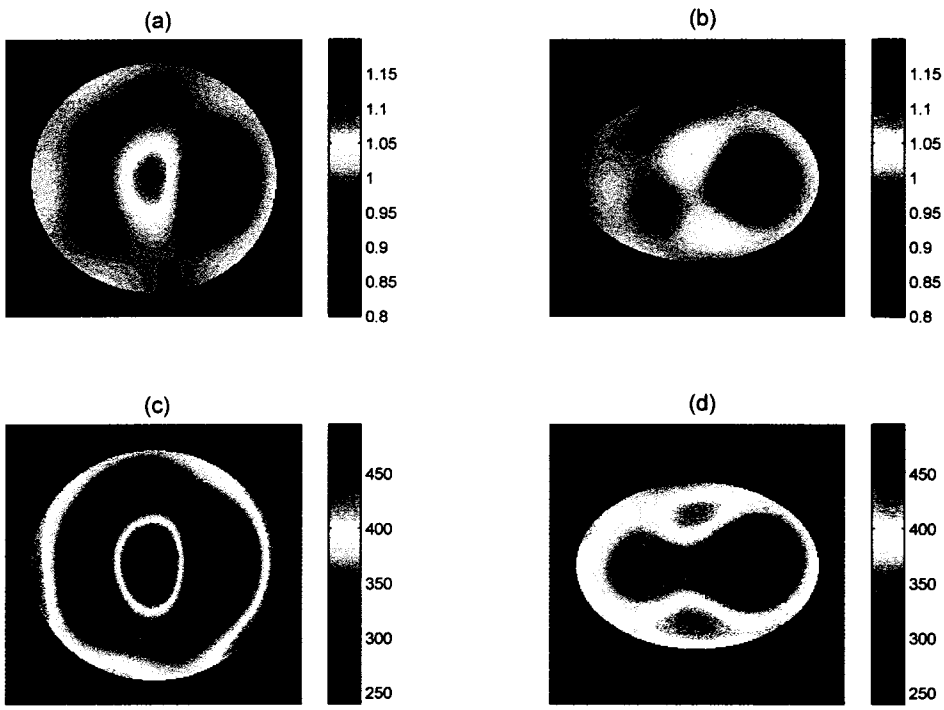

Figure 6.6: In this experiment a PVC pipe is placed $80mm$ on the major axis, represented by the dashed line, (a) and (b) are difference images, (c) and (d) are static images, with conductivity in mS/m, (a) and (c) are UCM results, and (b) and (d) are PBM results.

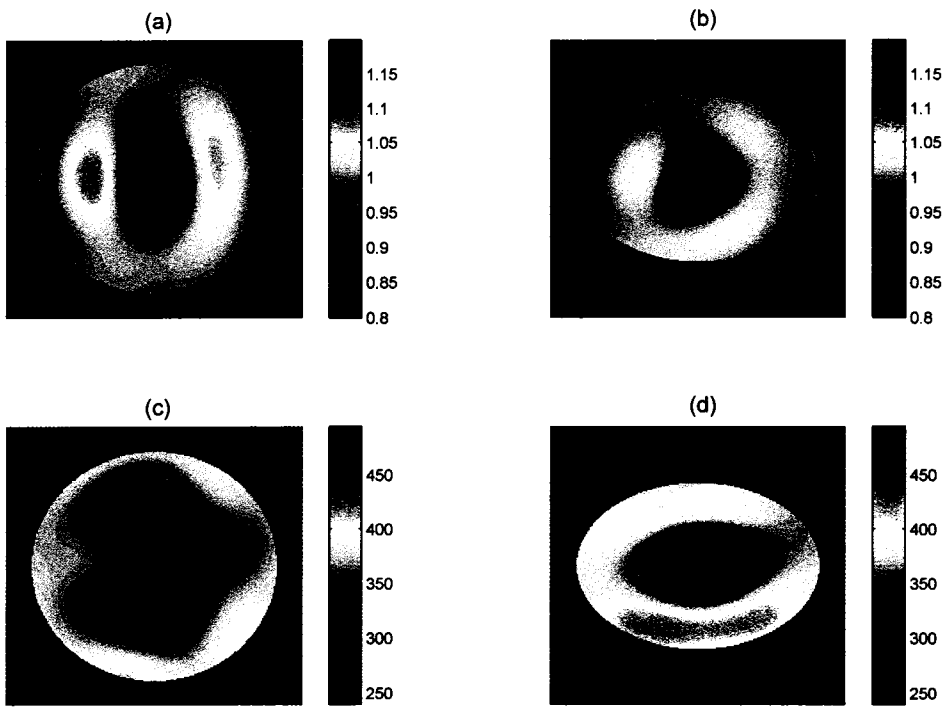

Figure 6.7: In this experiment a PVC pipe placed in the center of the domain, represented by the dashed line, (a) and (b) are difference images, (c) and (d) are static images, with conductivity in mS/m, (a) and (c) are UCM results, and (b) and (d) are PBM results.

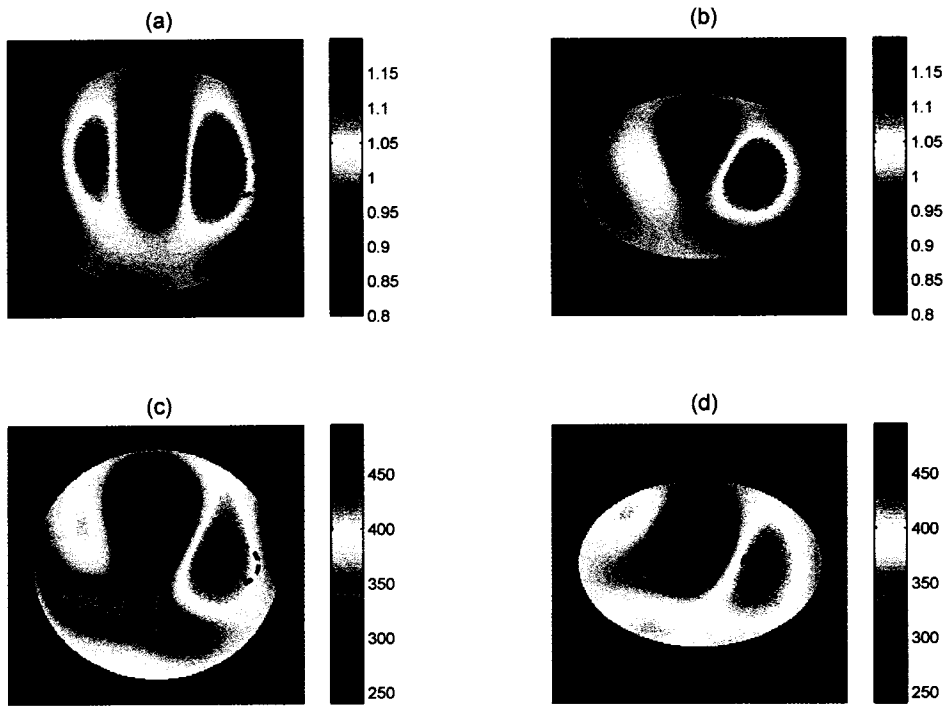

Figure 6.8: In this experiment a PVC pipe placed $60mm$ on the minor axis and a copper pipe placed $80mm$ on the major axis, represented by the dashed line, (a) and (b) are difference images, (c) and (d) are static images, with conductivity in mS/m, (a) and (c) are UCM results, and (b) and (d) are PBM results.

6.2 Reconstructions on a simulated chest

In this section we perform reconstructions on a simulated chest with heart, lungs, and other organs. The reconstructions use FEMCEM generated voltages. Before we show any reconstructions we explain some of the details involved in getting the chest domain and the construction of the mesh.

6.2.1 Details of the Chest-shaped boundary

In the FEMCEM we need to know the exact boundary in order to construct a mesh. We begin this process of obtaining the boundary from a CT scan. The CT scan we used was found on the internet and a picture is shown in Figure 6.9. We see a cross-section in the scan of a human chest. Next, we can import the image into Matlab into a figure file. Although there are much more sophisticated boundary recovery algorithms we simply click on numerous points, $(\vec{r}^{meas}, \vec{\theta}^{meas})$, on the boundary and import them into Matlab. The points are shown as x's in the top of Figure 6.9, where the N points have the form

$$\vec{r}^{meas} = [r_1^{meas} r_2^{meas} \cdots r_N^{meas}]^T \tag{6.1}$$

and

$$\vec{\theta}^{meas} = [\theta_1^{meas} \theta_2^{meas} \cdots \theta_N^{meas}]^T. \tag{6.2}$$

The next step is to take the measurements and construct a parameterized boundary function, $r(\theta)$. The resulting function we found is shown in the bottom of Figure 6.10. We have also added in the lungs and heart. In order to obtain this function we use a Fourier series. The details of the

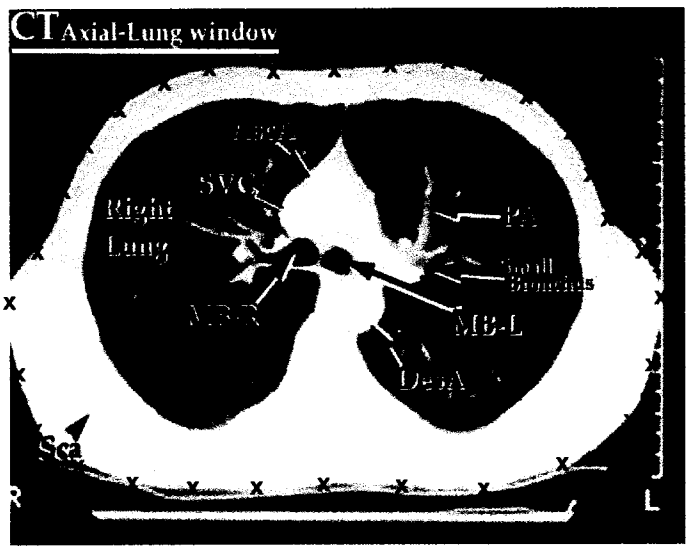

Figure 6.9: CT scan of a human chest with measured points marked with red x's.

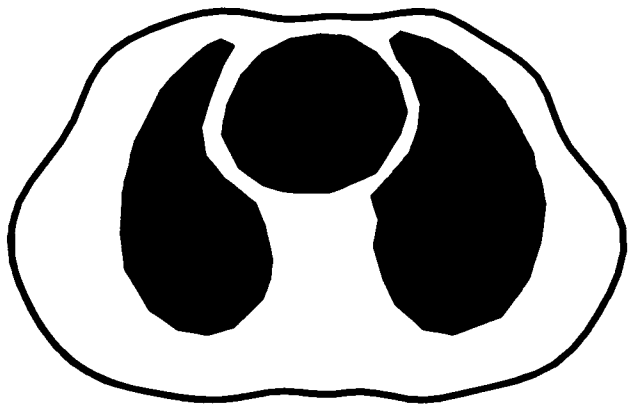

Figure 6.10: The recovered boundary, heart and lungs from the CT scan.

derivation were found in Hemant Jain's Phd thesis [40] and in addition are shown in Appendix C.2. The method takes a Fourier series of the form

$$r(\theta) = r_0 + \sum_{m=1}^{M} (a_m^c cos(m\theta) + a_m^s sin(m\theta)). \tag{6.3}$$

and minimizes the difference between $r(\theta)$ and $\vec{r}^{meas}$ in a least squares sense.

Although we only construct simulated chests, this method could be applied to human voltage measurements and the subject's corresponding CT scan. The boundary information from the CT scan would then be used to construct homogeneous voltage measurements and to calculate the scattering transform on the proper domain.

6.2.2 Description of the Mesh

The next step in the simulation process is the construction of the mesh for FEMCEM. The mesh is constructed with the help of a free Matlab softward package called DistMesh [68]. The software uses Delaunay triangulation and optimizes the node locations by a force-based smoothing procedure. The code attempts to make the triangle equilateral with a $h(x, y)$ function defined by the user specifying triangle size. Here h is the longest edge of a triangle. We present in Figure 6.11 the $h(x, y)$ constructed for two domains and in Figure 6.12 the corresponding mesh generated by DistMesh. After the meshes are constructed we simulate voltages with the FEMCEM for inhomogeneous and homogeneous conductivities. Then we are, finally, ready to perform reconstructions.

6.2.3 Reconstructions: heart and lungs

In this section we present the results of reconstructions for the simulated chest-shaped domain with heart and lungs. The simulated chest has

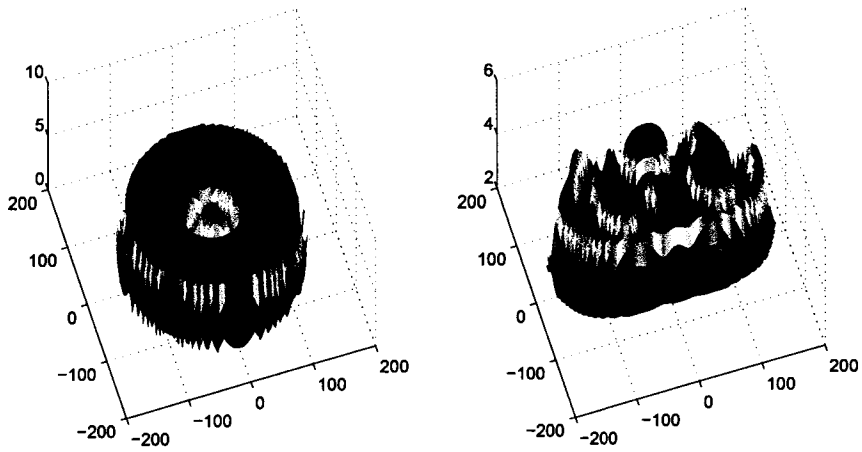

Figure 6.11: H-function defined on the a circular domain with a circular inclusion in the center and a chest-shaped domain with heart, lungs, ribs/spine, and aorta.

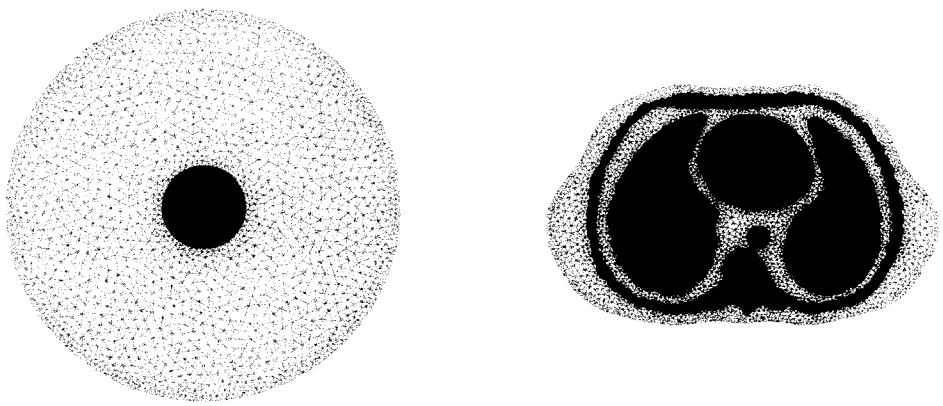

Figure 6.12: Mesh constructed by DistMesh for a circular domain with a circular inclusion in the center and a chest-shaped domain with heart, lungs, ribs/spine, and aorta.

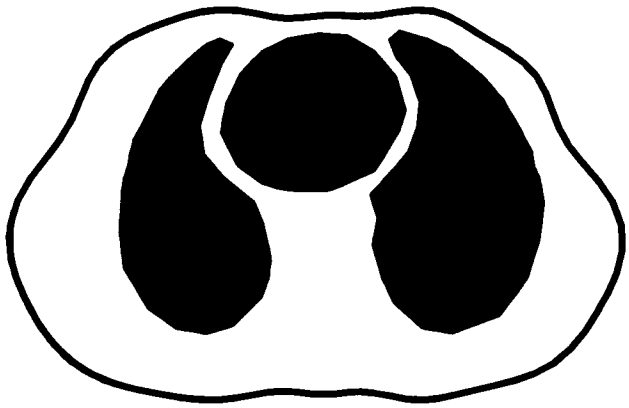

Figure 6.13: Simulated chest domain used in the tests.

32 electrodes, L, and a perimeter of 900 mm, seen in Figure 6.13. The 900mm was the measured perimeter for the person's chest from [38], and is roughly an average chest perimeter. The electrodes are $25.4mm \times 25.4mm$, leaving small gaps We let the current amplitude be $M = 1mA$. We use scaled conductivity values in this section. The background, γ_0, is set to 1. The lungs have a conductivity, γ_{lung}, of $\frac{1}{3}$ and the heart has a conductivity, γ_{heart}, of 2.

We introduce a different kind of calculation using TCPs called discete TCPs or dTCPs. It was found experimentally that if we compute the coefficients to the Fourier series discretely in the scattering transform from the electrodes then we obtain improved reconstructions. That is, the calculations of the matrices A and C, (5.15) are performed in two different ways. When we refer to TCP reconstructions we calculated (5.15) assuming the CPs are continuous functions. In contrast the dTCP calculation assumes

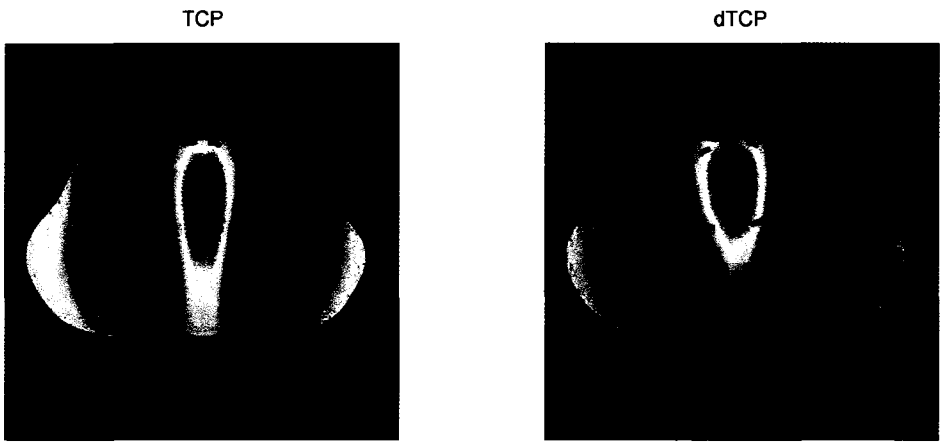

Figure 6.14: Reconstruction of smooth versus discrete assumption in CPs in t^{exp} calculation.

only knowledge of the CP's value at each electrode. Thus in the case of 32 electrodes we have for each coefficient of the Fourier series in (5.15) we calculate a 32 term Riemann sum.

In Figure 6.14 we see the results of the heart and lungs reconstructions and a comparison between TCPs and dTCPs. The scale of values in the figure is from 1/3 to 2. We see in Figure 6.14 not only an increased spatial clarity, but a reduction of artifacts on the far left and right sides of the TCPs reconstruction. We, therefore, will be using the dTCPs for further reconstructions instead of TCPs. In Table 6.2.3 we present the recovered conductivity values and errors of the reconstructions. We take the heart and lung values to be the maximum and minimum of the reconstructions. The truncation radius was tuned to minimize the errors with respect to the heart and lung values. We see a clear improvement in numerical values in addition to the better spatial resolution using dTCPs. In addition to the comparison between dTCPs and TCPs we see that the D-bar method works well with a chest-shaped domain. We continue with more realistic scenarios in the next section.

Table 6.2.3: Errors in reconstructions for different CPs. Note the abbreviations H - heart, Ls - lungs, and RE - relative error.

CP	R_{trunc}	Max H	Max H RE	Min Ls	Min Ls RE
TCP	2.9	1.94	3.0%	0.20	40%
dTCP	2.6	1.96	2.0%	0.31	10%

6.2.4 Reconstructions: more organs

In this section we present results from reconstructions obtained on a realistic chest setup. We will include the heart, lungs, ribs, spine, muscle, fat, and aorta. The conductivity values that we use are the following; $\gamma_{heart} = 670$, $\gamma_{lungs} = 100$, $\gamma_{bone} = 6$, $\gamma_{musc} = 400$, $\gamma_{fat} = 36$, $\gamma_{aorta} = 750$, and $z = 0.024/\gamma 0$. We divide the the contact impedance by γ_0, where γ_0 is assumed the background or boundary value. This is most commonly muscle in the reconstructions. Figure 6.15 illustrates all of the organs/inclusions in a chest cross-section. All the listed conductivities are in units mS/m. The CPs are chosen to be dTCPs for all the tests. As a practical concern, for the simulations since it's a complex domain we use a fine mesh. Specifically, the mesh had 12,923 nodes, 1035 boundary nodes, and a total of 24,805 triangular elements.

We will take progressive steps eventually reconstructing with all the organs. Our first test has a heart of 670mS/m and lungs of 100mS/m. The reconstruction can be seen in Figure 6.16. The maximum value in the heart is 662.9mS/m, giving a relative error of 1.1% and the lungs have a conductivity of 98.3mS/m resulting in 1.7% error. There is a difference between the reconstruction in Figure 6.16 and Figure 6.14 because the scale is different. That is, the scaled conductivities that would result from this section are $\gamma_{heart} = 1.675$ and $\gamma_{lungs} = 1/4$. If the scaled conductivities

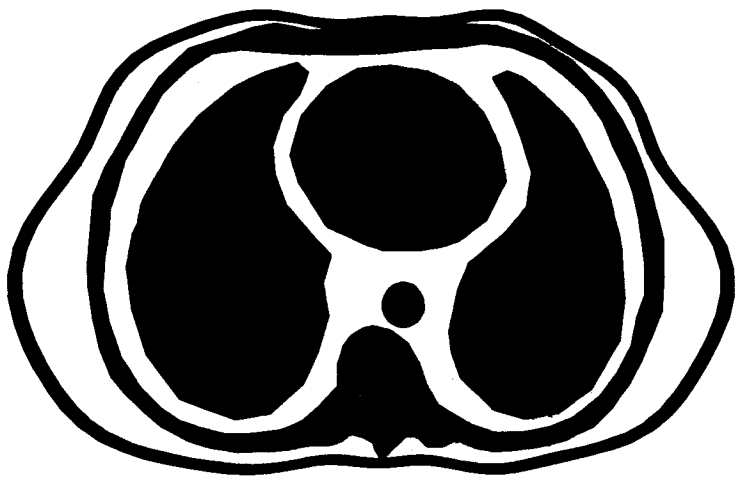

Figure 6.15: Simulated chest domain with heart (red), lungs, (blue), ribs (cyan), muscle (yellow), aorta (small red circle), and skin/fat layer (green).

Figure 6.16: Reconstructions of a heart and lungs with realistic conductivity values of 670mS/m for the heart, 100mS/m for the lungs, and 400mS/m for the background using dTCP. The truncation radius was set to 2.4.

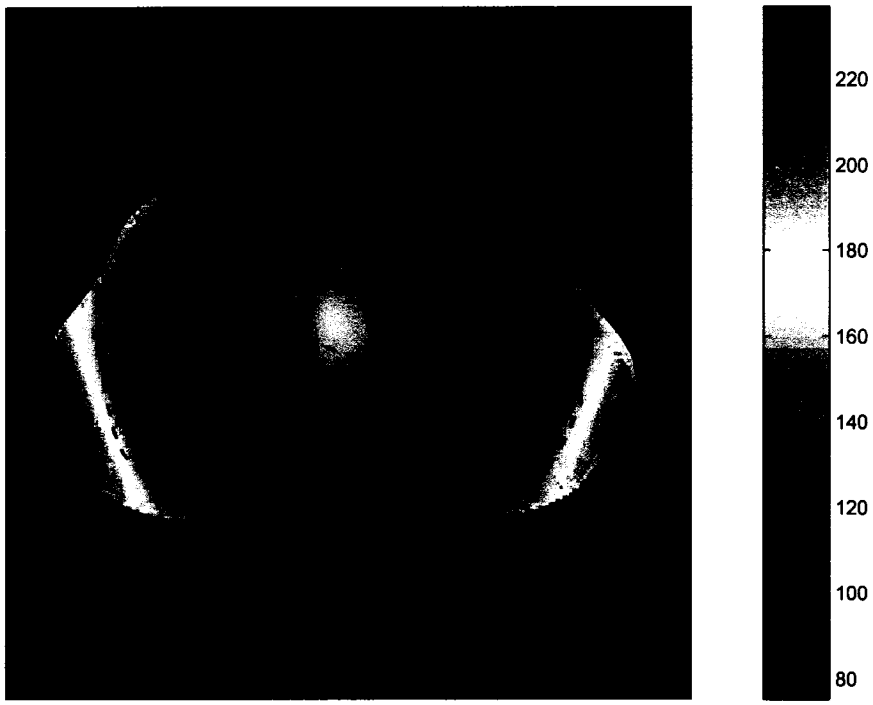

Figure 6.17: Reconstructions of a heart = 670mS/m, lungs = 100mS/m, aorta = 750mS/m, ribs = 6mS/m, and background 400mS/m using dTCP. The truncation radius was set to 2.4.

from this section, 1.675 and 1/4, were the same as the previous, 2 and 1/3, the results should be spatially identical.

This was a straightforward test. Considering the good reconstructions of scaled conductivities we expected this test to work well. We next add the aorta and ribs. In Figure 6.17 we see a reconstruction that attempts to recover the heart, lungs, ribs/spine, and aorta. The conductivity values in Figure 6.17 are very far from the ideal. However, the outline of the heart and lungs can be seen. The inclusion of the ribs in the simulation clearly has a very large effect on the reconstruction. As a follow-up we remove the ribs and see if the D-bar method can pick up the small, but highly conductive, aorta in the center of the domain. In Figure 6.18 we see on the left the reconstruction. It appears that there is absolutely no

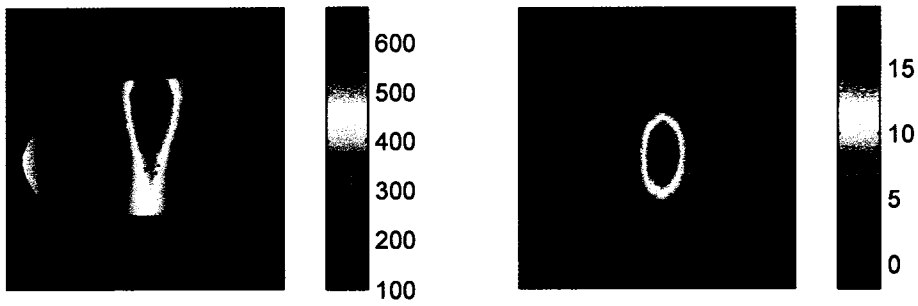

Figure 6.18: Reconstructions of a heart = 670mS/m, lungs = 100mS/m, and aorta = 750mS/m using dTCP on the left. On the right we see the difference between the left and Figure 6.16. The truncation radius was set to 2.4.

aorta recovered. However, if we take the difference between the recovered conductivity in Figure 6.18(left) and Figure 6.16 we get the image on the right of Figure 6.18. So it appears that we can recover, to a limited extent, a very small object in the domain.

The last test we present in this section includes all the features. That is, we simulate the heart, lungs, ribs, aorta, skin/fat layer, and background of muscle. The reconstruction is shown in Figure 6.19. Clearly, this is not a completely successful reconstruction. However, it illustrates the current ability of the method to reconstruct a simulated conductivity of this complexity.

We have tested complex conductivities in this section. Figure 6.17 and Figure 6.19 were less than ideal. However, this does not suggest the approach is without value. For instance, the inclusion of the ribs may be too demanding. Even though the electrodes would have to be placed partially

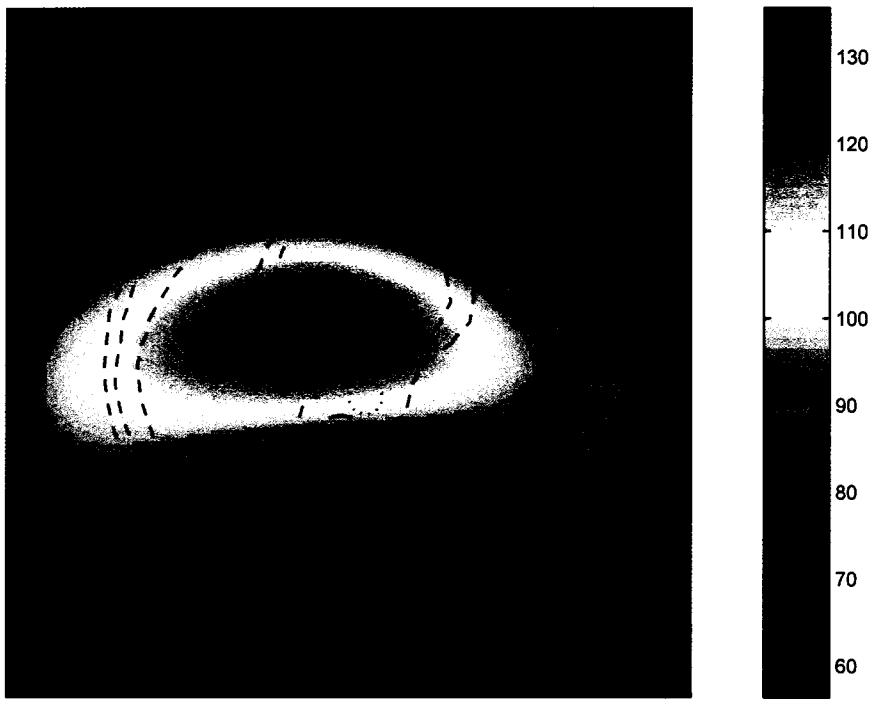

Figure 6.19: Reconstructions of a heart = 670mS/m, lungs = 100mS/m, aorta = 750mS/m, ribs = 6mS/m, skin/fat layer 36mS/m, and background 400mS/m using dTCP. The truncation radius was set to 1.8.

over the ribs there is no reason they would be entirely on the ribs. Clearly, such a large resistivity would diminish the quality of reconstructions inside them. So placing electrodes over ribs should be avoided as much as possible.

6.3 Human Chest Reconstructions

In this section we present reconstructions taken from a human subject using the ACT 3 system. The system is a 32 electrode system as discussed previously. It operates at 28.8kHz. TCP were used with a amplitude of 0.85 mA. The electrodes were 29 mm high by 24 mm wide. The chest had a circumference of 900 mm. A total of 100 frames of data were collected at 18 frames s^{-1}. We present result of one frame (set of voltages) that is used to construct Λ_γ and another frame used in the construction of Λ_1. That is, these reconstructions are difference images.

The difference image on a circular tank is a reproduction of the result shown in [38]. In Figure 6.20 we show the reconstruction on a circle of radius 143 mm. Unfortunately, we do not have any boundary information for the human subject besides the perimeter of 900 mm. As a result, we are not optimistic about reconstructions. Nevertheless, we attempt reconstructions on the chest-shaped domain from the previous section as well as for an ellipse. The chest-shaped domain has an approximate axis ratio 0f 0.71 and the ellipse we use is the one presented in Section 6.1 with an axis ratio of 0.73. The recontruction corresponding to the scattering transform calculated on these domains are shown in Figure 6.21. The reconstructions do not look good. However, the axis ratio and chest-shaped domain corresponding to the CT scan from the internet, which need not correspond to this subject in anyway. We run a search on ellipses varying the axis

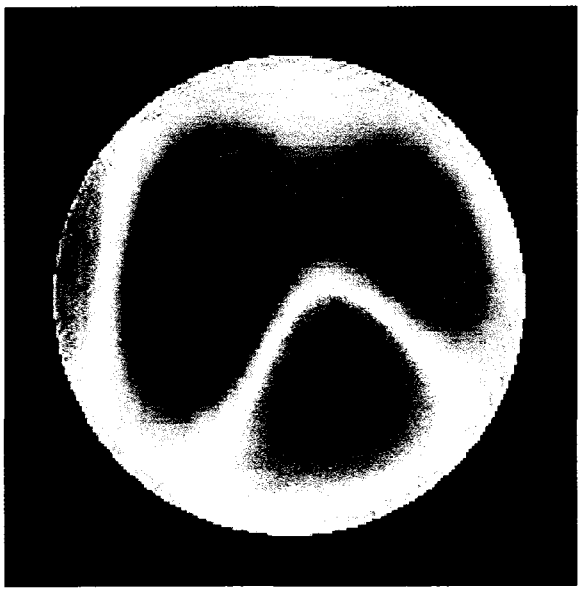

Figure 6.20: Reconstruction of human chest data modeled on a circle.

Figure 6.21: Reconstruction of human chest data modeled on an ellipse with an axis ratio of 0.73 and a chest-shaped domain.

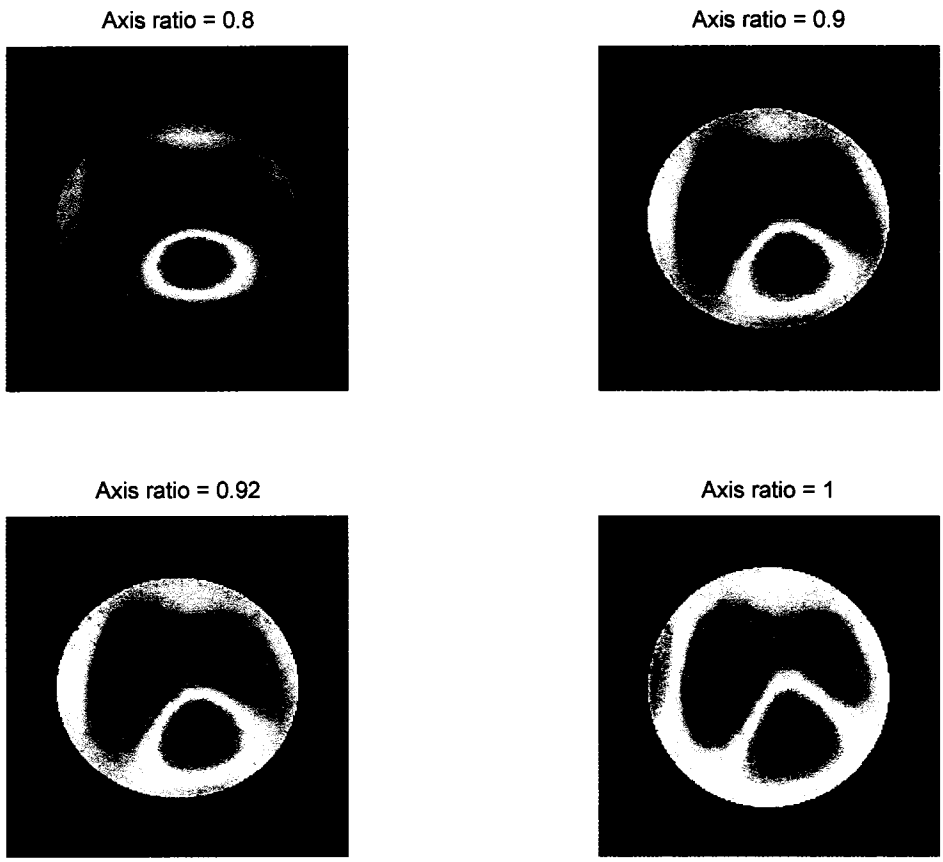

Figure 6.22: Reconstruction of human chest data modeled on several ellipses with different axis ratios.

ratios. We present several of these ellipses in Figure 6.22. It seems that the reconstruction modeled on an ellipse with an axis ratio of either 0.9 or 0.92 is best. Both of these axis ratios reduce the large conductive artifact on the left side of the reconstruction in Figure 6.20. Also the lung shape is more realistic, and the heart does not blur as much into the boundary as seen in the reconstruction on the circle. These reconstructions show modest improvement over the reconstructions on the circle. However, without knowledge of the boundary it is and has been difficult to guess the domain. We put aside reconstructions and begin our discussion on optimal CPs next.

Chapter 7

OPTIMAL CURRENT PATTERNS

In this chapter we discuss the construction of optimal CPs (OCPs) as defined in [35]. We calculate them for any $\mathcal{C}^1$ domain analytically for a small class of inclusions and numerically for any $\mathcal{C}^1$ inclusion. We restrict to a $\mathcal{C}^1$ boundary because in the implementation we require the calculation of the derivative of the parameterized boundary function.

OCPs are constructed in a way to maximize the distinguishability constant defined as

$$\delta \equiv \frac{\left[\sum_{l=1}^{L}\left(V_l^k(\gamma_{test}) - V_l^k(\gamma_0)\right)^2\right]^{\frac{1}{2}}}{\left[\sum_{l=1}^{L}(J_l^k)^2\right]^{\frac{1}{2}}}.$$

This is a quantitative measure of a current pattern's ability to distinguish two different conductivities γ_{test} and γ_0 [39]. It is a normalized measure of the voltage differences. Simply speaking, if the difference between voltages corresponding to two different conductivities is large then the CPs used can distinguish the conductivities 'well'.

The concept of distinguishability was introduced by Isaacson in [35]. Cheney et al found in [15] that eigenfunctions (eigenvectors) of the difference in Neumann-to-Dirichlet maps $R_{\gamma_{test}} - R_{\gamma_0}$ maximizes δ for the conductivity γ_{test}. An obvious concern in the construction of the OCPs is knowledge

of γ_{test}. In practice, i.e. with a physical experiment, one can iteratively find numerical OCPs for unknown conductivities. This approach will be discussed later. If one has only simulated data then γ_{test} must be guessed or assumed.

7.1 Analytic OCPs

The first OCPs that we construct use the analytic solution shown in Section 3.1.1. The solutions found earlier were on a general domain for a homogeneous conductivity and an inhomogeneous conductivity with a domain-shaped inclusion. The limitation here is that these OCPs are only optimal for conductivities, γ_{test}, that have a domain-shaped inclusion.

The general idea of the construction is to test the eigenfunctions of the conductivity equation to see if they are eigenfunctions of the Neumann-to-Dirichlet map by checking all the constraints. If they are not eigenfunctions of the Neumann-to-Dirichlet map then we modify them so as to get a proper set of eigenfunctions. Recall, that the Neumann-to-Dirichlet map represents the map between the input current density and resulting voltage measurements each of which must sum to zero. The first constraint is conservation of charge and the second is due to the requirement that voltages must be grounded. These two constraints guarantee uniqueness of the solution. Thus, given our solution of the conductivity equation, we need only check that both the eigenfunctions and output sum to zero.

Recall the solution on the homogeneous domain was found to be

$$u(\eta,\theta) = \frac{1}{\alpha A}\sum_{n=1}^{\infty}\frac{J_n}{n}\eta^{\alpha n}e^{inv(\theta)} \tag{7.1}$$

and the solution for a domain-shaped inclusion was found to be

$$w_2(\eta,\theta) = \sum_{n=1}^{\infty}\left(E_n\eta^{\alpha n} + H_n\eta^{-\alpha n}\right)e^{inv(\theta)}, \tag{7.2}$$

where the constants E_n and H_n are found in Appendix B.2 and the definitions of the other terms are found in Section 3.1.1. Note that w_2 is the solution outside the domain-shaped inclusion. The eigenfunctions of conductivity equation are $\{g_m = e^{inv(\theta)}\}$ for $m = 1, ..., \infty$. These functions do not integrate to zero. If we choose the functions $g_m(\theta) - \beta_m$ where β_m is defined

$$\int_{-\pi}^{\pi} g_m(\theta)d\theta = \beta_m \neq 0,$$
$$\int_{-\pi} g_m(\sigma)d\sigma = \rho_m \neq 0,$$

the constraint is satisfied. Next we need to verify that this resulting set of functions are eigenfunctions of the Neumann-to-Dirichlet map. Using $g_m(\theta) - \beta_m$ in the solutions (7.1) and (7.2), i.e. (3.15), (3.19) from earlier, we have

$$\begin{aligned} w_2(1,\theta; g_m - \beta_m) - u(1,\theta; g_m - \beta_m) &= \sum_{n=1}^{\infty} \frac{\lambda_n}{\|g_n(\theta)\|_p} (g_m - \beta_m, g_n)_p \, g_n, \\ &= \lambda_m g_m(\theta), \end{aligned} \tag{7.3}$$

where λ_m is defined

$$\lambda_m \equiv \frac{\frac{2}{A\alpha m}(\gamma_1 - 1)\eta_1^{\alpha m}}{(1-\gamma_1)\eta_1^{\alpha m} - (1+\gamma_1)\eta_1^{-\alpha m}}. \tag{7.4}$$

We see that (7.3) simplifies by the orthogonality of the eigenfunctions, (3.9). The last requirement for the Neumann-to-Dirichlet map is that the voltages must sum to zero. Therefore when we apply that constraint, (7.3) implies

$$(R_\gamma - R_1)(g_m - \beta_m) = \lambda_m(g_m - \beta_m). \tag{7.5}$$

Thus, the eigenfunctions of the Neumann-to-Dirichlet map are

$$J_m(\theta) \equiv g_m - \beta_m = e^{imv(\theta)} - \beta_m. \tag{7.6}$$

In practice we use the functions

$$T_l^k = \begin{cases} cos(mv(\theta_l)) - \tilde{\beta}_m, & \text{for } m \leq \frac{L}{2}, \\ sin((m - \frac{L}{2})v(\theta_l)) - \tilde{\beta}_m, & \text{for } \frac{L}{2} + 1 \leq m \leq L - 1, \end{cases} \tag{7.7}$$

as the analytic OCPs (AOCPs), where $\theta_l = \frac{2\pi l}{L}$, and $\tilde{\beta}_m$ is defined

$$\tilde{\beta}_m = \begin{cases} \sum_{l=1}^{L} cos(mv(\theta_l)), & \text{for } m \leq \frac{L}{2}, \\ \sum_{l=1}^{L} sin((m - \frac{L}{2})v(\theta_l)), & \text{for } \frac{L}{2} + 1 \leq m \leq L - 1, \end{cases}$$

Next, we will describe the numerical OCPs calculated.

7.2 Numeric OCPs

In this section we focus on numerical ways of finding the OCPs. We assume the FEMCEM simulations give a good approximation for the difference of the Neumann-to-Dirichlet maps. We denote the FEMCEM difference map as

$$\delta\mathbf{L}(\ \cdot\ ; \gamma_{test}, \gamma_0) \approx R_{\gamma_{test}} - R_{\gamma_0}. \tag{7.8}$$

We construct $\delta\mathbf{L}$ from the FEMCEM matrix equation $Ab = f$, (3.33), where $f = \mathcal{C}^T J$, $V = C\beta$, and β is defined in b, i.e. $b = [\alpha\ \beta]^T$. We define a new matrix

$$\tilde{\mathcal{C}} \equiv [\mathbf{0}_{L \times N_n}\ \mathcal{C}]\,. \tag{7.9}$$

Combining all of this we get our FEMCEM difference map given as

$$\delta\mathbf{L}(\ \cdot\ ; \gamma_{test}, \gamma_0) \equiv \left[\tilde{\mathcal{C}} A^{-1}(\gamma_{test}, z)\tilde{\mathcal{C}}^T\ -\ \tilde{\mathcal{C}} A^{-1}(\gamma_0, z)\tilde{\mathcal{C}}^T\right](\cdot), \tag{7.10}$$

where $A(\gamma, z)$ is defined by (3.34) and $\mathcal{C}$ is defined by (3.37). It should be noted that we in general do not compute the inverse of the matrix A because it is computationally expensive.

Due to the fact that the matrix A is ill-conditioned we have used several methods to get the eigenvectors and compare the results. We list the methods below.

1. Apply the power method to (7.8) as in [31], denoted NOCP1.

2. Directly find the eigenvectors of the matrix (7.10) using Matlab's eig command, denoted NOCP2.

3. Find the eigenvectors from the matrix (7.10) without constructing A^{-1} [86], denoted NOCP3.

4. Construction of a mapping $\delta\tilde{\mathbf{L}} \approx R_{\gamma_{test}} - R_{\gamma_0}$ on a basis of CPs, denoted NOCP4.

Each method has apparent advantages and disadvantages. The power method is the most general. If one had a physical experiment, one could apply a current to the tank/person, measure voltages, normalize, and repeat. This is done in practice, for instance at RPI with the ACT3 system. However, we only have simulated data to construct our NOCPs. The limiting factors in the construction of the NOCPs is solely due to the FEM and its accuracy. The matrix A in (7.10) is large, approximately $5,000 \times 5,000$, and ill-conditioned.

The second method is the most computer intensive because it requires constructing the inverse of A. The third method is quick, but is dependent on an initial guess of CPs. The second and third test involve constructing matrices of size $L \times L$ that have rank of $L-1$. As a result these matrices are singular and the corresponding eigenvectors constructed are questionable. The fourth method uses a CP basis in order to get a matrix of size $L-1 \times L-1$ with rank $L-1$. Unfortunately, this method depends on the initial guess and there are no convergence results for the process. We discuss the details of the first and fourth methods below. The third method is straightforward and the details of it are in Appendix B.10.

7.2.1 Power Method

In this section we describe an algorithm using the power method applied to the operator (7.8). The power method was used by Gisser, et al. in 1988 to find OCPs, [31]. Later Breckon and Pidcock in 1988, [12], discussed details of obtaining the whole set of CPs. They noticed that since $R_{\gamma_{test}} - R_{\gamma_0}$ is a symmetric compact operator it has real eigenvalues $|\lambda_1| \geq |\lambda_2| \geq ... \geq 0$ and orthonormal eigenfunctions. Therefore, we should be able to construct a whole set of OCPs with our FEMCEM assuming it is sufficiently accurate. We present below the details of the algorithm.

1. Set $i = 1$ and $\delta\mathbf{L}^{(i)}(\ \cdot\ ; \gamma_{test}, \gamma_0) = \delta\mathbf{L}(\ \cdot\ ; \gamma_{test}, \gamma_0)$,

2. Guess any J^k for $k = 0$ with the constraints that $\|J^k\|_2 = 1$ and $\sum_{l=1}^{L} J_l^k = 0$.

3. Compute $J^{k+1} = \frac{1}{\|\delta\mathbf{L}^{(i)}(J^k; \gamma_{test}, \gamma_0)\|_2} \delta\mathbf{L}^{(i)}(J^k; \gamma_{test}, \gamma_0)$.

4. Compute $\Delta = \|J^{k+1} - J^k\|_2$

   (a) If $\Delta \leq \epsilon$, then set $i = i + 1$, define

   $$\delta\mathbf{L}^{(i+1)}(\ \cdot\ ; \gamma_{test}, \gamma_0) = \delta\mathbf{L}(\ \cdot\ ; \gamma_{test}, \gamma_0) - \sum_{j=1}^{i} \langle \delta\mathbf{L}^{(1)}, \hat{J}^j \rangle \hat{J}^j$$

   where $\hat{J}^i = J^{k+1}$, $\lambda_i = \|\delta\mathbf{L}^{(i)}(J^k; \gamma_{test}, \gamma_0)\|_2$ and go to step 2.

   (b) Otherwise, set $k = k + 1$ and go to step 3.

5. If $i > L - 1$ then stop the procedure.

7.2.2 Construction of NOCP4

In this section we approximate the operator R_γ in a way similar to the calculation of the scattering transform in Section 5. An explicit formula of the approximate operator is given as

$$\delta\tilde{\mathbf{L}}(m,n) = (J_m, \delta\mathbf{L}(J_n; \gamma_{test}, \gamma_0))_L \,, \text{ for } m,n = 1...L-1 \qquad (7.11)$$

where $(\ ,\ )_L$ is the inner product over the vectors of length L. This matrix $\delta\tilde{\mathbf{L}}$ is of size $L-1 \times L-1$ and has a basis of the CPs, $\{J_n\}$ for $n = 1...L-1$. Therefore to get the OCPs we find the eigenvectors of this operator and then express these eigenvectors with respect to the basis of currents. The algorithm proceeds as follows:

1. Pick a set of L-1 CPs, J, that each sum to zero.

2. Construct $(J_m, \delta\mathbf{L}(J_n; \gamma_{test}, \gamma_0))_L$, for $m,n = 1...L-1$.

3. Find the eigenvectors of $\delta\tilde{\mathbf{L}}$, denoted as W.

4. Evaluate
$$J_{new}(\theta_l, k) = \sum_{n=1}^{L-1} W(n,k) J(\theta_l, n).$$

5. If $\|J - J_{new}\| < \epsilon$, stop. Otherwise, set $J = J_{new}$ and go to *Step 2.*

The initial guess of this method is very important. It does not guarantee convergence to the correct eigenvectors, as seen in numerical experiments. Therefore, we specify three types of these CPs, NOCP4a is when we use a random guess, NOCP4b is when we use a guess of NOCP3, and NOCP4c uses the guess of TCPs.

7.3 Verification of the NOCPs

We want to verify the computation of the eigenvectors with the CEM and FEM techniques. We test our method with the optimal CPs resulting from a simulated circular tank with a circular inclusion. If the optimal CPs are obtained successfully we should have exactly the TCPs [35]. The simulated tank has a perimeter of 900mm with a circular inclusion of 10%, 20%, 30%, 40%, 50%, 60% 70%, 80%, 90%, or 95% of the tank's radius. The tank has a conductivity 1 outside the inclusion and 2 inside the inclusion. The parameter z was chosen to be 2.4 in these simulations.

We can see the mean relative percent errors for the different CPs and all the inclusions in Figure 7.1. The error term is computed by the following formula

$$RE = \frac{1}{L-1} \sum_{k=1}^{L-1} \frac{\|T^k - T^k_{ideal}\|_2}{\|T^k_{ideal}\|_2} \times 100,$$

where T^k are the recovered CPs each of size $L \times 1$ and T^k_{ideal} are the TCPs. It is apparent that with an inclusion of less than 40% not all the CPs can be recovered accurately. For instance, the matrix $\hat{R}^M_\gamma$ from NOCP4a, NOCP4b, or NOCP4c does not reach full rank until 40%. We find that the best method appears to be the power method, NOCP1, for inclusions of size 50% or larger. We discount NOCP4c because it is unrealistic to guess the answer. It could be argued that NOCP4b is the best, but the difference seems rather minimal. Another observation is that the fourth method does not have good convergence. This can be seen in Figure 7.1 by observing that the minimum error of NOCP4a is greater than 40% and noting that the initial guess of NOCP4a was far away from the ideal CPs.

Figure 7.2 contains a plot of the relative percent errors, with respect to L^2, of NOCP1 for each particular CP for inclusions of size 20%, 40%,

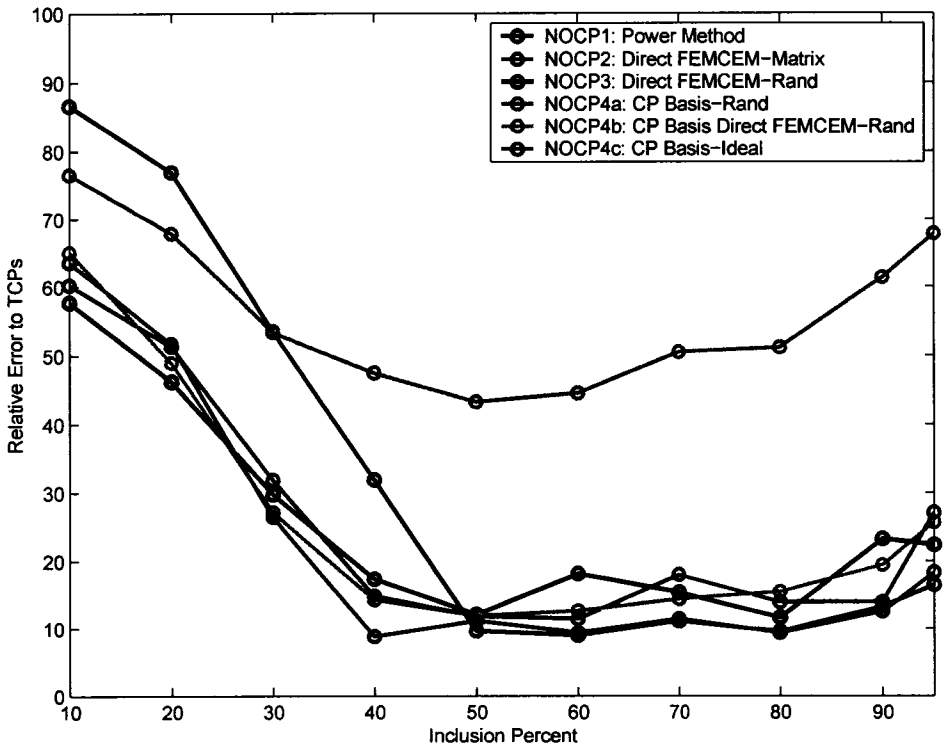

Figure 7.1: Mean relative percent errors, with respect to L^2, over all CPs of NOCPs for a circle with a circular inclusion.

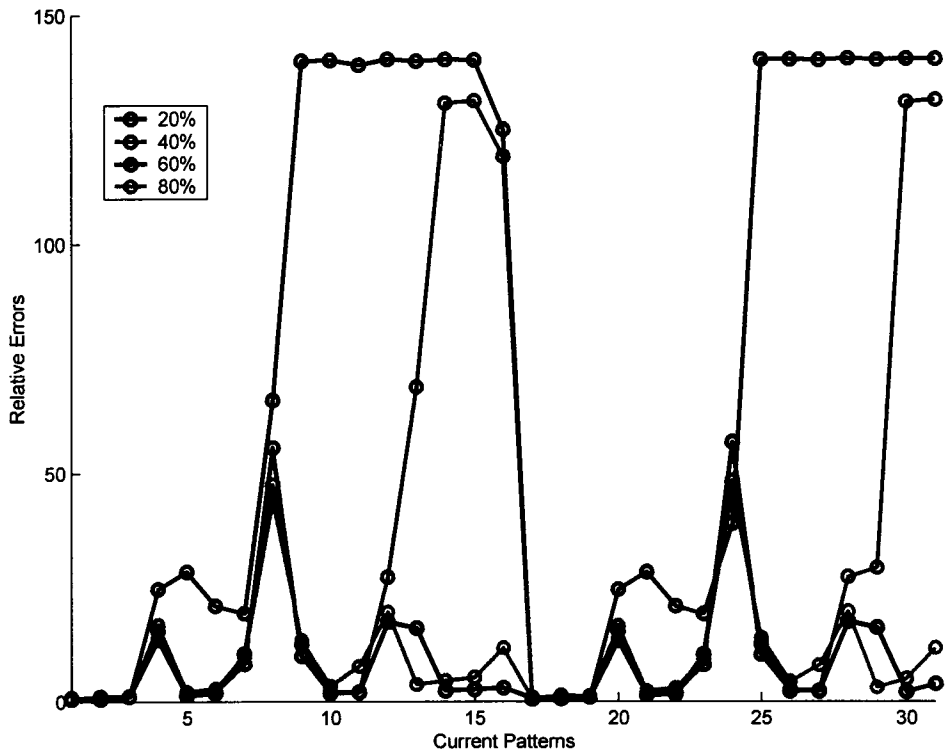

Figure 7.2: Relative percent errors, with respect to L^2, between NOCP1s and 'ideal' TCPs found on a circle with a circular inclusion of 20%, 40%, 60%, and 80%.

60%, and 80%. Although, the mean relative error is very large for 20% and 40% we see that the method is able to pick up the low frequency optimal CPs. It is apparent that the higher frequency CPs can only be found in the case of a very large inclusion. We expect this because the higher frequency patterns do not penetrate as far into the domain as the lower frequency ones.

As a final illustration for verification, we show the first 16 CPs from NOCP1 with an inclusion of 80% plotted over the TCPs. This is to show that these NOCP1s appear to be good, despite the somewhat large relative errors. The error is most likely due to domain modeling in the FEM and/or the use of the CEM. The circular domain and inclusion are approximated

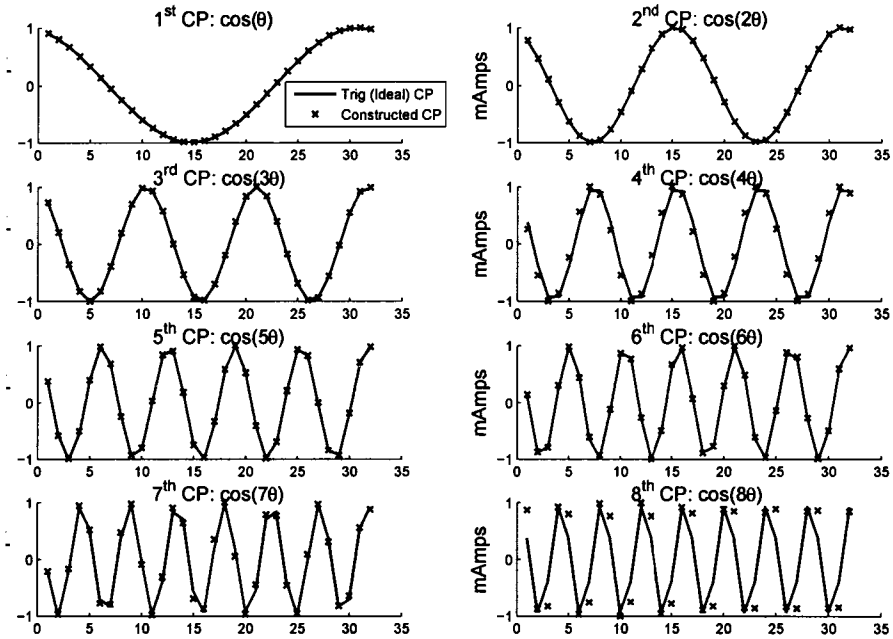

Figure 7.3: Comparison between first eight CPs of NOCP1 and 'ideal' TCPs found on a circle with a circular inclusion of 80%.

by polygons of many sides, but not exactly circles. The optimal CPs, TCPs, that were derived for the unit circle assumed a continuous electrode model and we use the CEM.

7.4 Analysis of AOCPs

In this section we do some investigation into the difference between AOCPs and TCPs. The AOCPs are given by (7.7) and shown again below

$$T_l^k = \begin{cases} cos(mv(\theta_l)) - \tilde{\beta}_m, & \text{for } m \leq \frac{L}{2}, \\ sin((m - \frac{L}{2})v(\theta_l)) - \tilde{\beta}_m, & \text{for } \frac{L}{2} + 1 \leq m \leq L - 1, \end{cases}$$

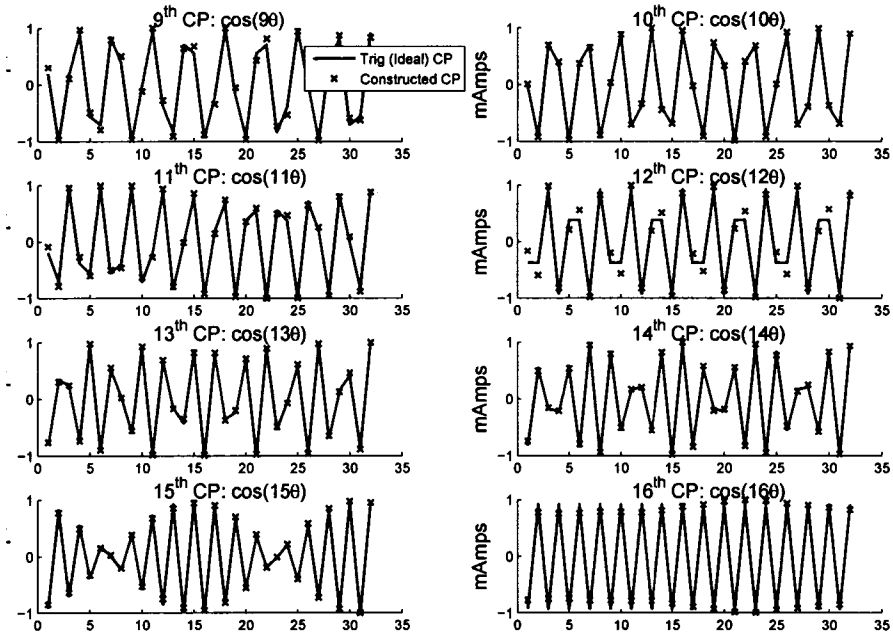

Figure 7.4: Comparison between 9^{th} through 16^{th} CPs of NOCP1 and 'ideal' TCPs found on a circle with a circular inclusion of 80%.

where v, α, and p are defined by (3.10), (3.12), and (3.5), respectively, and displayed below

$$v(\theta) = \alpha \int_{\theta_0}^{\theta} p(\theta) d\theta, \qquad \alpha \equiv 2\pi \left(\int_{-\pi}^{\pi} p(s) ds \right)^{-1},$$

$$p(\theta) = \frac{\sqrt{(r')^2 + r^2}}{r}.$$

It is clear that if $r(\theta) = 1$ then $p(\theta) = 1$, $\alpha = 1$, and, assuming $\theta_0 = 0$, then $v(\theta) = \theta$. That is, we would have exactly the TCPs which are optimal on a circular domain with a circular inclusion. It is of interest to consider how far $v(\theta)$ is from θ in practice and, in the case that it is close, whether any conclusions can be drawn from this. We define a useful parameter, ϵ, as follows

$$\epsilon \equiv \max_{\theta} \left| \alpha \int_0^{\theta} p(s) ds - \theta \right| = \max_{\theta} |v(\theta) - \theta| . \tag{7.12}$$

7.4.1 Experimental evaluation of ϵ

We consider the domains of an ellipse and a chest shown in Figure 7.5. The plots of $p(\theta)$ for each domain are shown in Figure 7.6. The horizontal line at 1 represents $p(\theta)$ for a circle. We see that the functions, $p(\theta)$, for the ellipse and chest are relatively close to 1. The next illustration is of $|v(\theta) - \theta|$ for the ellipse and chest seen in Figure 7.7. We find the values $\epsilon_{ellipse} \approx 0.0101$ and $\epsilon_{chest} \approx 0.0561$. It appears that given the small values of the ϵ's an analysis comparing CPs is practical.

7.4.2 Difference between TCPs and AOCPs

We want to get an approximate difference between the TCPs and AOCPs. From the previous section we found numerically that ϵ was small, see (7.12) and the right side of Figure 7.6. Thus we can practically assume

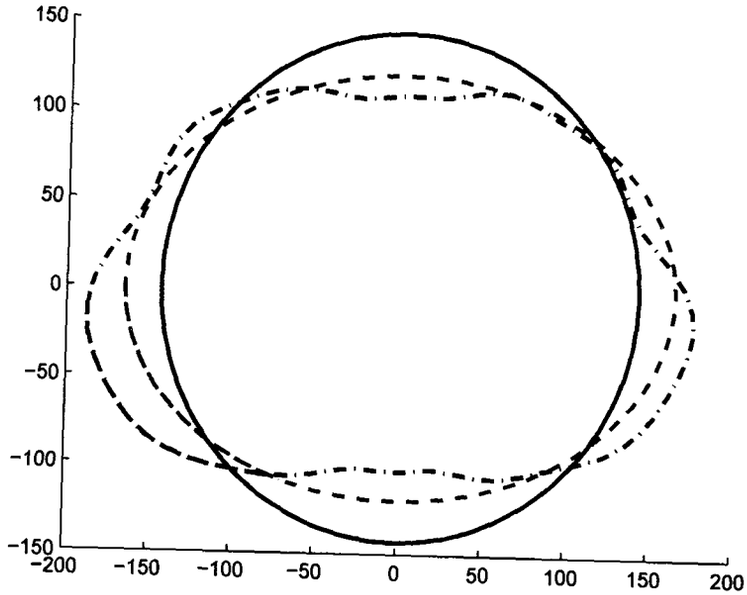

Figure 7.5: Comparison of the circle, ellipse, and chest domains.

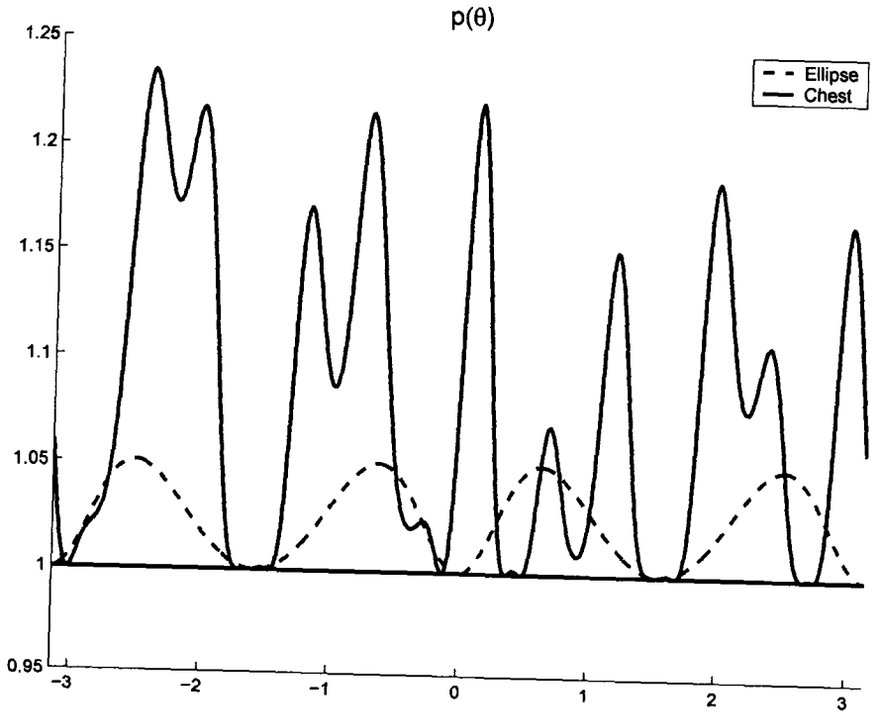

Figure 7.6: Illustrations of the $p(\theta)$ for an ellipse and chest-shaped domain.

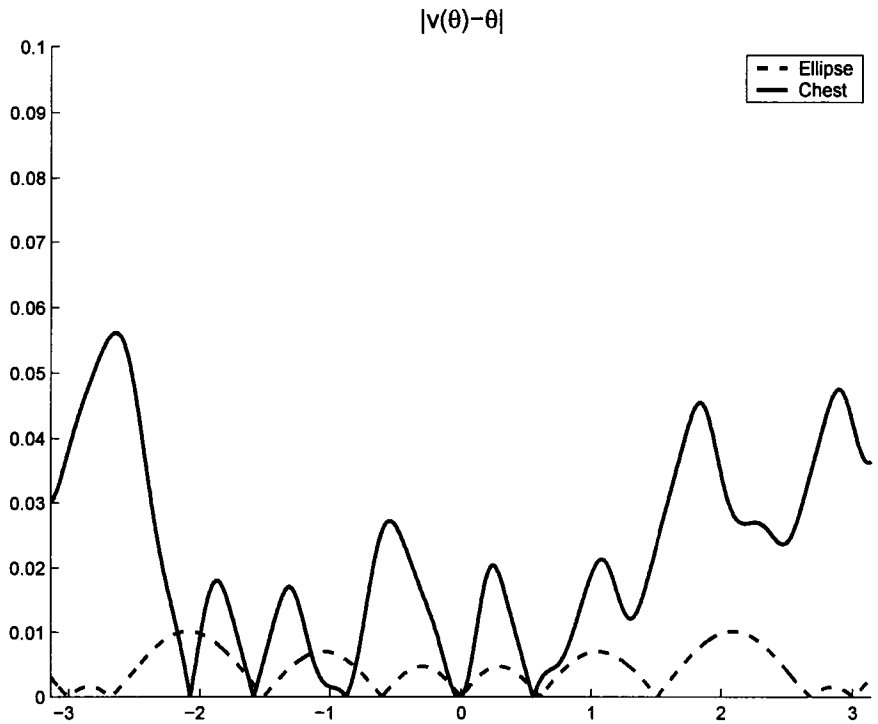

Figure 7.7: Illustrations of $|v(\theta)-\theta|$ for an ellipse and chest-shaped domain.

that $v(\theta) \approx \theta \pm \epsilon$ and we can approximate the AOCPs in the following way

$$T^k(\theta) = \begin{cases} cos(m(\theta \pm \epsilon)) - \tilde{\beta}_m, & \text{for } m \leq \frac{L}{2}, \\ sin((m - \frac{L}{2})(\theta \pm \epsilon)) - \tilde{\beta}_m, & otherwise. \end{cases}$$

Consider the difference between the cosine terms. We have

$$\begin{aligned} |cos(n(\theta \pm \epsilon)) - cos(n\theta)| &= |cos(n\theta)cos(n\epsilon) \mp sin(n\theta)sin(n\epsilon) - cos(n\theta)| \\ &\leq n\epsilon|sin(n\theta)| + \tfrac{(n\epsilon)^2}{2}|cos(n\theta)| + \tfrac{(n\epsilon)^3}{3}, \end{aligned}$$

and

$$|sin(n(\theta \pm \epsilon) - sin(n\theta)| \leq n\epsilon|cos(n\theta)| + \frac{(n\epsilon)^2}{2}|sin(n\theta)| + \frac{(n\epsilon)^3}{3},$$

assuming that $\epsilon << 1$. The bounds are calculated using Taylor's series and Taylor's inequality.

In a practical sense we can conclude the difference between AOCPs and TCPs is approximated by

$$\|cos(nv(\theta)) - \tilde{\beta}_m - cos(n\theta)\|_\infty \approx n\epsilon + \frac{(n\epsilon)^2}{2} + \frac{(n\epsilon)^3}{3} + |\tilde{\beta}_m|.$$

The first few CPs give the most information of the conductivity. If we calculate this estimated difference for the first three CPs for the chest we get 0.062, 0.121, and 0.193. Assuming the current amplitude is 1mA, clearly the difference gets quite large as n gets large. However, the real question is what does this difference do to the reconstructions? How much better are the reconstructions? As a first attempt to answer this question, we do a short investigation into the difference in distinguishabilities between AOCPs and TCPs below.

7.4.3 Difference in Distinguishabilities

Consider the approximate difference in the distinguishability of the AOCPs and the TCPs. If the difference in distinguishabilities is large, it is expected that AOCPs should work much better than TCPs. We get the distinguishability from (7.3) for AOCPs and the following

$$\begin{aligned} \delta_n^{(AOCP)} &= \frac{\|V(\gamma;cos(nv(\theta))) - V(1;cos(nv(\theta)))\|_2}{\|cos(nv(\theta))\|_2} \\ &= \frac{\|\lambda_n^{(1)} cos(nv(\theta))\|_2}{\|cos(nv(\theta))\|_2} \\ &= \lambda_n^{(1)}, \end{aligned} \tag{7.13}$$

The conductivity, γ, is assumed to be a conductivity that has a domain-shaped inclusion. Assuming ϵ is small we approximate the TCPs by

$$\begin{aligned} cos(n\theta) &\approx cos(nv(\theta) \pm \epsilon) \\ &\approx cos(nv(\theta)) \pm n\epsilon sin(nv(\theta)) + \tfrac{(n\epsilon)^2}{2} cos(nv(\theta)) + \tfrac{(n\epsilon)^3}{3}. \end{aligned} \tag{7.14}$$

Therefore, if we approximately calculate the distinguishability from (7.14) for the TCPs we have

$$\delta_n^{(TCP)} \approx \lambda_n^{(1)} \pm n\epsilon\lambda_n^{(2)} + \frac{(n\epsilon)^2}{2}\lambda_n^{(1)}. \tag{7.15}$$

The relative difference in the distinguishabilities is approximated by

$$\frac{|\delta_n^{(TCP)} - \delta_n^{(AOCP)}|}{\delta_n^{(AOCP)}} \approx \frac{n\epsilon|\lambda_n^{(2)}| + \frac{(n\epsilon)^2}{2}|\lambda^{(1)}|_n}{|\lambda_n^{(1)}|} \approx n\epsilon + \frac{(n\epsilon)^2}{2}. \tag{7.16}$$

We will look again at the first few CPs to find the distinguishabilities. Numerically, we get the approximate relative percent differences 5.8%, 11.9%, and 18.3% for the first three CPs. This seems to be good evidence that the reconstructions for the AOCPs should be much better than TCPs. We look into numerical verification of these conclusions in terms of actual calculations of distinguishabilities for the CPs and reconstructions on a chest-shaped domain with a chest-shaped inclusion in the following chapter. In addition, we show reconstructions of realistic domains, i.e. inclusions of heart, lungs etc. These reconstructions should illustrate whether AOCPs are better than TCPs in practice.

Chapter 8

CURRENT PATTERN STUDY

In this chapter we test the effectiveness of the all CPs that have been introduced by using simulated voltages from a chest-shaped domain. The experiments are as follows:

- comparison of distinguishabilities resulting from the CPs,
- investigation into skip CPs effectiveness,
- reconstructions on a simulated chest with simulated heart and lungs using scaled conductivity values for all CPs,
- discussion on the choice of γ_{test} in NOCP1 construction.

In all the experiments we simulate a chest cross-section with L = 32 electrodes and a perimeter of 900mm, seen in Figure 8.1. The 900mm was the measured perimeter for the person's chest from [38], and can be considered a typical chest perimeter. The electrodes are of two different sizes. CPs that inject current on all electrodes simultaneously (TCP, OCPs, and OHCPs) are best with wide electrodes. Therefore, for these CPs we choose electrodes of size $25.4mm \times 25.4mm$, which result in small gaps between electrodes. The alternative is CPs that inject current on two electrodes at

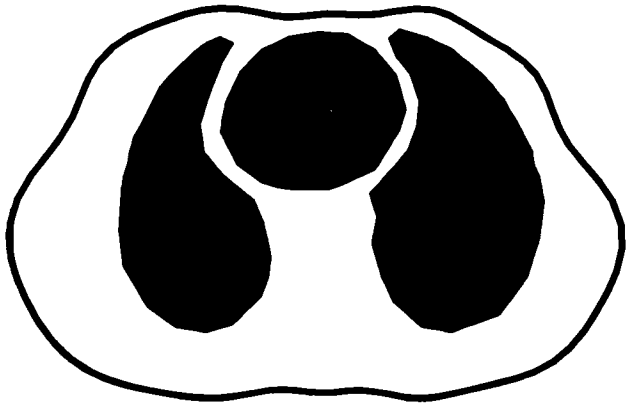

Figure 8.1: Simulated chest domain used in the tests.

once (ACP and skip CPs). These should have narrow and tall electrodes and are chosen to be of size $35mm \times 10mm$.

We let the current amplitude be $M = 1mA$ for all the simulated data. In the first three experiments we use scaled conductivity values. We set the background,γ_0, to 1. The lungs have a conductivity, γ_{lung}, of $\frac{1}{3}$. The heart has a conductivity, γ_{heart}, of 2.

All of these experiments are designed to evaluate the effectiveness of the CPs and to give us insight into performing static reconstructions on a human chest.

8.1 Comparison of distinguishabilities

In Chapter 7 we defined the concept of distinguishability. In this section, we use the distinguishability parameter to evaluate how well the CPs can recognize something in the domain. We divide this study into two

sections: one with chest-shaped inclusions and the other with a heart and lungs in the domain. We begin with the chest-shaped inclusion.

8.1.1 Comparing TCPs versus AOCPs

In the previous chapter we concluded by making an estimate on the approximate difference between AOCPs and TCPs. We found the estimate to be (7.16), i.e.

$$\frac{|\delta_n^{(TCP)} - \delta_n^{(AOCP)}|}{\delta_n^{(AOCP)}} \approx \frac{n\epsilon|\lambda_n^{(2)}| + \frac{(n\epsilon)^2}{2}|\lambda^{(1)}|_n}{|\lambda_n^{(1)}|} \approx n\epsilon + \frac{(n\epsilon)^2}{2},$$

assuming that the conductivity had a domain-shaped inclusion. We simulate voltages for the TCPs and AOCPs on the simulated chest with an inclusion of 80% the chest radius. In Figure 8.2 we see the calculated relative percent difference of TCPs and AOCPs for all the CPs. However when we simply look at the distinguishabilities side by side they look almost identical. This can be seen in Figure 8.3. After careful inspection of the of Figure 8.3 we see that there is a difference between AOCPs and TCPs. However the difference is only noticeable at higher frequencies. We believe these tests can be viewed in two ways. Either it is a failure of the AOCPs to produce better results, or else it is a justification that TCPs are robust enough to be used on a wide variety of boundary shapes.

8.1.2 Heart and lungs

We present the average and maximum distinguishability, shown in Table 8.1.2, for each set of CPs for the simulated chest with heart and lungs. That is, γ_{test} corresponds to a simulated chest with a heart and lungs and γ_0 is the homogeneous domain. We also display the distinguishabilities corresponding to each CP for each set of CPs in Figure 8.4. We see in Figure

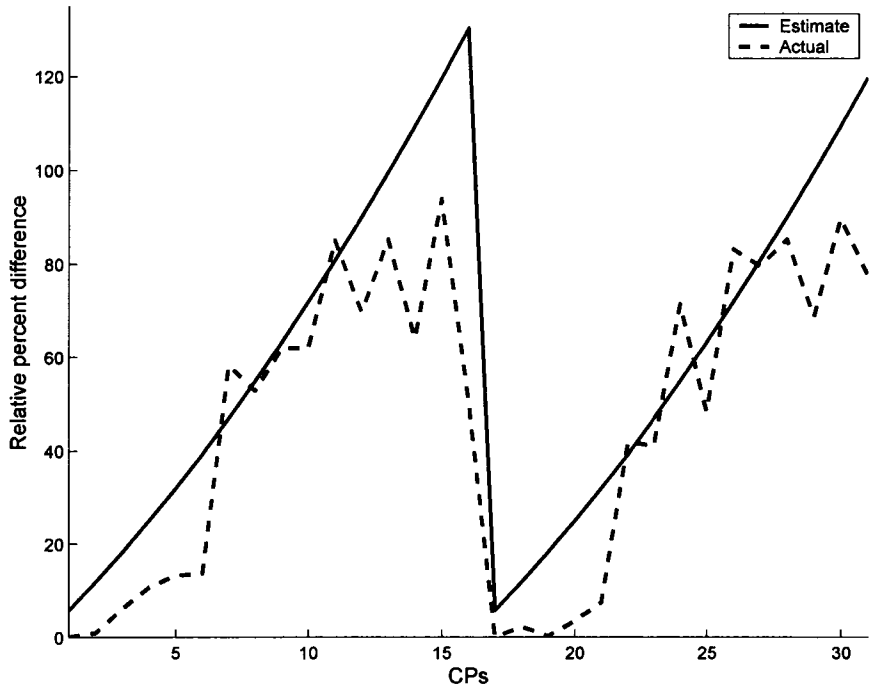

Figure 8.2: Relative percent difference between TCPs and AOCPs for a chest with a 80% chest-inclusion.

Table 8.1.2: Average and maximum distinguishabilities, δ for the simulated heart and lungs.

CP:	Average δ	Maximum δ
Adjacent	4.12	9.47
Skip 3	8.92	19.00
Trig.	9.70	97.84
AOCP	10.15	97.81
NOCP1	7.58	100.81
NOCP3	7.58	100.81
NOCP4b	7.58	100.81
OHCP	18.78	40.62

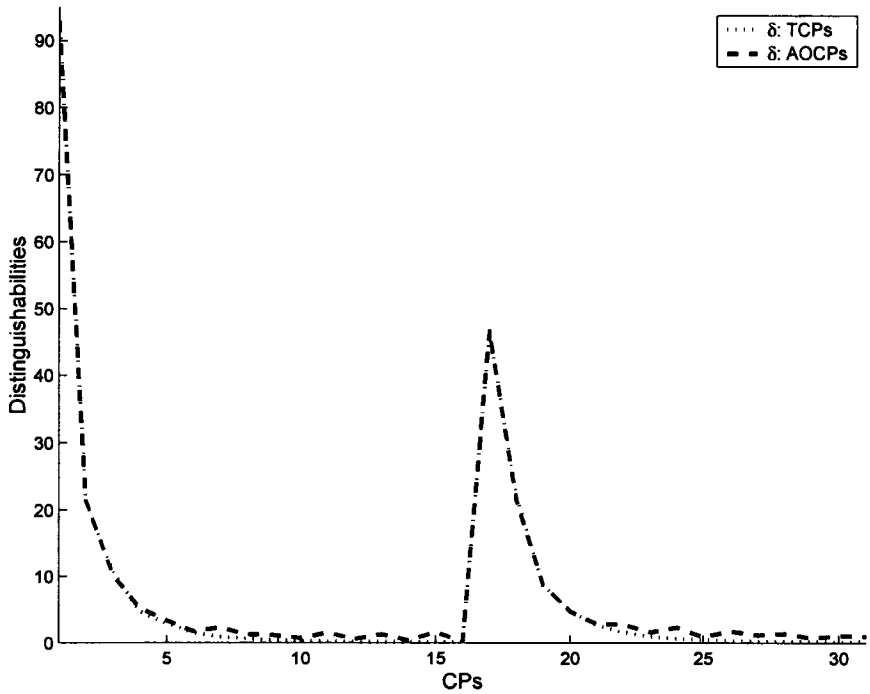

Figure 8.3: Absolute difference of distinguishabilities for an 80% chest-shaped inclusion between TCPs and AOCPs.

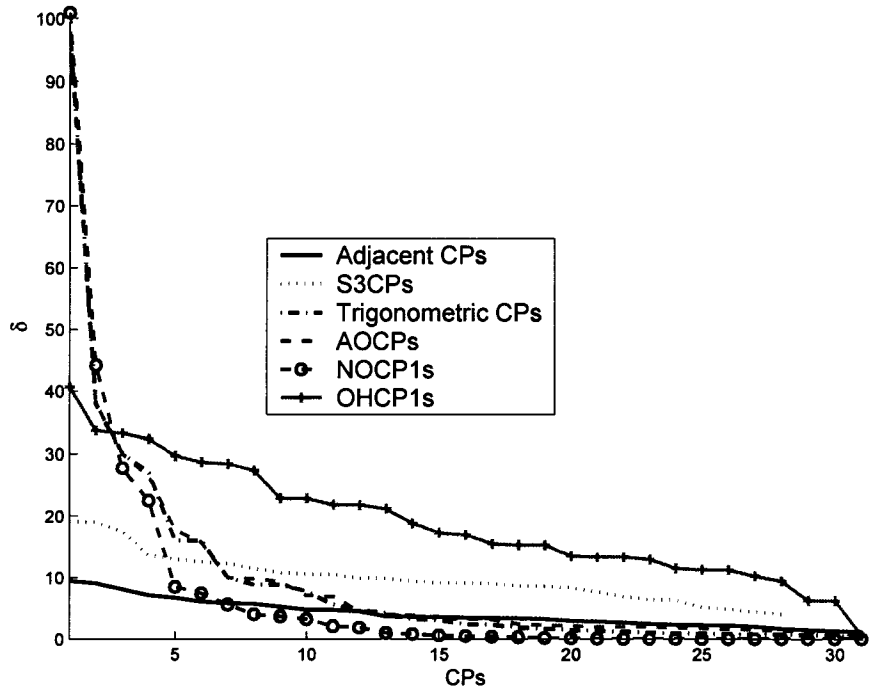

Figure 8.4: Distinguishabilities for each CP of the different CP types sorted.

8.4 that the maxima of TCP, AOCP, and NOCPs are much higher than the ACP, S3CPs, OHCPs. The average of all the CPs are relatively close as seen in Table 8.1.2, except for OHCP. It appears that the 'best' is either AOCP or OHCPs. In Figure 8.4 an interesting aspect to note is the decay in the distinguishabilities. AOCPs, S3CPs and OHCPs do not decay substantially. In contrast TCPs, AOCPs, and NOCP1s seem to decay exponentially. The exponential decay for AOCPs was expected because of its eigenvalues (7.4). NOCP1s probably decay the fastest due to the limits of numerical accuracy. These results are a little hard to judge, because we have no idea of what quality of reconstructions correspond to these distinguishability values. Next we illustrate some reconstructions with these CPs in an effort to draw conclusions about which distinguishabilities are preferred or which distinguishabilities can be accurate judges of performance.

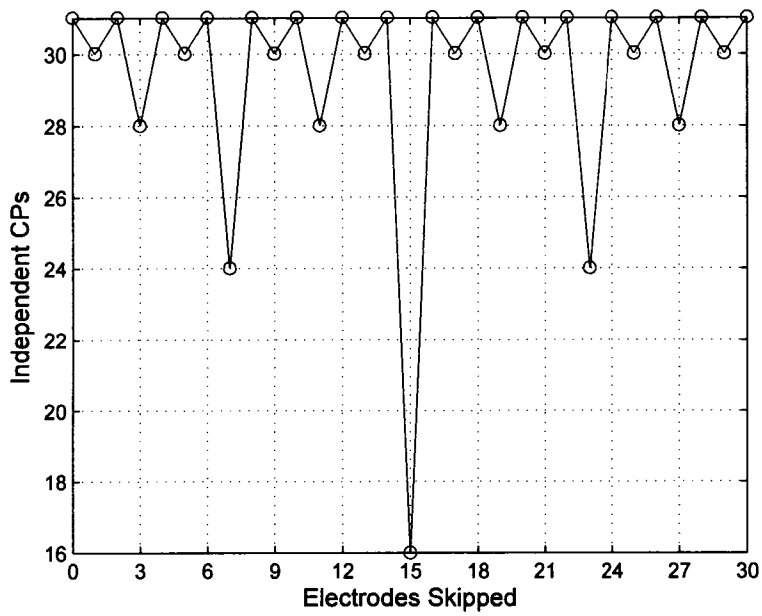

Figure 8.5: Illustration of the number of independent CPs as a function of the number of electrodes skipped for a 32 electrode setup.

8.2 Adjacent CP Reconstructions

The adjacent current patterns (ACPs) are commonly used in studies. In addition to just ACPs there are the skip CPs. The number of independent CPs is dependent on the number of electrodes skipped. We plot the number of independent CPs for all the skip CPs in Figure 8.5. We see ACPs have L-1 along with SsCP when s is even. We expect S3CP, s7CP, and S11CP, and S15CP to not perform as well because of the reduced number of independent CPs. We will restrict our study of skip CPs to S1CP through S15CP. After that point it is equivalent to skipping electrodes in the other direction. Thus we expect mirrored results.

In order to determine the quality of all the different CPs we first look at the distinguishabilities from each of CPs. In Figure 8.6, as expected, the

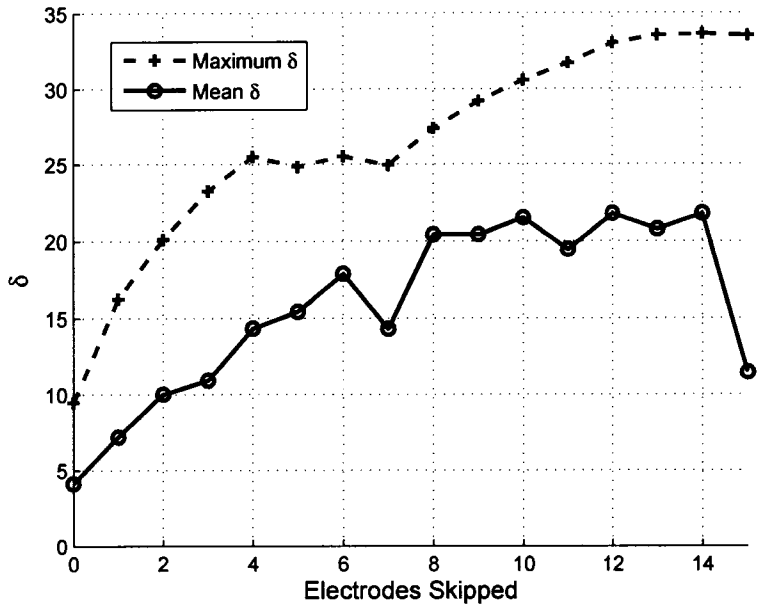

Figure 8.6: Maximum and mean distinguishabilities for ACP, S1CP, through S16CP.

distinguishabilities increase as the number of electrodes increase. There is a drop off in the mean values after more than 9 electrodes are skipped.

In Figure 8.7 there is an illustration of reconstructions of the heart and lung scenario, described above, for ACPs, skip 1 through 7 CPs. The remainder are in Figure 8.8. It appears that as long as there are L-4 or more independent CPs the reconstructions work well. Clearly in the cases of S7CP and S15CP, 24 and 16 independent CPs, there is not enough information to construct an accurate Neumann-to-Dirichlet map. It seems surprising that there is not a noticeable improvement in the reconstructions considering how the distinguishabilities increase in Figure 8.6 with the more electrodes skipped.

8.3 Reconstructions from a simulated chest with heart and lungs

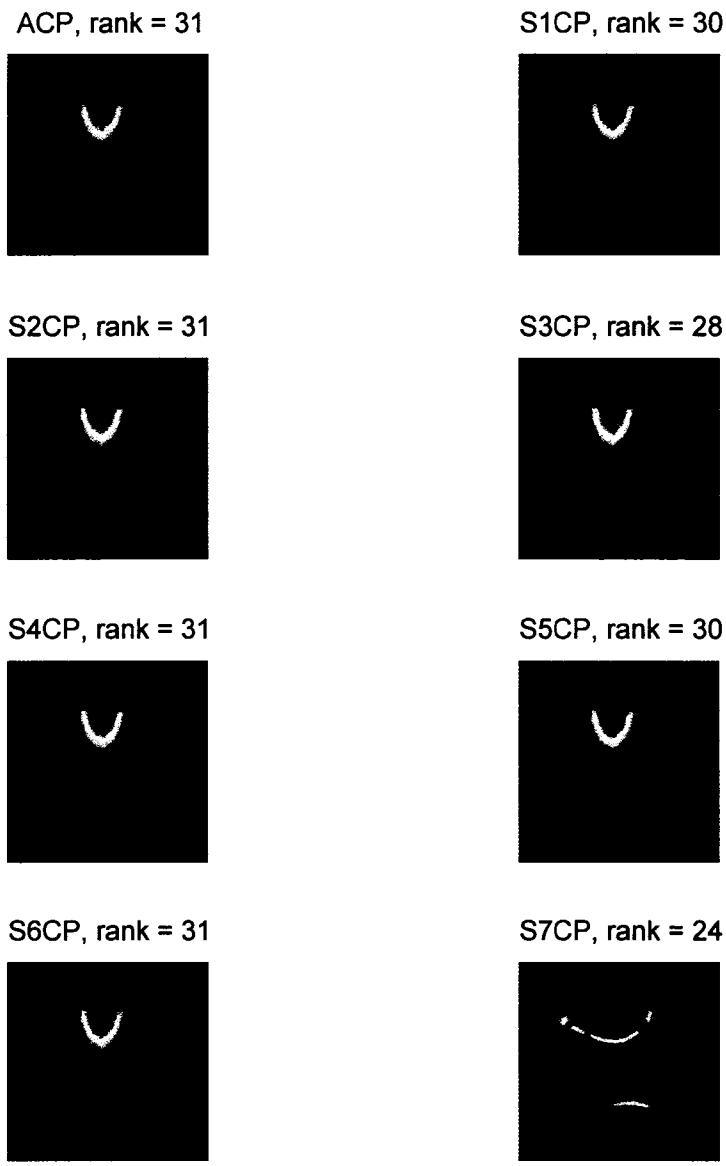

Figure 8.7: Reconstructions of simulated heart and lungs for the ACPs and S1CP through S7CPs. The truncation radii used is 2.

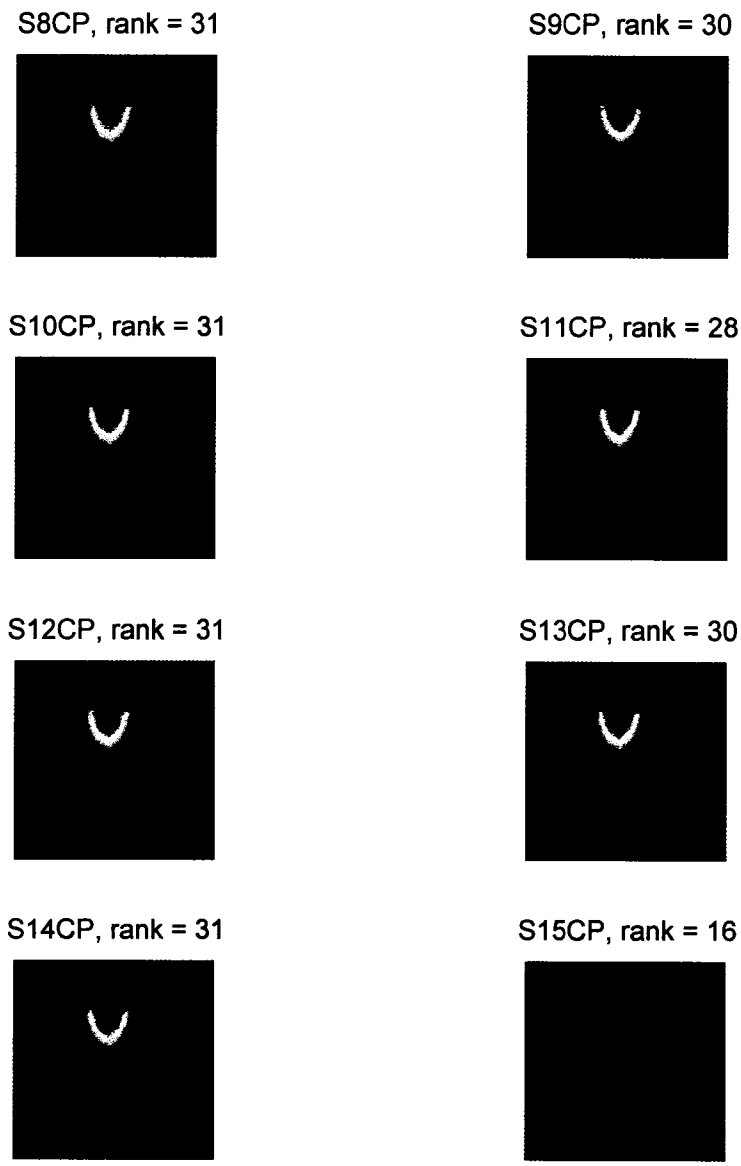

Figure 8.8: Reconstructions of simulated heart and lungs for the S8CP through S15CP. The truncation radii used is 2.

Table 8.3: Errors in reconstructions for different CPs. Note the abbreviations H - heart, Ls - lungs, and RE - relative error.

CP	Max H	Max H RE	Min Ls	Min Ls RE
ACP	1.80	10.0%	0.20	40%
S3CP	1.75	12.5%	0.19	43%
TCP	1.94	3.0%	0.20	40%
dTCP	1.96	2.0%	0.31	10%
AOCP	1.92	4.0%	0.27	19%
dAOCP	2.03	4.0%	0.27	19%
NOCP1	1.97	1.5%	0.30	10%
OHCP	1.99	0.5%	0.31	7%

In this section we present the results of reconstructions for the simulated chest-shaped domain with heart and lungs. In Figure 8.9 we see these results. Spatially, the locations are best found with dTCPs, dAOCPs, and NOCP1s. The best clarity is found with NOCP1s. We present the truncation radii, maximum, and minimum from each reconstruction in Table 8.3. The maximum and minimum are taken to be the heart and lung conductivity, respectively. We find the relative errors with respect to these values. Recall that the conductivity of the heart is 2 and that of the lungs is 1/3. ACP and S3CPs have the largest relative errors. TCPs are not much better than the alternating CPs. The dTCPs, dAOCPs, NOCP1, and OHCP1s all seem to get good values. We see that OHCPs recover the values the best. It should be noted that dAOCPs are constructed similar to dTCPs and a discussion on their construction is presented in Section 6.2.3.

It seems quite clear that we can conclude that the CPs with the highest distinguishabilities obtain the best spatial resolution, i.e. dTCP, dAOCP, and NOCP1. It appears from OHCPs that a high average distinguishability results in good conductivity values. The skip patterns seem to do worse than their distinguishability would imply. One possible explanation for the poor

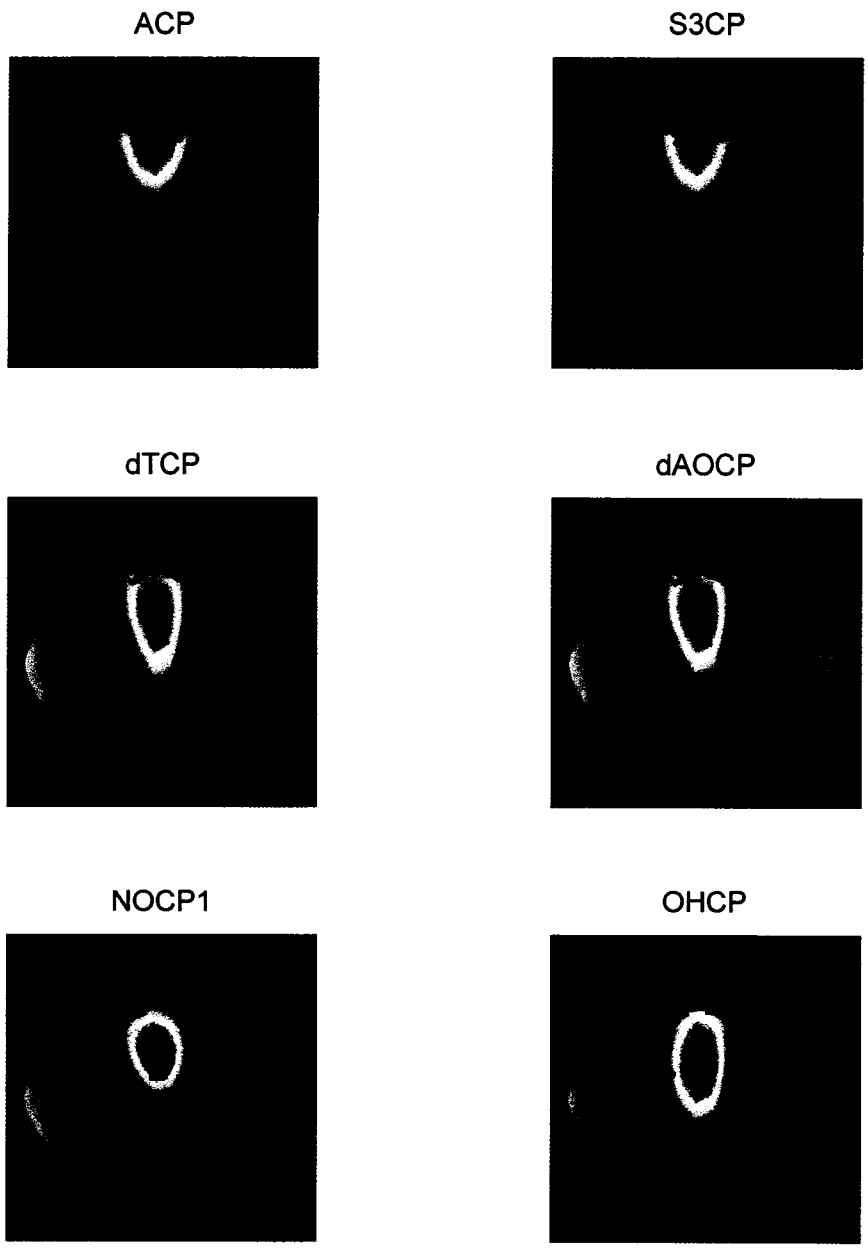

Figure 8.9: Reconstructions on a realistic chest with heart and lungs with for each set of CPs.

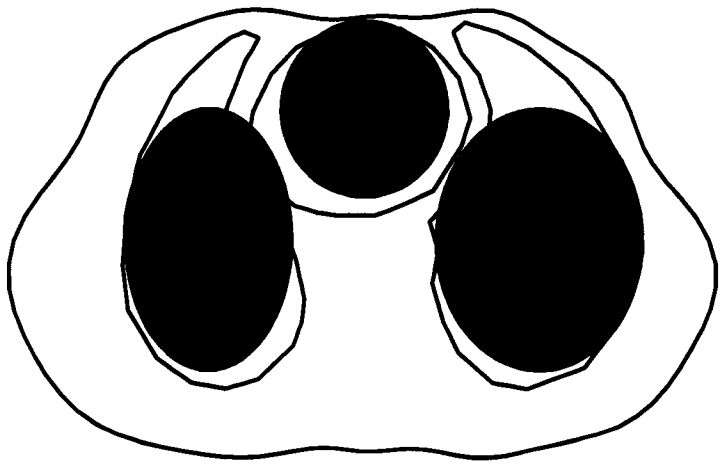

Figure 8.10: Elliptical organs approximating the realistic organs.

quality of reconstruction using ACP and S3CP is the tall, thin electrodes that are used for these CPs.

8.4 Testing γ_{test} in NOCP1 construction

Thus far we have assumed ideal knowledge of the conductivity in the domain when constructing the NOCPs. In this section we give a more practical construction of the NOCP1s. We assume that we want to construct a chest with heart and lungs in the domain, but since we would not know the shape of the organs we assume elliptical shapes. These CPs will be denoted as $NOCP1_{ell}$ and the ideal knowledge will be denoted $NOCP1_{ideal}$. The approximate organs are shown in Figure 8.10 on top of the realistic organs. There are two questions here: how different are the resulting NOCP1, and how much worse/better are the reconstructions? The best way to calculate the differences in the two sets of CPs constructed is to look at the distinguishabilities. In Figure 8.11 we see an illustration comparing the two sets of distinguishabilities from voltages on a simulated chest with realistic organs. Its hard to see from the picture, but the $NOCP1_{ideal}$ have a slightly

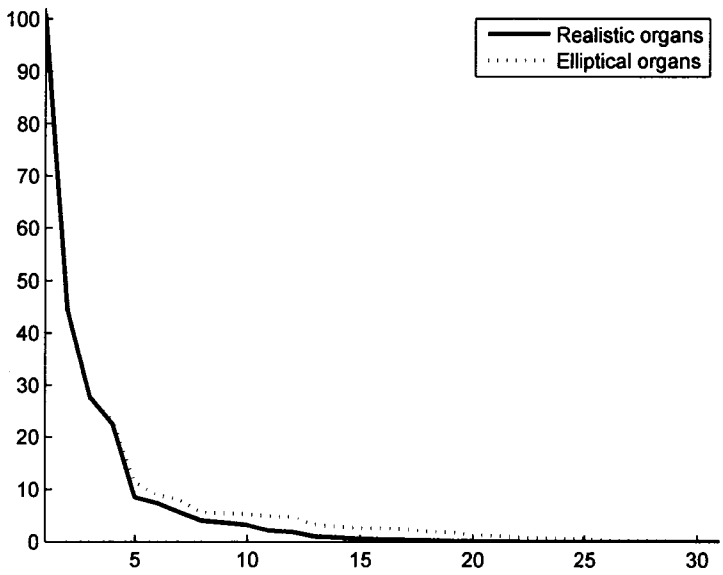

Figure 8.11: Distinguishabilities of $NOCP1_{ideal}$ and $NOCP1_{ell}$.

higher distinguishability for the first CP (100.8 compared to 99.5), although the average distinguishability is slightly higher using the $NOCP1_{ell}$ (8.7 compared to 7.6). It can be seen on the tail end of Figure 8.11 that the $NOCP1_{ell}$ are slightly higher.

In Figure 8.12 we see reconstructions using both sets of NOCP1s on a chest with realistic heart and lungs. Both CPs work well. Specifically, the the heart values found were 1.97 and 1.82 and the lungs were 0.30 and 0.30 for the $NOCP1_{ideal}$ and $NOCP1_{ell}$, respectively. It is impossible for us to test, without a lab, to see if NOCP1s constructed using elliptical organs are practical. However, in our simple tests they are very practical and very close to ideal knowledge of the conductivity in the domain. In the remainder of this dissertation we use NOCP1s constructed from ideal knowledge of the conductivity.

Figure 8.12: Reconstructions of a chest with realistic heart and lungs using $NOCP1_{ideal}$ on the left and $NOCP1_{ell}$ on the right.

Chapter 9

MODELING ASSUMPTIONS & ERRORS

Thus far there have been reconstructions from measured data in Section 6.1 on an elliptical tank and in Section 6.3 from a human subject. The results from the tank were good and had occasional artifacts. The human subject reconstructions were very sensitive to the domain in which t^{exp} was modeled. As a result of these reconstructions this chapter investigates the possible reasons for the artifacts/errors observed earlier. A series of different assumptions are applied to the method or errors are applied to simulated data. Almost all of data is constructed with the FEMCEM discussed in Chapter 3.

The same scenario as in Sections 8.1-8.3 is used for most testing in this chapter. That is, a simulated chest, perimeter of 900mm, with a simulated heart and lungs in the domain. The conductivity of the heart is 2, lungs are 1/3, and the background is set to 1. The electrodes are of size $25.4mm \times 25.4mm$ for dTCPs, NOCP1s, and OHCPs and size $35mm \times 10mm$ for ACPs and S3CPs. Lastly, the injected current has a maximum amplitude 1mA. The experiments that were performed are listed below.

1. An investigation into the effect of FEMCEM over the analytic voltages.

2. Errors in conductivity reconstruction of the chest-shaped domain caused by domain modeling.

3. Investigation into t_{diff}^{exp}, i.e. difference images.

4. Electrode placement error, rotation of electrodes by 1%-4%, in inhomogeneous voltage measurements.

5. Noise applied to the inhomogeneous voltages within $\pm 0.01mV$, $\pm 0.1mV$, $\pm 0.5mV$, and $\pm 1mV$.

6. Noise applied to the inhomogeneous currents within $\pm 0.001mAmps$, $\pm 0.005mAmps$, $\pm 0.01mAmps$, and $\pm 0.02mAmps$.

9.1 FEMCEM versus Analytic voltages

In this section we compare the use of simulated homogeneous voltages constructed using FEMCEM versus the analytic solution. We use measured voltages from RPI using their ACT3 system. It is a circular tank of radius 15cm, electrodes of size 1.6cm high by 2.5cm wide, and 32 electrodes. TCPs are used with an amplitude of 0.2mA. The tank is filled with saline and the measured conductivity is 424mS/m. There are two sets of measurements: one corresponds to a homogeneous tank and the other has an agar heart and lungs in the tank.

We first directly compare the voltages assuming we have ideal knowledge of the conductivity. In Figure 9.1 we see the relative percent errors, in the L^2 sense, between the measured voltages and the analytic and FEMCEM generated voltages. One can clearly observe that the FEMCEM voltages are much more accurate than the analytic solution. Specifically, the smallest error for the FEMCEM is 3.1% and for the analytic is 11.2%.

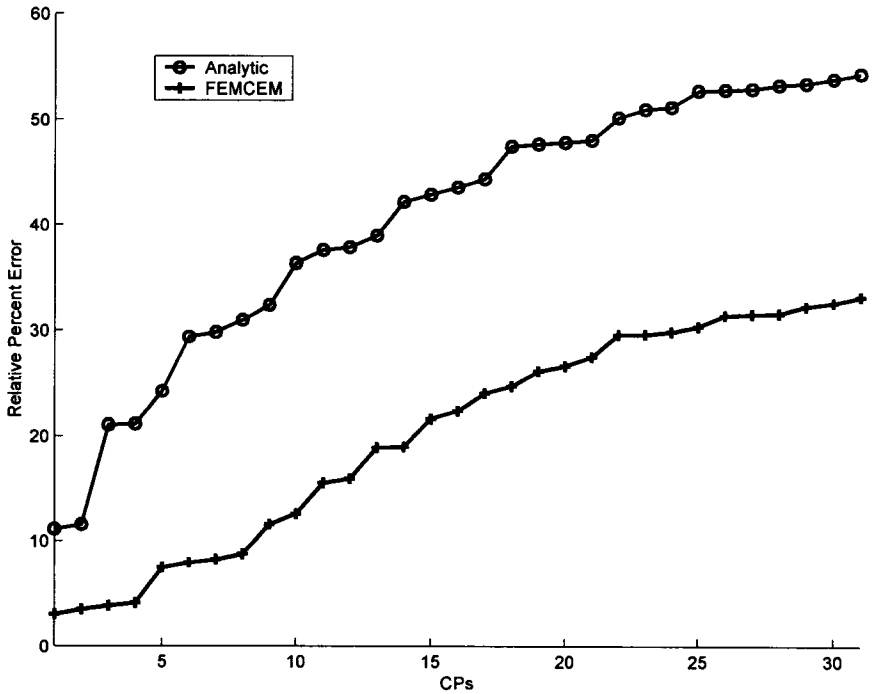

Figure 9.1: Sorted Relative percent error, in the L^2 sense, between measured voltages and the analytic and FEMCEM generated voltages over all the CPs.

Table 9.1: γ_{best} values calculated on the two sets of measured voltages. The ideal/measured conductivity of the saline is 424mS/m.

Voltages	γ_{best} for hom.	γ_{best} for heart and lungs
Analytic	499.0mS/m, 17.6%	421.0mS/m, 0.7%
FEMCEM	408.6mS/m, 3.6%	344.5mS/m, 18.7%

In practice we do not know the ideal/measured homogeneous voltages. Instead, an estimate is calculated, discussed in Section 3.2.3. In Table 9.1 we show the calculated γ_{best} values for the two sets of measured voltages.

As it turns out the analytic voltages for the tank with heart and lungs obtains an amazingly accurate estimate for the saline. However, in the homogeneous case the FEMCEM provides a much better estimate. It seems that for this case, since lungs take up much more space in the tank, the average conductivity should be less than the saline 424mS/m. However, since the analytic solution overestimates the conductivity it gives a very good estimate. In Figure 9.2 we illustrate the reconstructions of of the agar heart and lungs using Λ_1 generated from analytic voltages on the left and FEMCEM voltages on the right using γ_{best} from Table 9.1. The reconstructions, in Figure 9.2, appear comparable. The values for the heart are 818mS/m and 812mS/m which correspond to errors of 9% and 8% for the analytic and FEMCEM voltages, respectively. The values for the lungs are 199mS/m and 144mS/m which correspond to errors of 17% and 40%. We see in terms of values the analytic solution provides more accurate reconstructed conductivity values than reconstructions from FEMCEM.

It appears in this case the analytic solution has given a slightly better reconstruction than FEMCEM in terms of conductivity values, despite the fact that Figure 9.1 clearly shows that FEMCEM provides more accurate voltages for the homogeneous case. It seems we can conclude that the

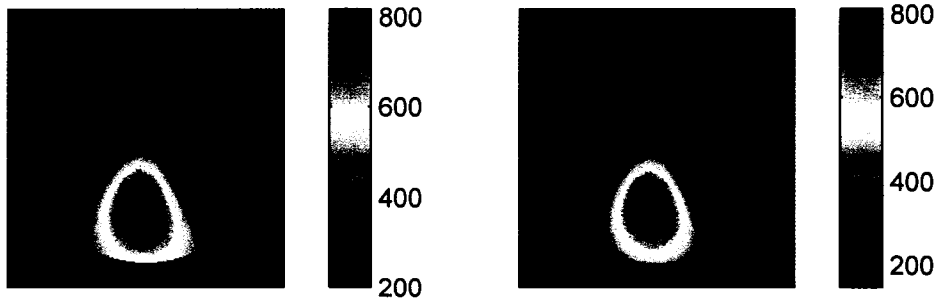

Figure 9.2: Reconstruction of the agar heart and lungs using Λ_1 generated from analytic voltages on the left and FEMCEM voltages on the right. A truncation radius of 3.5 was used.

analytic solution is reliable on circular domains, but it would seem to be more reasonable to use FEMCEM considering the voltage accuracy.

9.2 Domain Modeling Assumptions

There have been a series of publications using the D-bar method, all modeled on a circle [71, 72, 60, 59, 37, 38]. The effectiveness of proper modeling has been seen in Section 6.1 and Section 6.3. In this section, the domain modeling is isolated by the use of simulated data. In the previous reconstructions other factors may have caused errors.

In this section we use three domains for modeling purposes: the chest described above, an ellipse, or a circle. The ellipse has an axis ratio of 0.73 with a perimeter of 900mm. This results in the same ellipse used to model the elliptical ACT tank, and is roughly the size and shape of a human chest.

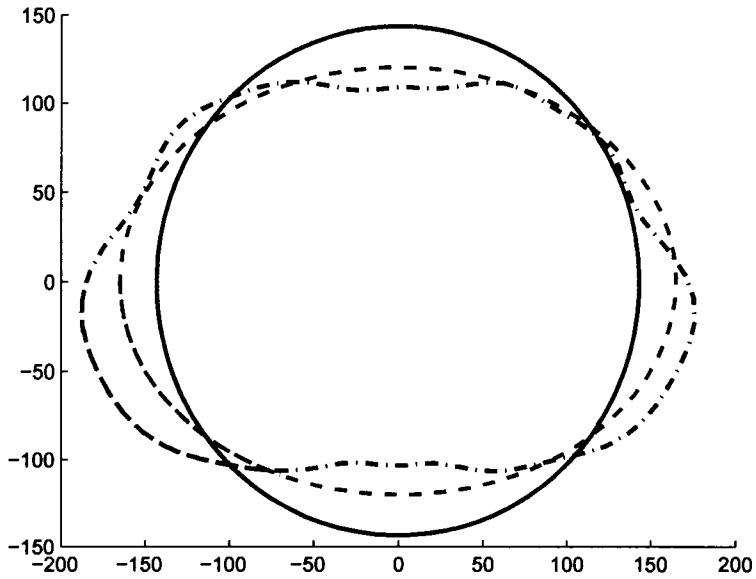

Figure 9.3: Comparison of the circle, ellipse, and chest domains.

The circle, which has a perimeter of 900mm as well, is the same circle used to model the reconstructions of the human chest data from Section 6.3 and from [38]. We illustrate the domains in Figure 9.3. Everything is simulated using FEMCEM, the inhomogeneous voltage data is simulated on the chest, and the following experiments are performed.

1. The first experiment uses simulated homogeneous voltages from the circle, ellipse, and chest. Reconstructions are then performed assuming the domain was a circle, ellipse, and chest, respectively, in the scattering transform calculation.

2. The second experiment uses homogeneous simulated voltages from the chest and reconstructions are performed assuming the domain was a circle, ellipse, and chest in the scattering transform calculation.

3. The final experiment uses the homogeneous simulated voltages from the circle and ellipse and then performs the reconstructions assuming a chest in the scattering transform calculation.

The first test should give insight into static reconstructions and the effects of approximate domain modeling and homogeneous voltage simulations. The second test isolates the effect of proper modeling in the scattering transform. The last test shows errors that arise from improper voltage measurements.

9.2.1 Test 1: Static Images

We have the reconstructions shown in Figure 9.4 and the values from the reconstructions shown in Table 9.2.1. All reconstructions show the general artifacts that are found in literature (for instance [41]). That is, when the domain is assumed to be a circle there is a large artifact in the center and objects are blurred/stretched. In these reconstructions it appears the heart moves to the center. This effect appears to be CP independent. The blurring is diminished with the elliptical domain, which is expected because its a good approximation of the chest. The conductivity values, seen in Table 9.2.1, do not follow any obvious trend. Due to variations in the choice of the truncation radius, it appears that the domain approximations do not greatly effect the error in conductivity values. The conclusion of this test is that to get the best possible spatial resolution one needs to model the domain as accurately as possible. However, at least, in this simulated case, approximate domains still produce meaningful reconstructions.

9.2.2 Test 2: Effects of proper modeling in t^{exp}

In Figure 9.5 we see the results for ACPs and dTCPs. The reconstructions using NOCP1s and OHCPs are omitted. Their reconstructions

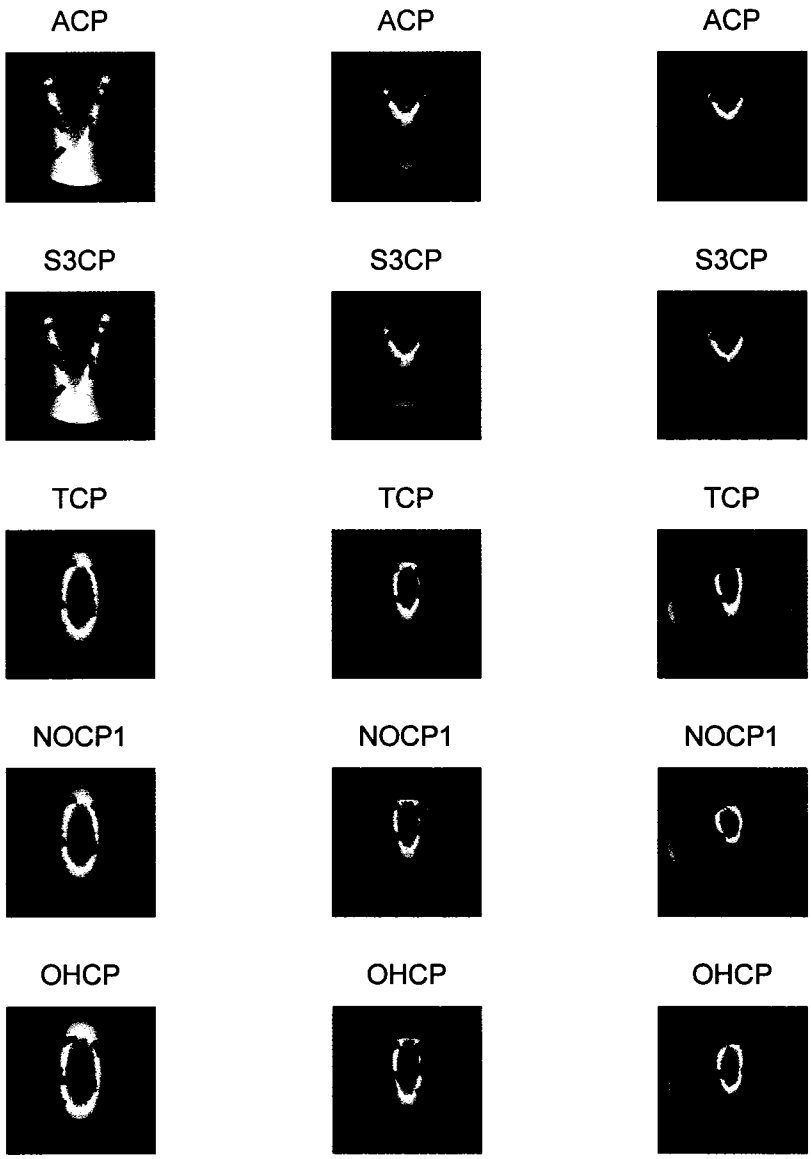

Figure 9.4: Comparison between conductivity reconstructions with an inhomogeneous voltage data from the chest with homogeneous voltage data from the circle, ellipse, and chest modeled in the scattering transform on the circle, ellipse, and chest, respectively.

Table 9.2.1: Errors in reconstructions for different CPs on different domains. Note, H and Ls are heart and lung conductivities, respectively, RE is relative error.

CP	Max H	Max H RE	Min Ls	Min Ls RE
ACP: Circle	1.71	14.5%	0.27	19.0%
Ellipse	1.54	23.0%	0.24	28.0%
Chest	1.86	7.0%	0.18	46.0%
dTCP: Circle	2.19	9.5%	0.39	17.0%
Ellipse	2.08	4.0%	0.31	7.0%
Chest	1.87	6.5%	0.31	7.0%
NOCP1: Circle	2.19	9.5%	0.39	17.0%
Ellipse	2.00	0.0%	0.30	10.0%
Chest	2.00	0.0%	0.29	13.0%
OHCP: Circle	2.19	9.5%	0.39	17.0%
Ellipse	1.81	9.5%	0.34	2%
Chest	2.00	0.0%	0.33	1.0%

are very similar to dTCPs. One can observe similar artifacts/blurring as seen in Figure 9.4, but with much more blurring into the boundary in the case of ACPs. It appears from these tests that it is the accurate domain modeling in the calculation of the scattering transform that is essential for good spatial resolution. Therefore, in order to verify this observation we go on to the third test that should isolate the contribution of the voltage measurements.

9.2.3 Errors due to incorrect voltage modeling

This test isolates the contribution of the effect of accurate voltage modeling. The scattering transform is calculated on a chest for each reconstruction. In Figure 9.6 the reconstructions are shown for dTCPs using simulated homogeneous voltage measurements. There is little blurring into the center with respect to the heart. The reconstructions using the circle and ellipse blend the lungs together.

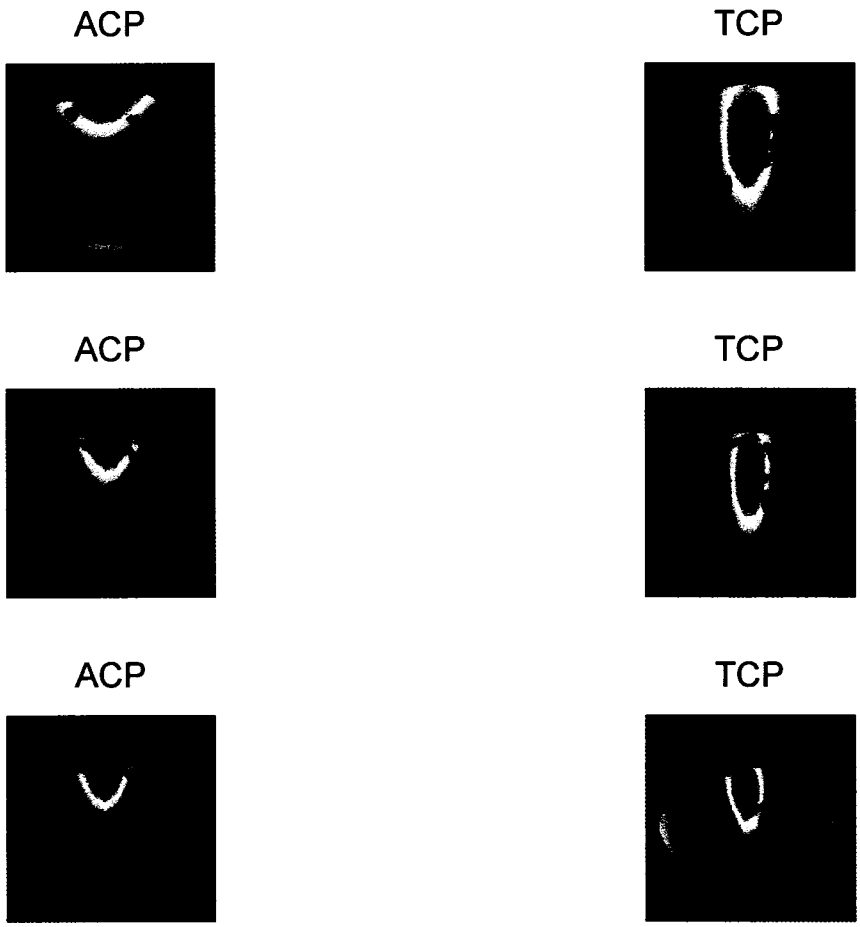

Figure 9.5: Comparison between conductivity reconstructions with inhomogeneous and homogeneous voltage data from the chest modeled in the scattering transform on the circle, ellipse, and chest.

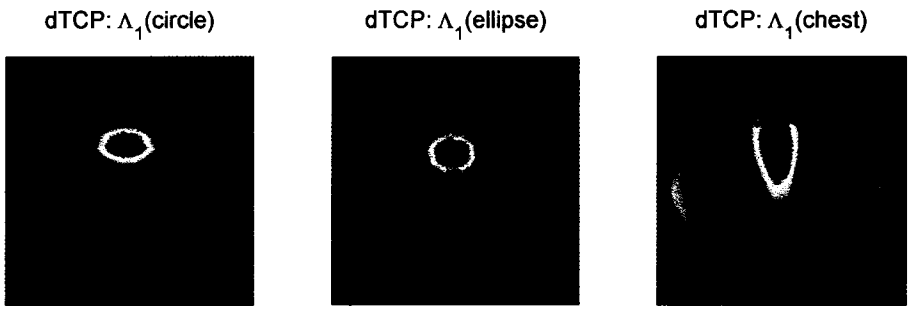

Figure 9.6: Comparison between conductivity reconstructions with an inhomogeneous voltage data taken on the chest and homogeneous voltage data taken on circle, ellipse, or chest. The scattering transform is calculated on a chest for each reconstruction.

The conclusion of this section is as one would expect, accurate domain modeling will produce the best reconstructions. However, contributions of different of the process to the error can be understood better. For instance, proper voltage modeling effects the reconstructions more than proper modeling in the scattering transform. Despite the fact that there is a lot of blurring in Test 2, one can at least observe two lungs.

9.3 Investigation into t_{diff}^{exp}

The term t_{diff}^{exp} refers to the calculation of the scattering transform shown in Chapter 5 where Λ_1 is constructed by a reference frame. A reference frame refers to a set of measured, not homogeneous, voltages. We can

think of t_{diff}^{exp} in the following way

$$\begin{aligned} t_{diff}^{exp}(k) &= t^{exp}(k;\gamma_1) - t^{exp}(k;\gamma_2), \\ &= \tfrac{1}{\gamma_b}\int_{\partial\Omega} e^{i\bar{k}\bar{z}}\left(\Lambda_{\gamma_1} - \Lambda_1\right) e^{ikz} d\sigma - \tfrac{1}{\gamma_b}\int_{\partial\Omega} e^{i\bar{k}\bar{z}}\left(\Lambda_{\gamma_2} - \Lambda_1\right) e^{ikz} d\sigma, \\ &= \tfrac{1}{\gamma_b}\int_{\partial\Omega} e^{i\bar{k}\bar{z}}\left(\Lambda_{\gamma_1} - \Lambda_{\gamma_2}\right) e^{ikz} d\sigma. \end{aligned} \tag{9.1}$$

In terms of (9.1) the reference frame used for differencing is used to construct Λ_{γ_2}. Also one can refer to the discussion between these difference images and the conventional type, $\gamma_1^{recon} - \gamma_2^{recon}$, in Section 5.4.

In [38] t_{diff}^{exp} was used successfully to produce reconstructions on human chest data using a selected reference frame from the full set of measurements. Taking an inhomogeneous reference frame for Λ_{γ_2} results in subtracting conductivities between Λ_{γ_1} and Λ_{γ_2}. In this section we propose to test this idea experimentally with simulated data on our simulated chest and measured data on the oval tank. The difference between results in [38] and reconstructions presented here is that we know all conductivities. Thus we should be able to conclude more accurately if this t_{diff}^{exp} is working the way it seems to be in [38].

9.3.1 Simulated chest data

We look at two reconstructions of heart and lungs. Λ_{γ_1} was formed from a simulated chest with a heart = 670mS/m and lungs = 100mS/m. In Figure 9.7 on the left we see Λ_{γ_2} formed from a simulated chest with a heart = 500mS/m and lungs = 200mS/m. On the right of Figure 9.7 Λ_{γ_2} is formed from a simulated chest with a heart = 750mS/m and lungs = 40mS/m. This is meant to approximate the voltage measurements that were used in [38]. In their study the reference frame was held fixed and

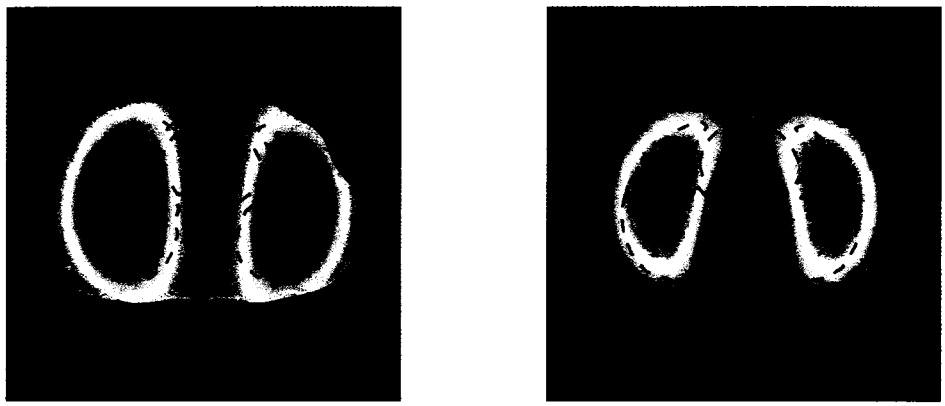

Figure 9.7: Reconstructions of t_{diff}^{exp} using Λ_{γ_1} with a heart = 670mS/m and lungs = 100mS/m using dTCP and different nonhomogeneous Λ_{γ_2}. On the left Λ_{γ_2} using a heart = 500mS/m and lungs = 200mS/m and on the right Λ_{γ_2} using a heart = 750mS/m and lungs = 40mS/m. The truncation radius was set to 2.4.

the voltage data that was used to form Λ_{γ_1} was changed. In Figure 9.7 we show reconstructions incorporating the same idea. On the left the heart conductivity is reduced and the lungs increased in Λ_{γ_2}. On the right the heart conductivity is increased and the lungs are decreased in Λ_{γ_2}. In terms of values the reconstructions in Figure 9.7 are a success. However, the heart appears to be blurred on the left of Figure 9.7, and it appears to have moved in the right of Figure 9.7. It might be a question of FEMCEM accuracy or maybe some other effect. Instead of drawing conclusions we look to another set of tests on measured data.

9.3.2 Oval tank data

In this subsection we look back to the oval tank data from the ACT 3 system. The full details of the setup are given in Section 6.1.1. We look at three sets of voltage measurements to determine the Dirichlet-to-Neumann maps. The map Λ_{γ_1} is constructed from the tank experiment with a PVC pipe placed $60mm$ on the minor axis and a copper pipe placed $80mm$ on the

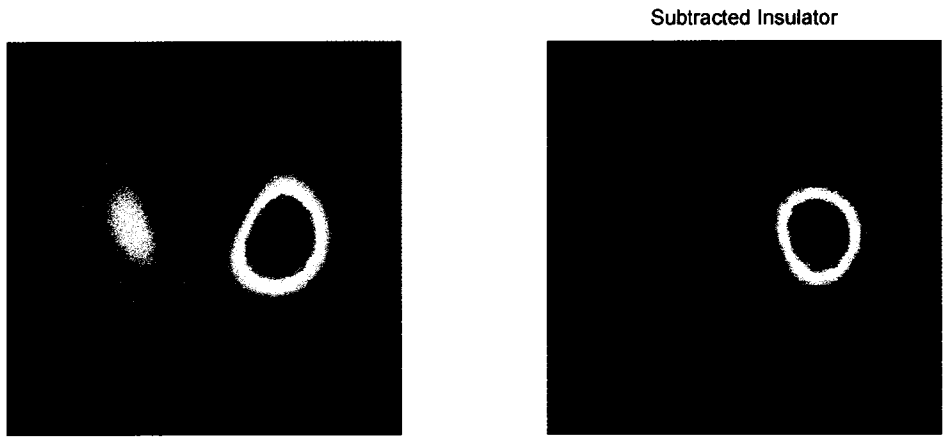

Figure 9.8: Reconstructions on the oval tank using Λ_{γ_1} constructed from a PVC pipe placed $60mm$ on the minor axis and a copper pipe placed $80mm$ on the major axis and Λ_{γ_2} constructed from a PVC pipe placed $60mm$ on the minor axis.

major axis. The map Λ_{γ_2} is constructed from either the experiment with a PVC pipe placed $60mm$ on the minor axis or a copper pipe placed $80mm$ on the major axis. The idea here, as above, is to see if we can actually subtract conductivities by taking the difference of Dirichlet-to-Neumann maps where Λ_{γ_2} is inhomogeneous.

In Figure 9.8 we attempt to subtract the insulator and in Figure 9.9 we attempt to subtract the conductor. Artifacts appear from the subtraction in Figure 9.8(right) and Figure 9.9(right). There appears to be an insulator just below the center in in Figure 9.8(right) and there seems to be a conductor left of center in Figure 9.9(right).

The t_{diff}^{exp} certainly needs to be studied more. It clearly provided good reconstructions in [38]. However, considering the tests shown in this section there are concerns about target locations and artifacts.

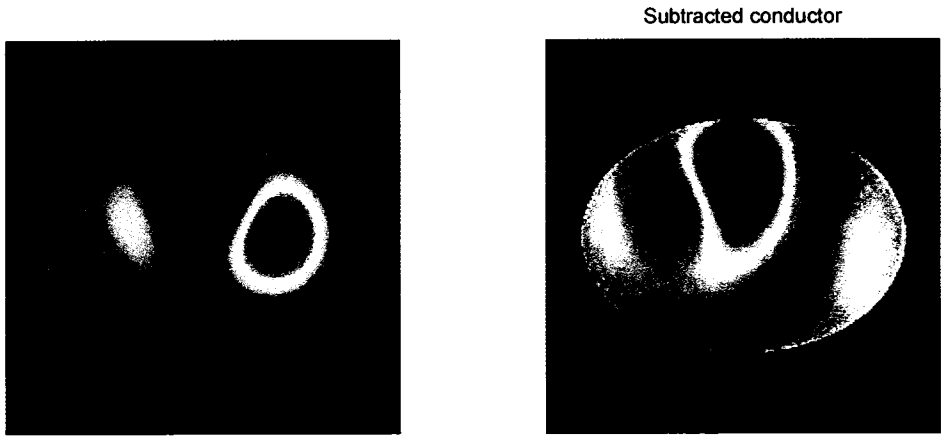

Figure 9.9: Reconstructions on the oval tank using Λ_{γ_1} constructed from a PVC pipe placed $60mm$ on the minor axis and a copper pipe placed $80mm$ on the major axis and Λ_{γ_2} constructed from a copper pipe placed $80mm$ on the major axis.

9.3.3 Comparison between different difference images

We have stated earlier in this dissertation that there are conventional difference images and difference images produced from t^{exp}_{diff}. Thus far in this section we have only looked at difference images using t^{exp}_{diff}. Since we have measured homogeneous data from the ACT 3 oval tank study we can compare conventional difference images with the once we've found so far. We are assuming that conventional different images reconstruct γ_1 from voltage measurements corresponding to a inhomogeneous tank, reconstruct γ_2 from voltage measurements corresponding to a homogeneous tank, and take the difference $\gamma_{diff} = \gamma_1 - \gamma_2$. We show the results of two test in Figure 9.10 and Figure 9.11. In this case the difference images look almost identical and it is hard to argue which one is better.

9.4 Analysis of Errors due to electrode placement: Rotations

In all experimental data the electrodes are placed slightly off from their ideal positions. It is important to know if the results are sensitive

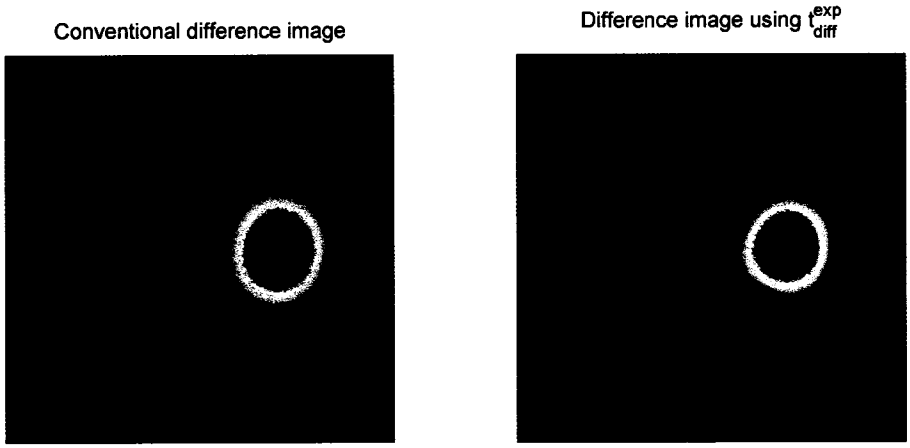

Figure 9.10: Reconstructions on the oval tank constructed from a PVC pipe placed $80mm$ on the major axis.

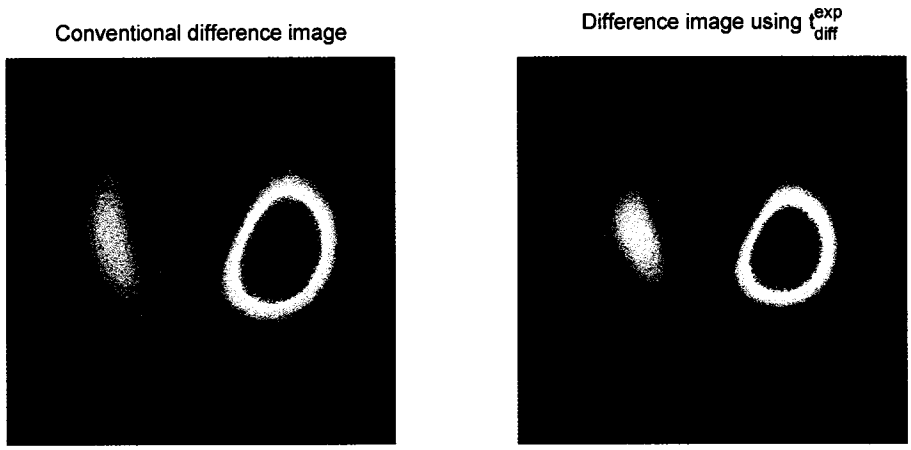

Figure 9.11: Reconstructions on the oval tank constructed from a PVC pipe placed $60mm$ on the minor axis and a copper pipe placed $80mm$ on the major axis.

to placement and to know what the tolerance is for the placement. Thus, in this section we look at errors in the reconstruction due to rotated electrodes. The choice of rotated electrodes as opposed to randomly perturbed electrodes was chosen because of the wide electrode configuration used in dTCP, NOCP1 and OHCP. The electrode gap in those cases is about 2 mm with a perimeter of 900 mm. Consequently, it was much easier to rotate the electrodes than to deal with the cases of overlapping electrodes when trying to apply random perturbations.

The homogeneous experiment is assumed 'ideal', that is, no rotation of electrodes and no error is applied to electrodes. The inhomogeneous simulated voltages have the electrodes rotated in the counterclockwise direction. The rotations we consider are 1% (9mm), 2% (18mm), 3% (27mm), and 4% (36mm) of the perimeter. Recall, that the electrodes are of width 25.4mm for dTCP, NOCP1, and OHCP and 10mm for ACP and S3CP. Therefore, a rotation of 3% is rotating the inhomogeneous setup by a full electrode. It would not be surprising if the reconstructions were completely useless at that point. Illustrations of the rotations of 2% and 4% can be seen in Figure 9.12, the black segments are rotated electrodes and the blue segments are the ideal placement. The reconstructions are presented in Figures 9.13 and Figure 9.14. The most stable reconstructions occur on the circular domain, i.e. the left column of Figure 9.13. There is no large error in the reconstructions. This is strong support for the claim that one should model on a circular domain if knowledge of the experimental setup is lacking or inaccurate.

The reconstructions on the chest with ACP and S3CP are also very stable. As the electrodes are rotated counterclockwise, the reconstructions

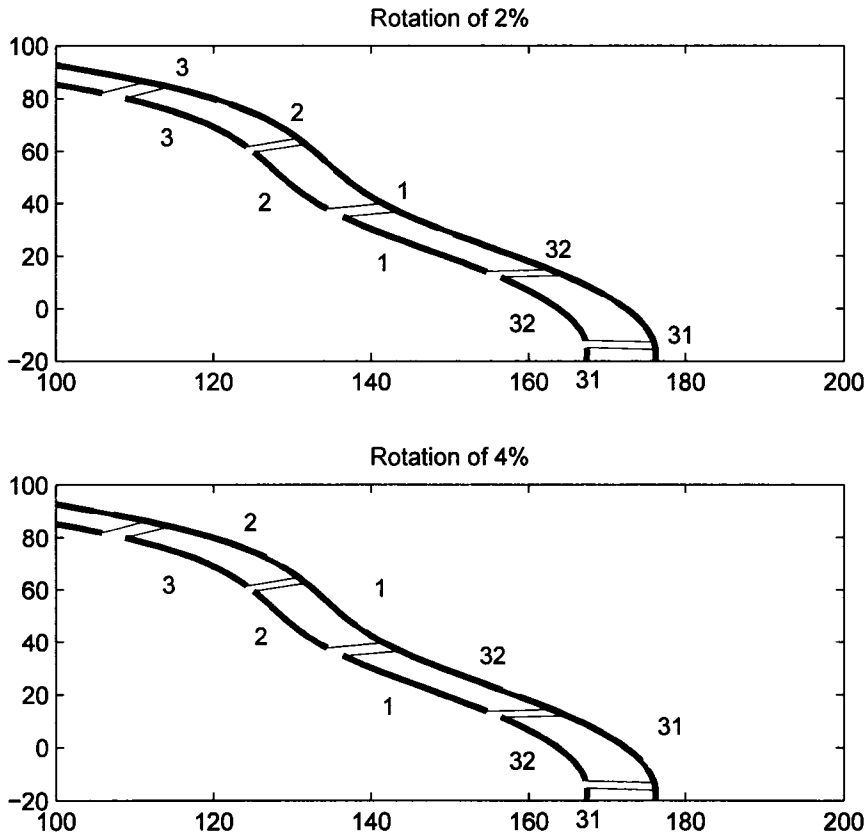

Figure 9.12: Illustration of 2% and 4% rotated electrodes. The black segments are rotated electrodes and the blue segments are the ideal placement. Electrodes are rotated counter clockwise.

Figure 9.13: Reconstructions from simulated data with electrode rotations of 0%, 1%, 2%, 3% and 4% for dTCP on a circle, ACP, and S3CP.

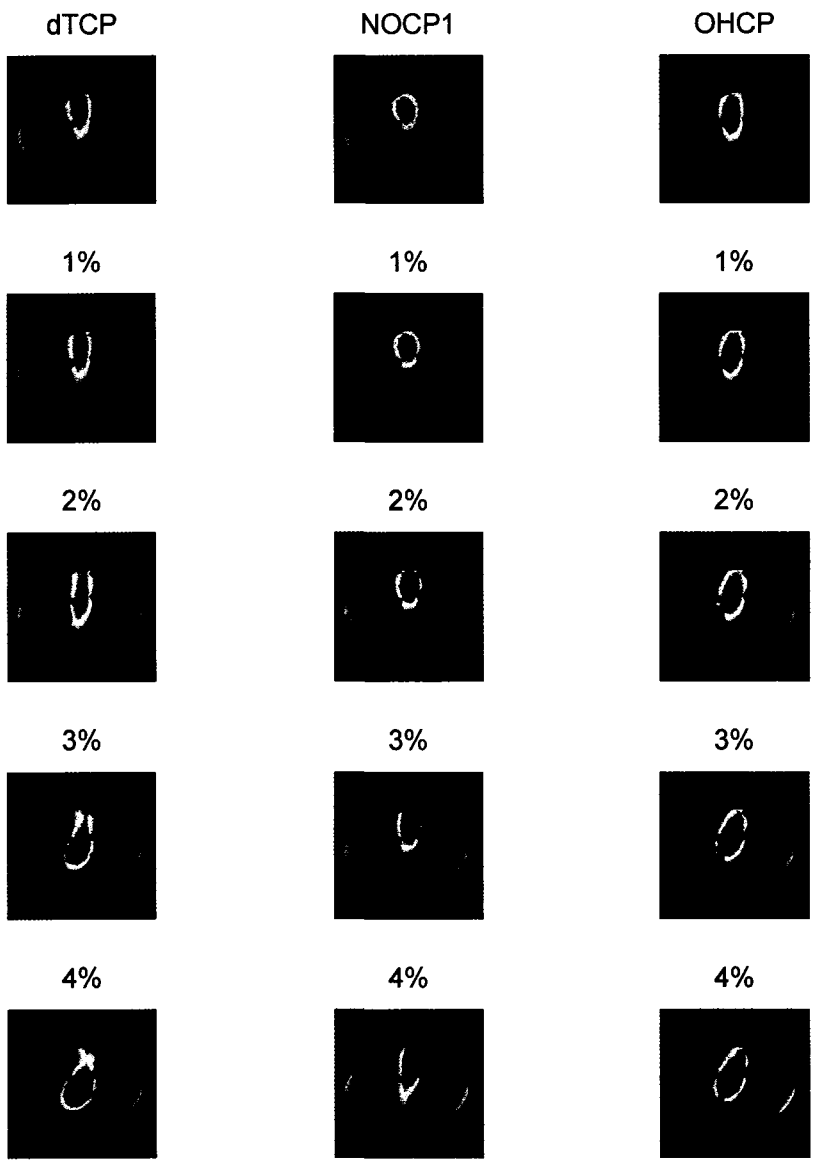

Figure 9.14: Reconstructions from simulated data with electrode rotations of 0%, 1%, 2%, 3% and 4% for dTCP, NOCP1, and OHCP.

appear to be rotating clockwise. The spatial resolution is satisfactory all the way to 4% error. However, the reconstructed conductivity values remain accurate up to 3% rotation.

The last three figures show the dTCP, NOCP1, and OHCP reconstructions on a chest. The dTCPs remain satisfactory up to 2% rotation, NOCP1s up to 3%, and OHCPs up to 4%. In the case of OHCPs the conductivity values become inaccurate after 1% rotation. The conclusion seems to be that the D-bar reconstruction method is very robust to electrode placement. Therefore, these tests indicate that artifacts in reconstruction from the ACT 3 system are not caused by electrode placement.

9.5 Errors in voltages measurements

The measured voltages always have some noise. In this section we apply noise to the voltage data from the inhomogeneous domain. We assume here that the noise would come from measurement on the electrodes. Specifically, uniform random variables are used to add noise to the measurement within $\pm 0.01mV$, $\pm 0.1mV$, and $\pm 1mV$ of the specified voltage. In this test we apply currents to the simulated chest, measure voltages, and then apply noise to the voltages.

In Table 9.5 we show relative errors for dTCP(circle), ACP, and dTCP (chest). We show the relative errors because the different CPs have different maximum voltages. Thus, the relative errors vary depending on the CPs. We do not include the other CPs because S3CPs are close to ACPs and NOCP1s and OHCPs are very close to dTCP(chest). We note that the relative errors are the largest since the maximum of ACPs is so small.

In Figure 9.15 and Figure 9.16 we show the reconstructions corresponding to the voltage errors. In fact the majority of the reconstructions

Table 9.5: Calculated relative errors (RE) for the noise added to measurements for different CPs.

CPs	dTCP(circle)	ACP	dTCP
Max Volts	280.98	34.91	356.58
Max RE $\pm 0.01mV$	0.06%	0.095%	0.068%
Max RE $\pm 0.1mV$	0.57%	0.85%	0.70%
Max RE $\pm 1mV$	5.94%	8.92%	6.25%

are good. A few reconstructions are less good, i.e. $\pm 1mV$ for ACPs and dTCP(chest). However, $\pm 1mV$ seems to be quite a large error. It seems if the error is within $\pm 0.1mV$ then there are no significant artifacts. As was the case for the electrode rotations, the D-bar method is robust for reasonable voltage errors.

9.6 Errors in injected currents

In this section we consider the application of noise to the injected currents in the inhomogeneous data. That is, we apply noise to the current and then calculate the corresponding voltage data. We randomly perturb the current within $\pm 0.001mA$, $\pm 0.005mA$, $\pm 0.01mA$, and $\pm 0.02mA$ of the specified current using a uniform distribution. Since the amplitude of the current is 1mAmp we can think of the errors in the experiments as one-hundredth of the relative errors we are creating, i.e., $\pm 0.001mA$ is equivalent to 0.1% relative error.

In Table 9.6 we show the relative errors of the injected currents and the corresponding relative errors in voltage measurements that result for dTCP(circle), ACP and dTCP(chest). We do not include the other CP relative errors for the reason cited above. A clear implication of this test is that small current noise results in large voltage error. For instance, for

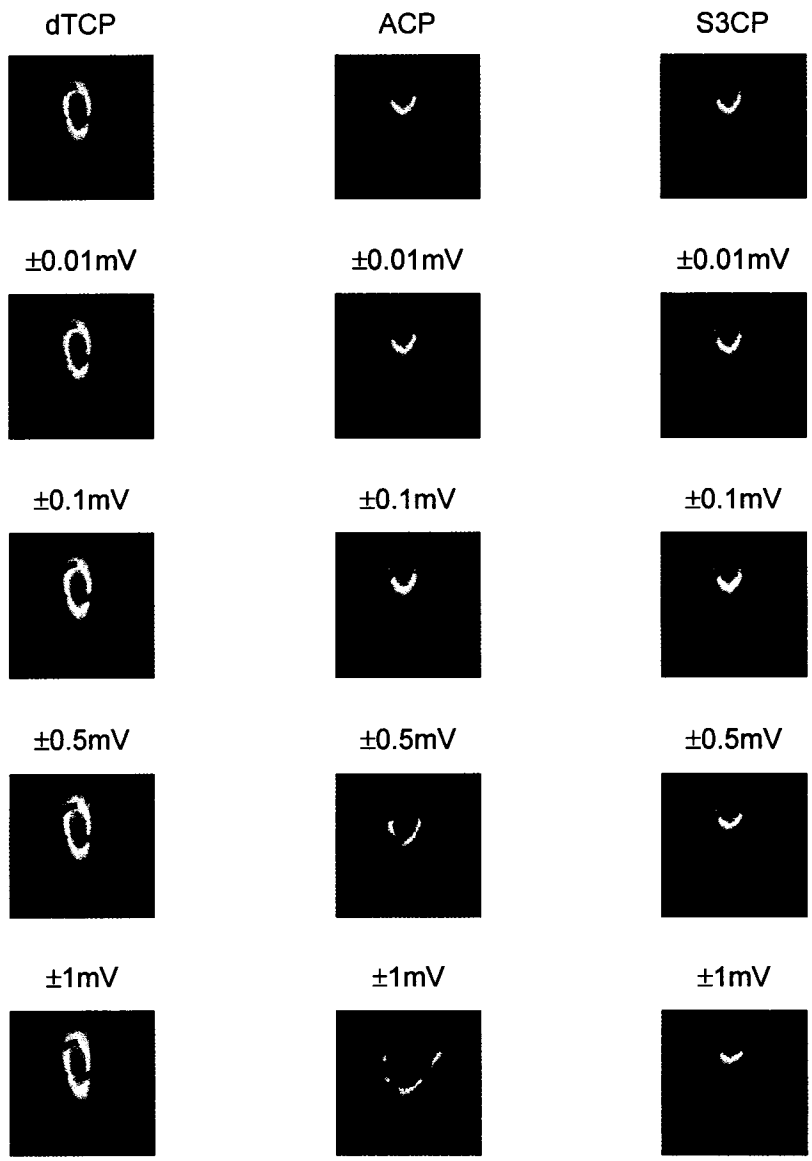

Figure 9.15: Reconstructions from simulated data with voltage error of within $\pm 0.01mV$, $\pm 0.1mV$, and $\pm 1mV$ of the specified voltage for dTCP on a circle, ACP, and S3CP.

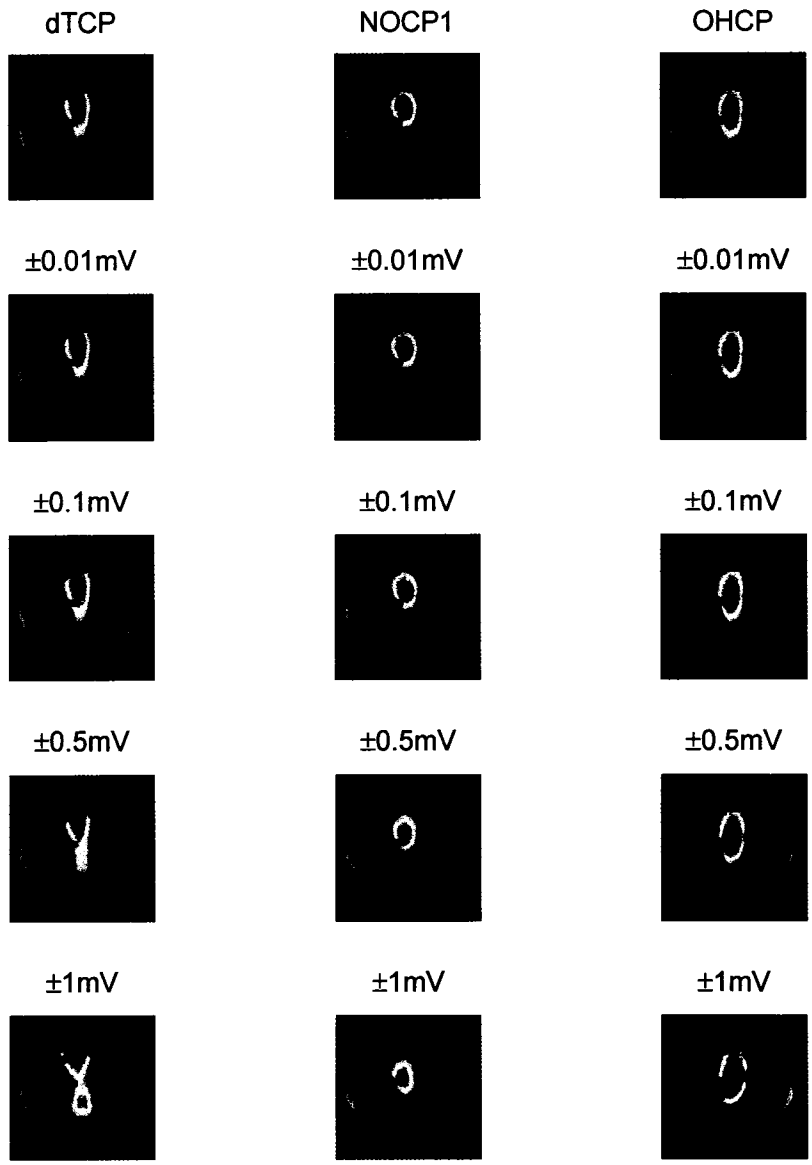

Figure 9.16: Reconstructions from simulated data with voltage error of within $\pm 0.01mV$, $\pm 0.1mV$, and $\pm 1mV$ of the specified voltage for dTCP, NOCP1, and OHCP.

Table 9.6: Calculated relative errors (RE) for the noise added to measurements for different CPs.

CPs (Amplitude 1mA)	dTCP(circle)	ACP	dTCP
Norm CPs	4 or 5.66	1.41	
Max RE $\pm 0.001mA$	0.091%	0.258%	
Max RE $\pm 0.005mA$	0.494%	1.408%	
Max RE $\pm 0.02mA$	2.044%	5.643%	
Max RE Volts	0.63%	1.24%	0.73%
Max RE Volts	2.88%	4.50%	3.52%
Max RE Volts	13.26%	23.19%	18.13%

dTCP circle 2% in the current results in 13% in the voltages. We see, again, that ACPs are the most susceptible to noise.

In Figure 9.17 and Figure 9.18 we the reconstructions corresponding to the current noise. Once again, we see the best stability with dTCP(circle). The reconstructions from ACP and S3CP become unreliable after 0.005mA error. We have a similar error in dTCP(chest) for the largest error of 0.05 as in Figure 9.16. As with the rest of the reconstructions, the D-bar method seems pretty stable to current noise. Considering that the ACT 3 system is able to inject CPs within 0.05% accuracy of the specified amplitude, i.e. $\pm 0.0005mA$ if the amplitude is $1mA$, it seems that current errors that small should produce no noticeable effect.

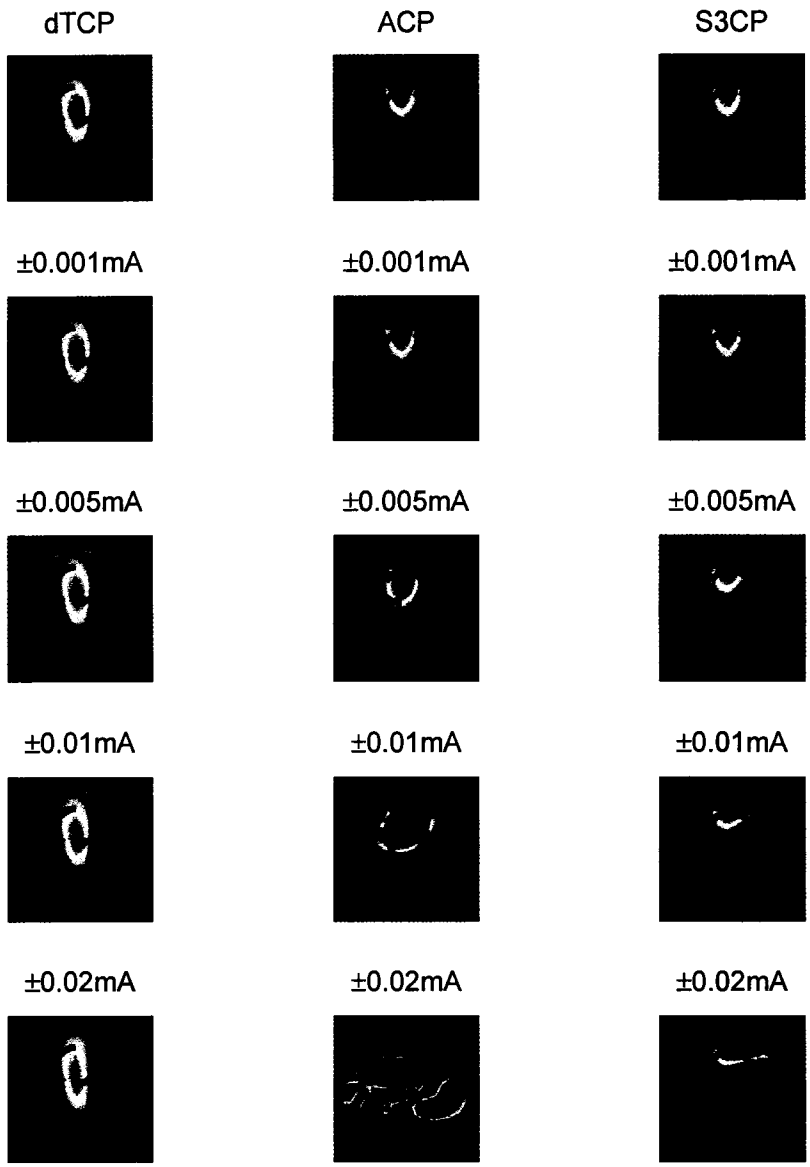

Figure 9.17: Reconstructions from simulated data with randomly perturbed current within $\pm 0.001mA$, $\pm 0.005mA$, $\pm 0.01mA$, and $\pm 0.02mA$ of the specified current for dTCP on a circle, ACP, and S3CP.

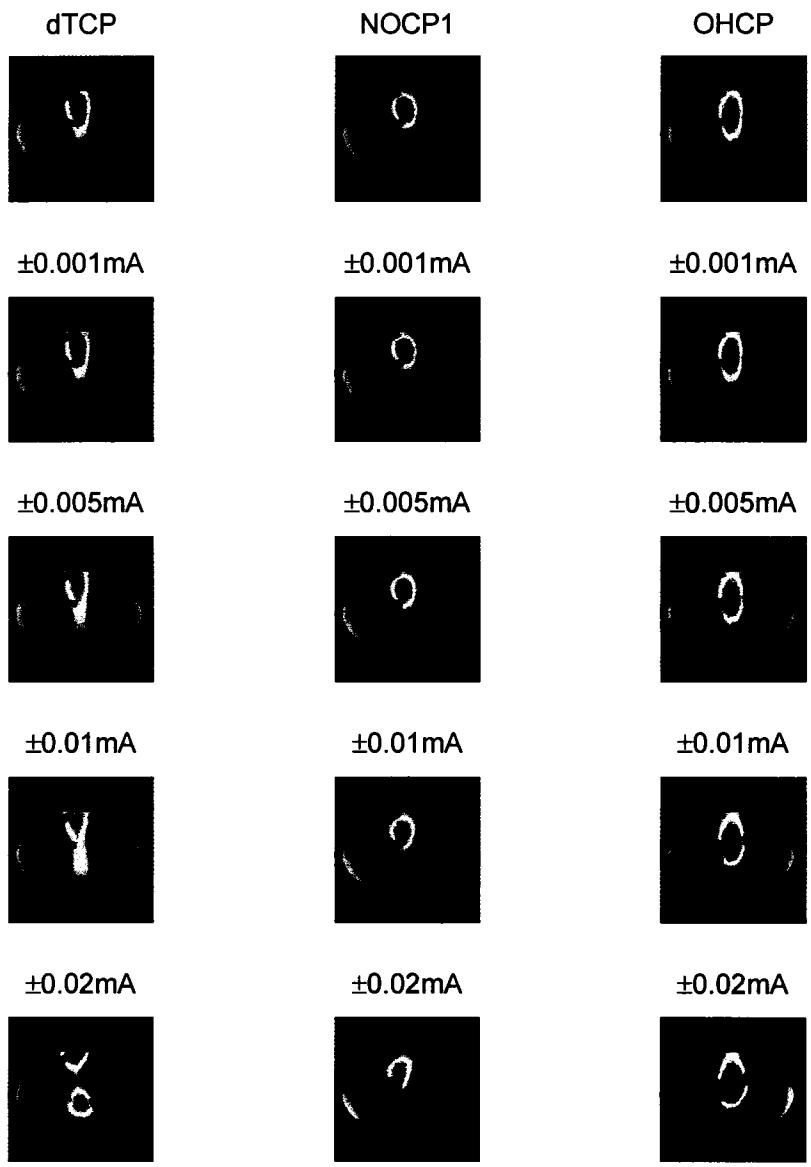

Figure 9.18: Reconstructions from simulated data with randomly perturbed current within $\pm 0.001mA$, $\pm 0.005mA$, $\pm 0.01mA$, and $\pm 0.02mA$ of the specified current for dTCP, NOCP1, and OHCP.

Chapter 10

ANALYSIS OF SCATTERING TRANSFORMS

In this chapter we propose a simple way to improve the regularization of the scattering transform. In Figure 10.1 we show the static scattering transform corresponding to ACT 3 data on an elliptical domain with a copper and pvc pipe. One can clearly see that the scattering transform begins to 'blow-up' in different directions near the boundary. In this case, we have regularized the problem by truncating the scattering transform at 2. In the reconstructions in [62] the truncation radius was extended to 3 and good reconstructions were found, see top left of Figure 10.2. We want to suppress the 'blow-up' in the scattering transform, although, theoretically we want the scattering transform for all k. Numerically, this is equivalent to keeping the scattering transform as far out as is practical. The restriction to truncating a circle limits this method. Thus we propose to truncate the scattering transform when the slope gets 'too large'.

We see reconstructions with this approach in Figure 10.2 for maximum slopes of 3, 4, and 5 resulting in maximum truncation radii of 3.9, 4.5, and 4.5, respectively. The shapes of the truncations are shown in Figure 10.3 and the slopes the scattering transform are shown in Figure 10.4. There is improvement in artifacts and spatial resolution of the targets in the tank.

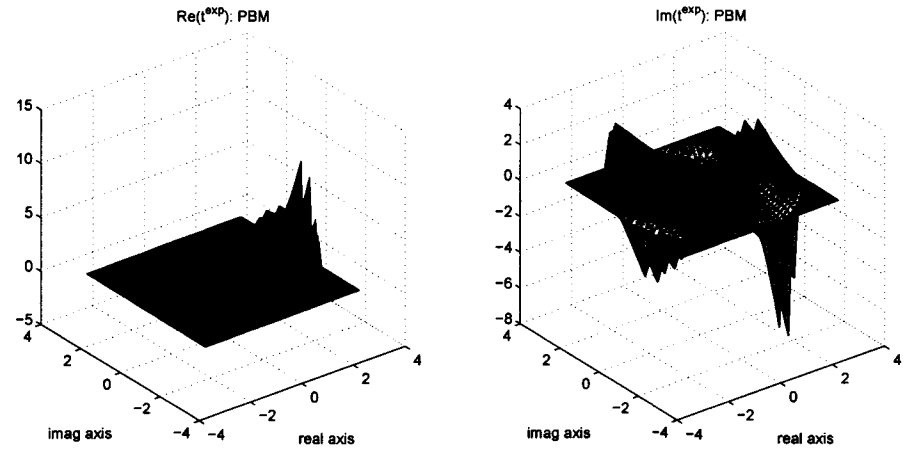

Figure 10.1: Static Scattering transform corresponding to ACT 3 data on an elliptical domain with a copper and pvc pipe with a truncation radius of 2.

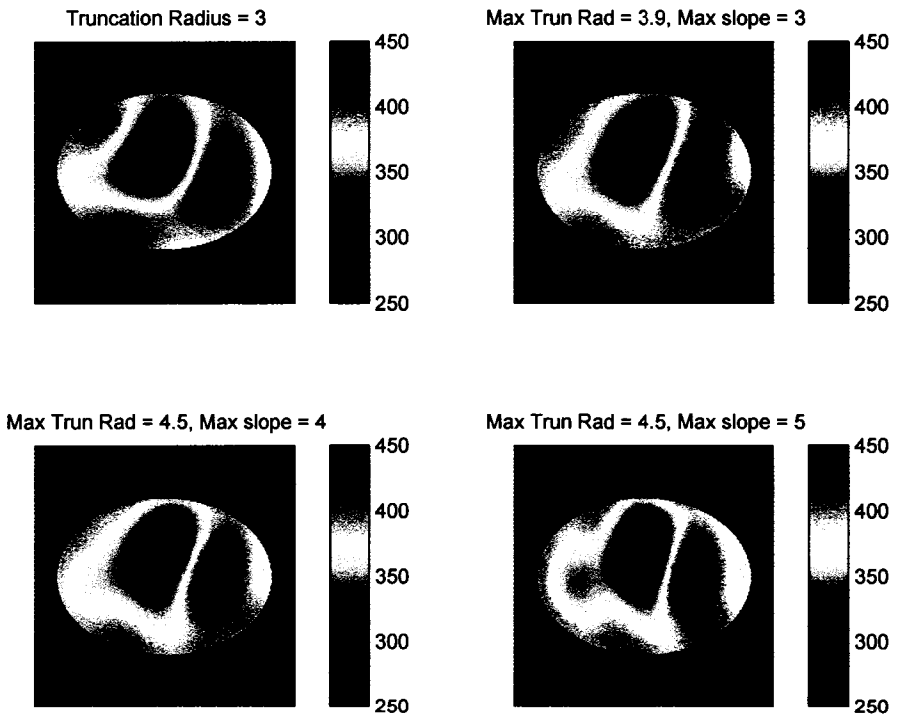

Figure 10.2: Reconstructions comparing different types of truncation in the scattering transform.

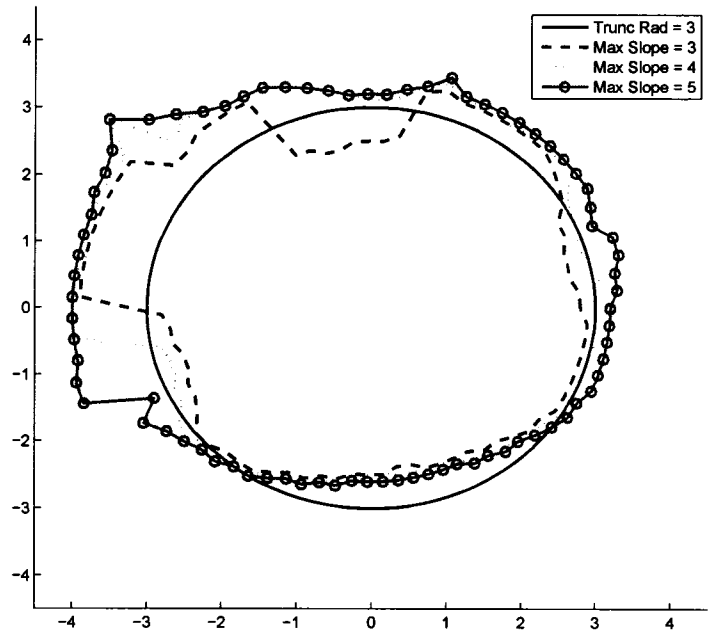

Figure 10.3: Truncations for scattering transforms.

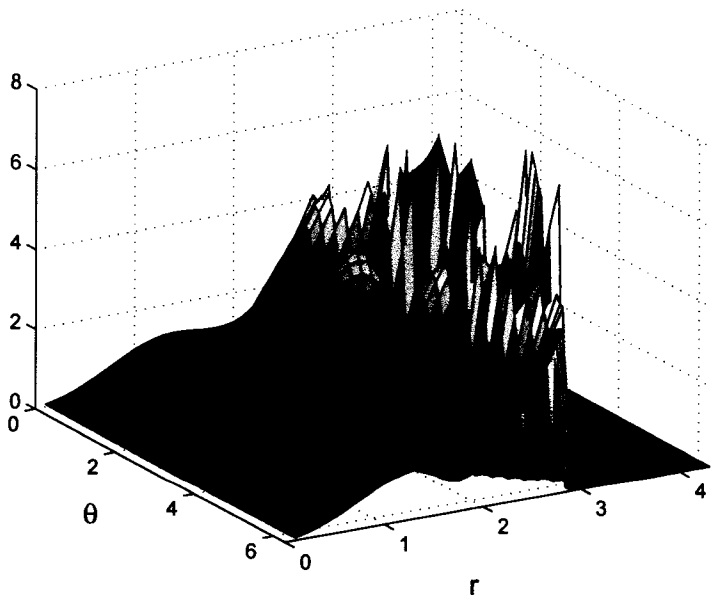

Figure 10.4: Slopes of the scattering transform.

Chapter 11

LAYER-STRIPPING

The layer-stripping technique in the EIT problem has been studied quite thoroughly. As discussed earlier, when applied to measured data, the algorithm does not produce good results. We propose to perform layer-stripping just to obtain the conductivity and normal derivative of the conductivity on the boundary. The hope is that the algorithm is stable enough for this. Knowledge of $\gamma|_{\partial\Omega}$ and $\frac{\partial\gamma}{\partial\nu}\big|_{\partial\Omega}$ is essential to implement the first step of Nachman's D-bar method. We assume the implementation of the first step should improve reconstructions.

We present the algorithm described in [75] by Somersalo, Cheney, D. Isaacson, and E. Isaacson from 1991 for recovering γ on the boundary of a unit disc. Next we are interested in reconstructing the conductivity inside the boundary. Generally, this would not be advisable because of the instability of the method, but since, we only need to go in one step in order to obtain enough information for a finite difference approach to obtain the normal derivative of the conductivity, our hope is the method is stable enough to produce accurate reconstructions of $\frac{\partial\gamma}{\partial\nu}\big|_{\partial\Omega}$.

11.1 Theory of Layer-Stripping

Layer-stripping uses the conductivity equation (1.1) and the Neumann-to-Dirichlet map $R : j \mapsto u|_{\partial\Omega}$. We describe the construction of the layer-stripping method for circular domains presented in [75]. We present the steps in order to understand the theory and to investigate the possibility of generalizing the method to non-circular domains. The algorithm is composed of two parts. First γ is constructed on the boundary, second we construct the Neumann-to-Dirichlet map for an inner layer. The conductivity is reconstructed on that layer and steps are repeated.

11.1.1 Construction of γ on the boundary

We consider the Neumann problem

$$\begin{aligned} \nabla \cdot (\gamma(x,y)\nabla u(x,y)) &= f, \quad (x,y) \in \Omega, \gamma(x,y) \\ \frac{\partial u}{\partial \nu}(x,y) &= j(x,y) \quad (x,y) \in \partial\Omega. \end{aligned} \tag{11.1}$$

where u is assumed to be grounded on the boundary and where f and j are subject to the integral constraint

$$\int_\Omega f dx = \int_{\partial\Omega} j dS.$$

This condition is necassary for the existence of the solution. We define the map T_γ by

$$T_\gamma(f,j) = u.$$

Note that T_γ is related to resistivity map R_γ by taking $f = 0$ and restricting u to the boundary. Thus

$$R_\gamma = tT_\gamma|_{\{0\}\times H^{s+1/2}(\partial\Omega)}$$

where t is the trace map. We use the following proposition.

Proposition 11.1.1. *The operator T_γ admits a decomposition*

$$T_\gamma = \frac{1}{\gamma} T_1 + T_R, \tag{11.2}$$

where T_R is a mapping $H^s(\Omega) \times H^{s+1/2}(\partial\Omega) \to H^{s+3}(\Omega)$, $s \geq 0$.

The proof of Proposition 11.1.1 is shown in [75]. Using the result of Proposition 11.1.1 we can convert the T's in (11.2) to R's by the following

$$\begin{aligned} R_\gamma &= tT_\gamma|_{\{0\}\times H^{s+1/2}(\partial\Omega)} \\ &= t\tfrac{1}{\gamma}T_1|_{\{0\}\times H^{s+1/2}(\partial\Omega)} + tT_R|_{\{0\}\times H^{s+1/2}(\partial\Omega)} \\ &= \tfrac{1}{\gamma}|_{\partial\Omega} R_1 + R_R \end{aligned} \tag{11.3}$$

Note R_1 is the Neumann-to-Dirichlet map with $\gamma = 1$. Here Somersalo, et al. assume the domain is a unit disc and calculate R_1. The conductivity equation can be written in polar form, one can apply separation of variables, and solve the ODE to get the solution

$$u(r,\theta) = \sum_{m=-\infty,\ m\neq 0}^{\infty} c_m r^{|m|} e^{im\theta}. \tag{11.4}$$

The boundary condition can be written as a Fourier series, which gives

$$c_m = \frac{1}{|m|} j_m.$$

If $j = e^{im\theta}$ we have

$$R_1 : e^{im\theta} \to \frac{1}{|m|} e^{im\theta} \tag{11.5}$$

Define the matrix form in the Fourier basis of the Neumann-to-Dirichlet map as

$$R_{m,n} = \langle e^{im\theta}, R_\gamma e^{in\theta} \rangle, \tag{11.6}$$

where the inner product is assumed to be given by

$$\langle f, g \rangle = \frac{1}{2\pi} \int_{-\pi}^{\pi} \bar{f} g d\theta.$$

Define the Fourier coefficients of the resistivity as

$$\rho_n = \frac{1}{2\pi}\int_0^{2\pi} e^{-in\theta}\frac{1}{\gamma(1,\theta)}d\theta. \tag{11.7}$$

Proposition 11.1.2. *Let Ω be the unit disc, and assume that γ is smooth. Then*

$$\lim_{|n|\to\infty} |n| R_{n+k,n} = \rho_k \tag{11.8}$$

The result of this proposition is that the high frequency limit of R_γ gives the conductivity on the boundary. We omit the proof, but include the first step. The proof of Proposition 11.1.2 relies on the decay of the operator R_R in the Fourier basis. If we take (11.3) and multiply on the left and right side by $e^{im\theta}$ and $e^{in\theta}$, respectively, and integrate, we get

$$\langle e^{im\theta}, R_\gamma e^{in\theta}\rangle = \langle e^{im\theta}, \frac{1}{\gamma}\Big|_{\partial\Omega} R_1 e^{in\theta}\rangle + \langle e^{im\theta}, R_R e^{in\theta}\rangle. \tag{11.9}$$

Represent the resistivity by

$$\frac{1}{\gamma}|_{\partial\Omega} = \rho(\theta) = \sum_{k=-\infty}^{\infty} \rho_k e^{ik\theta}. \tag{11.10}$$

Then (11.9) simplifies to

$$\begin{aligned} \langle e^{im\theta}, R_\gamma e^{in\theta}\rangle &= \langle e^{im\theta}, \textstyle\sum_{k=-\infty}^{\infty} \rho_k e^{ik\theta} R_1 e^{in\theta}\rangle + \langle e^{im\theta}, R_R e^{in\theta}\rangle \\ R_{m,n} &= \textstyle\sum_{k=-\infty}^{\infty} \rho_k \langle e^{im\theta}, \frac{1}{|n|} e^{i(k+n)\theta}\rangle + \langle e^{im\theta}, R_R e^{in\theta}\rangle \\ R_{m,n} &= \tfrac{1}{|n|}\rho_{m-n} + \langle e^{im\theta}, R_R e^{in\theta}\rangle, \end{aligned} \tag{11.11}$$

by using (11.5), (11.6), (11.9), and (11.10). We get the specific indices on ρ_{m-n}, since there are only contributions when $-m+k+n=0$. The remainder of the proof shows that the operator R_R in the Fourier basis decays as m and n get large. Once this is established one can let $m = n+k$ and take the limit in (11.11) to get the result of Proposition 11.1.2.

11.1.2 Subsurface synthesis

In order to reconstruct the conductivity values in the interior of the domain we derive the Riccati equation on a disc of radius r. Our problem is now

$$\begin{aligned} \nabla \cdot (\gamma \nabla u) &= f, \quad |x| < r \\ \gamma \partial_r u &= j, \quad |x| = r. \end{aligned} \tag{11.12}$$

We now denote the Neumann-to-Dirichlet operator as

$$R_{\gamma,r} : j \mapsto u|_{\partial\Omega} \tag{11.13}$$

To see how $R_{\gamma,r}$ changes in the interior, we differentiate, giving

$$\partial_r u = \partial_r \left(R_{\gamma,r} j \right) = (\partial_r R_{\gamma,r}) j + R_{\gamma,r} \partial_r j. \tag{11.14}$$

Another form of the last term in (11.14) is found by differentiating the Neumann boundary condition in (11.12) with respect to r, i.e.

$$\partial_r j = \partial_r (\gamma \partial_r u). \tag{11.15}$$

We recall that the Laplace equation in polar coordinates is

$$\partial_r (\gamma \partial_r u) + \frac{\gamma}{r} \partial_r u + \frac{1}{r^2} \partial_\theta (\gamma \partial_\theta u) = 0 \tag{11.16}$$

Next we substitute (11.16) into (11.14) using (11.15) to get

$$\partial_r u = (\partial_r R_{\gamma,r}) j - R_{\gamma,r} \left(\frac{\gamma}{r} \partial_r u + \frac{1}{r^2} \partial_\theta (\gamma \partial_\theta u) \right). \tag{11.17}$$

We write (11.17) in terms of $R_{\gamma,r}$ by using (11.14), shown below

$$\left(\partial_r R_{\gamma,r} \right) j = \frac{j}{\gamma} + \frac{1}{r} R_{\gamma,r} j + \frac{1}{r^2} R_{\gamma,r} \left[\partial_\theta \left(\gamma \partial_\theta R_{\gamma,r} j \right) \right]. \tag{11.18}$$

This equation (11.18) is a Riccati equation. In [75] the next step is to show that a $R_{\gamma,r}$ is differentiable. We omit their results. We continue the

calculation. Using a Fourier basis we can express (11.18) in a way that is easy to compute. First we use the substitution $W_{\gamma,r} = \frac{1}{r}R_{\gamma,r}$ and the relation

$$r\partial_r W_{\gamma,r} = r\partial_r\left(\frac{1}{r}R_{\gamma,r}\right) = -\frac{1}{r}R_{\gamma,r} + \partial_r R_{\gamma,r},$$

and write (11.18), excluding j, as

$$r\partial_r W_{\gamma,r} = \frac{1}{\gamma} + W_{\gamma,r}\left[\partial_\theta\left(\gamma\partial_\theta W_{\gamma,r}\right)\right]. \tag{11.19}$$

We next define the Fourier representation of the operator $W_{\gamma,r}$ as

$$w_{m,n}(r) = \frac{1}{2\pi}\int_{-\pi}^{\pi} e^{-im\theta}W_{\gamma,r}(e^{in\cdot})(\theta)d\theta. \tag{11.20}$$

If we multiply (11.19) by $e^{-im\theta}$ and $e^{in\theta}$ on the left and right, respectively, we get after integrating,

$$\begin{aligned} r\tfrac{d}{dr}w_{m,n} &= \langle e^{im\theta}, \left(\textstyle\sum_{k=-\infty}^{\infty}\rho_k\right)e^{ik\theta}e^{in\theta}\rangle + \langle e^{im\theta}, W_{\gamma,r}\left[\partial_\theta\left(\gamma\partial_\theta W_{\gamma,r}e^{in\theta}\right)\right]\rangle, \\ &= \rho_{m-n} + w_{m,n} + B(m,n). \end{aligned} \tag{11.21}$$

We define B by

$$B(m,n) \equiv \langle e^{im\theta}, W_{\gamma,r}\left[\partial_\theta\left(\gamma\partial_\theta W_{\gamma,r}(e^{in\theta})\right)\right]\rangle. \tag{11.22}$$

We need the operator $W_{\gamma,r}$ to act on exponentials. Let us first focus on the right hand side of the inner product, specifically the term that the first $W_{\gamma,r}$ acts on, i.e.

$$\partial_\theta\left(\gamma\partial_\theta W_{\gamma,r}(e^{in\theta})\right). \tag{11.23}$$

Define a Fourier series for $W_{\gamma,r}(e^{in\theta})$ as

$$W_{\gamma,r}(e^{in\theta}) = \sum_{l=-\infty}^{\infty} w_{l,n}e^{il\theta}, \tag{11.24}$$

where the coefficients are defined by (11.20). This allows us to differentiate with respect to θ. So the term (11.23) becomes

$$\partial_\theta \left(\gamma \partial_\theta W_{\gamma,r}(e^{in\theta})\right) = \sum_{l=-\infty}^{\infty} ilw_{l,n}\partial_\theta \left(\gamma e^{il\theta}\right). \tag{11.25}$$

In order to be able to differentiate again we define another Fourier series for γ as

$$\gamma(\theta) = \sum_{q=-\infty}^{\infty} \gamma_q e^{iq\theta}.$$

Looking back to (11.25) with this new Fourier series we have

$$\begin{aligned} \textstyle\sum_{l=-\infty}^{\infty} ilw_{l,n}\partial_\theta \left(\gamma e^{il\theta}\right) &= \textstyle\sum_{l=-\infty}^{\infty}\sum_{q=-\infty}^{\infty} ilw_{l,n}\gamma_q \partial_\theta e^{i(q+l)\theta}, \\ &= -\textstyle\sum_{l=-\infty}^{\infty}\sum_{q=-\infty}^{\infty}(q+l)\gamma_q l w_{l,n} e^{i(q+l)\theta}. \end{aligned} \tag{11.26}$$

If we substitute (11.26) into (11.22) for B, we get

$$\begin{aligned} B(m,n) &\equiv -\textstyle\sum_{l=-\infty}^{\infty}\sum_{q=-\infty}^{\infty}(q+l)\gamma_q l w_{l,n}\langle e^{im\theta}, W_{\gamma,r}e^{i(q+l)\theta}\rangle, \\ &= -\textstyle\sum_{l=-\infty}^{\infty}\sum_{q=-\infty}^{\infty} w_{m,q+l}(q+l)\gamma_q l w_{l,n}. \end{aligned} \tag{11.27}$$

Substituting $k = q + l$ in (11.27) and combining with (11.21) we get

$$r\frac{d}{dr}w_{m,n} = \rho_{m-n} - \sum_{l=-\infty}^{\infty}\sum_{k=-\infty}^{\infty} w_{m,k} l \gamma_{k-l} k w_{l,n}. \tag{11.28}$$

11.2 Numerical implementation of Layer-stripping

Given the theory developed by Somersalo et al., [75], it is straightforward to implement a numerical algorithm. We describe the algorithm in two subsections, similar to the exposition of the theory. First, we describe the method for recovering the conductivity on the boundary, then we describe how to get $w_{m,n}$ on an inner layer. This allows us to get the conductivity on this inner layer. Then with a simple difference quotient we can approximate the normal derivative of the conductivity on the boundary.

11.2.1 Outer Boundary

We can find the resistivity, $\rho = \frac{1}{\gamma}$, at the outer boundary of Ω by using the reconstruction formula of Proposition 11.1.2:

$$w_{n+k,n} = \frac{1}{|n|}\rho_k + \mathcal{O}\left(\frac{1}{n^2}\right) \tag{11.29}$$

Using both $n = N$ and $n = -N$, where N is the highest frequency of CPs, we obtain an approximation $\tilde{\rho}(1,\theta)$ for $\rho(1,\theta)$ by writing

$$\begin{aligned}\rho(1,\theta) &\approx \textstyle\sum_{k=-N}^{N} \rho_k e^{ik\theta} \\ &\approx \tfrac{N}{2}(w_{-N,-N} + w_{N,N}) + N\textstyle\sum_{k=1}^{N}\left(w_{N-k,N}e^{-ik\theta} + w_{k-N,-N}e^{ik\theta}\right) \\ &= \tilde{\rho}(1,\theta)\end{aligned} \tag{11.30}$$

11.2.2 Reconstruction inside

Assuming we take a step of size $\Delta = 1 - a_1$, where $a_1 < 1$, then we can use Euler's method on the differential equation for $w_{m,n}$, i.e.

$$\begin{aligned}w_{n,m}(1-\Delta) &\approx w_{m,n}(1) - \Delta\tfrac{d}{dr}w_{m,n}(1) \\ w_{m,n}(a_1) &\approx w_{m,n}(1) - \Delta\left(\rho_{m-n} - \textstyle\sum_{k,l=-N+1}^{N-1} w_{m,k}(1)k\gamma_{k-l}lw_{l,n}(1)\right),\end{aligned} \tag{11.31}$$

using (11.28). The updated w allows us to go back to (11.30) in order to get an approximation for $\rho(a_1,\theta)$, where N is replaced with $N-1$ and $w(1)$ have been replaced with $w(a_1)$.

There are more details to discuss. For instance, how do we calculate $w_{m,n}$ from the the current and voltage measurements. These details are discussed in Appendix B.11.

11.3 Verification

11.3.1 Simulated Verification

In this section we verify the layer-stripping method with simulated voltage data. Each test in this section assumes ideal measurements. The domain for each test is a circular tank of radius 1 with electrodes of with width $\frac{25.4}{900}2\pi$ and height $\frac{25.4}{900}2\pi$. The CPs used are TCPs and have an amplitude of 1mA. The tests are of three basic types:

- homogeneous tests,
- variable conductivities with normal derivative of zero,
- variable conductivities with non-trivial normal derivatives.

We define two types of derivatives:

Definition 11.3.1. ***Type I****: the normal derivative of the conductivity on the boundary evaluated as*

$$\left.\frac{\partial\gamma}{\partial\nu}\right|_{\partial\Omega} = \frac{\gamma(1) - \gamma(1-\Delta)}{\Delta}$$

Definition 11.3.2. ***Type II****: the normal derivative of the conductivity on the boundary evaluated as*

$$\left.\frac{\partial\gamma}{\partial\nu}\right|_{\partial\Omega} = \frac{\gamma(1-\Delta) - \gamma(1-2\Delta)}{\Delta}$$

It was found, experimentally, that **Type II** derivatives are stable and **Type I** are not. It is due to the loss of a CP when we step to an inside layer. That is, **Type II** uses CPs with a frequency up to 15, whereas **Type I** constructs $\gamma(1)$ with 16 CPs and $\gamma(1-\Delta)$ with 15 CPs.

The first tests simulate a homogeneous domain. The voltages are calculated analytically or with FEMCEM. The conductivity is set to either 1

Table 11.3.1: Errors in conductivity on $\partial\Omega$ from the layer-stripping algorithm with a homogeneous domain.

Volts	γ	mean $\gamma_{\partial\Omega}$	RE
Analytic	1	1	$6.66 \cdot 10^{-14}\%$
Analytic	423	423	$3.94 \cdot 10^{-14}\%$
FEMCEM	1	0.95	5.40%
FEMCEM	423	400.2	5.40%

Table 11.3.1: Errors in the normal derivative of the conductivity on $\partial\Omega$ from the layer-stripping algorithm with a homogeneous domain.

Tests		ave. $\frac{\partial\gamma}{\partial\nu}\Big\|_{\partial\Omega}$	Type II
Volts	γ	$\Delta = 0.01$	$\Delta = 0.001$
Analytic	1	$-2.38 \cdot 10^{-15}$	$3.98 \cdot 10^{-15}$
Analytic	423	$-1.30 \cdot 10^{-5}$	$-1.30 \cdot 10^{-5}$
FEMCEM	1	-1.86	-1.78
FEMCEM	423	-0.79	-0.75

or $423mS/m$. The choice $423mS/m$ was chosen for later comparison with ACT data on a circular tank, reconstructions on this tank are shown in [37]. In Table 11.3.1 & 11.3.1 are the results of the layer stripping algorithm on the homogeneous tank.

The remaining tests are not homogeneous. The conductivity functions with zero normal derivatives on the boundary are

$$\gamma_1(r) = \begin{cases} 4, & \text{if } r < 0.95 \\ 2, & \text{otherwise,} \end{cases}$$

$$\gamma_2(\theta) = \begin{cases} 1, & \text{if } 0 < \theta < \pi/2 \\ 2, & \text{if } \pi/2 \leq \theta < \pi \\ 3, & \text{if } \pi \leq \theta < 3\pi/2 \\ 3/2, & \text{otherwise,} \end{cases}$$

and

$$\gamma_3(r) = \left(5e^{\left(-2\frac{(t^2+r^2)}{(r+t)^2(r-t)^2} \right)} + \sqrt{a} \right)^2,$$

where $t = 0.95$ and $a = 2$. This function is described in [37]; t determines the support of the exponential and a determines the conductivity on the

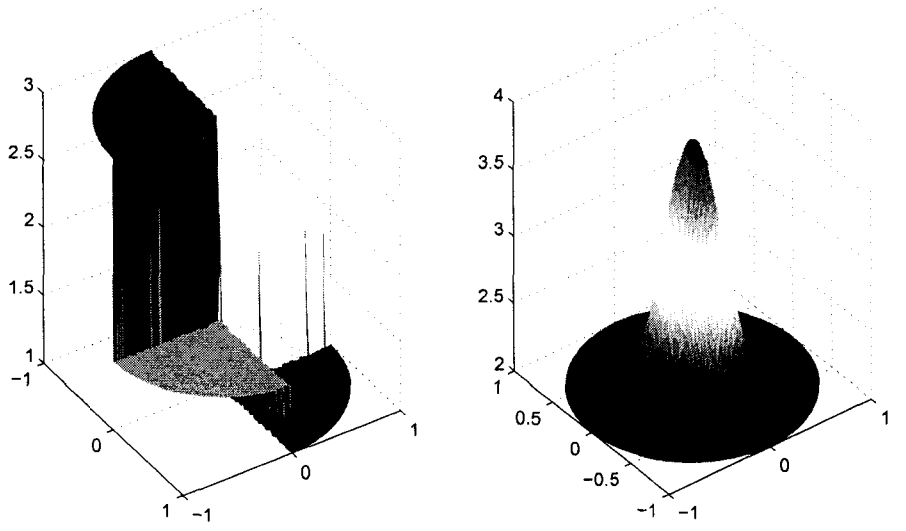

Figure 11.1: Illustrations of γ_2 and γ_3. Each have a normal derivative on the boundary of zero. The surface on the left has conductivity values of 1, 2, 3, and 1.5 in the quadrants 1 through 4, respectively.

boundary. Note that γ_1 and γ_2 violate the smoothness assumption of the layer-stripping method. The γ_2 and γ_3 are shown in Figure 11.1 and the left and right, respectively.

The last four functions have nonzero normal derivatives on the boundary. The functions we used are

$$\gamma_4(r) = 5 - 2r,$$

$$\gamma_5(r) = \left(5e^{\left(-2\frac{(t^2+r^2)}{(r+t)^2(r-t)^2}\right)} + \sqrt{a}\right)^2, \quad \text{with } t = 1.5 \text{ and a} = 2,$$

$$\gamma_6(r,\theta) = 5(1-\sqrt{r}) + rsin(3\theta) + 2,$$

$$\gamma_7(r,\theta) = 5(1-\sqrt{r}) + 2re^{\frac{sin(\theta)}{\pi}} sin(3\theta) + 5,$$

$$\gamma_8(r,\theta) = 5(1-\sqrt{r}) + rsin(\theta) + 5$$

The second function γ_5 is like the previous γ_3 except that compact support is beyond the boundary of the domain. We illustrate γ_6 and γ_7 in Figure

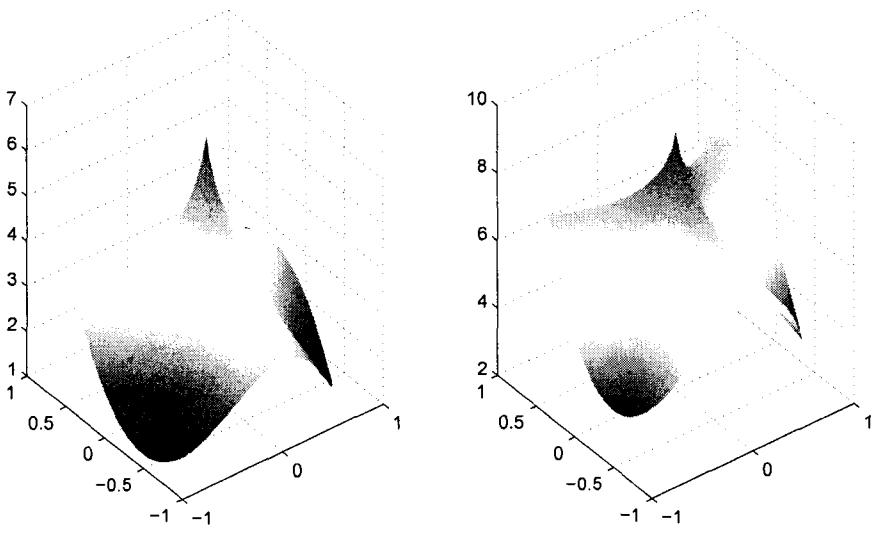

Figure 11.2: Illustrations of γ_6 and γ_7.

11.2. We present the results for the reconstructed conductivity and normal derivative in Figure 11.3 and Figure 11.4. The layer-stripping algorithm works fairly well for conductivity reconstructions on the boundary. However, the normal derivatives shown in Figure 11.4 are not good. The most troubling recoveries are the ones that should be constants, i.e. γ_1, γ_3, γ_4, and γ_5. After the implementation of the algorithm, we can only conclude that we are seeing the same instability others have seen in layer-stripping.

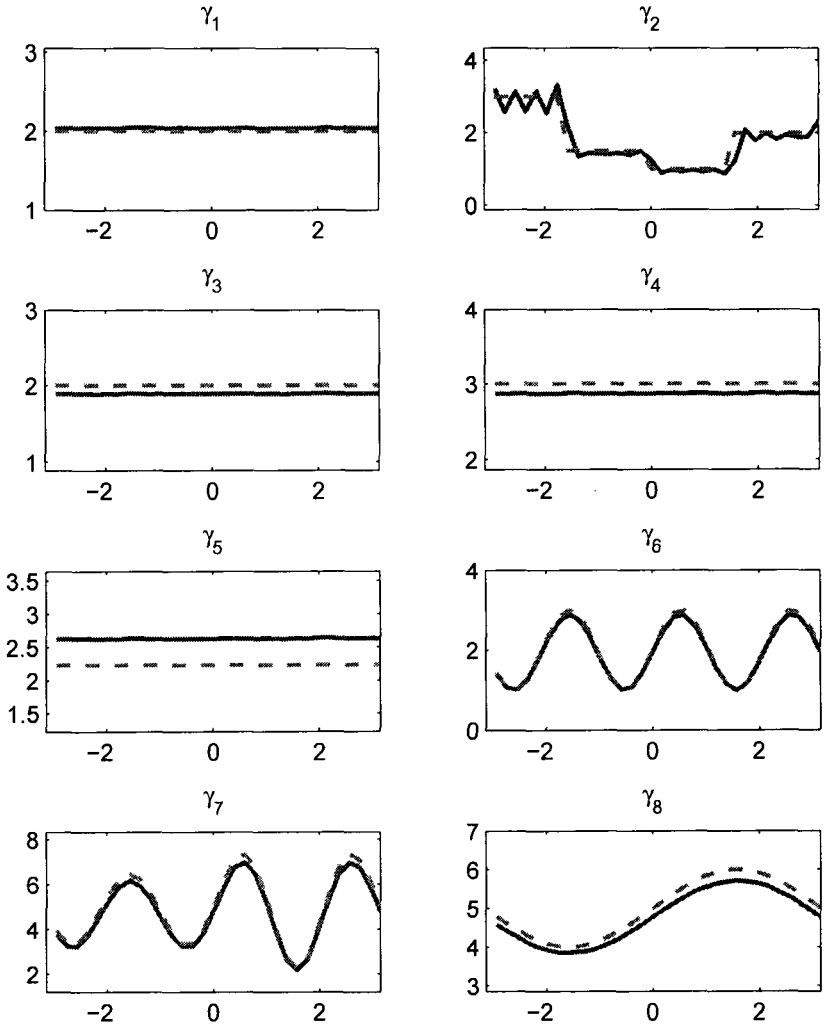

Figure 11.3: Illustrations of γ_6 and γ_7.

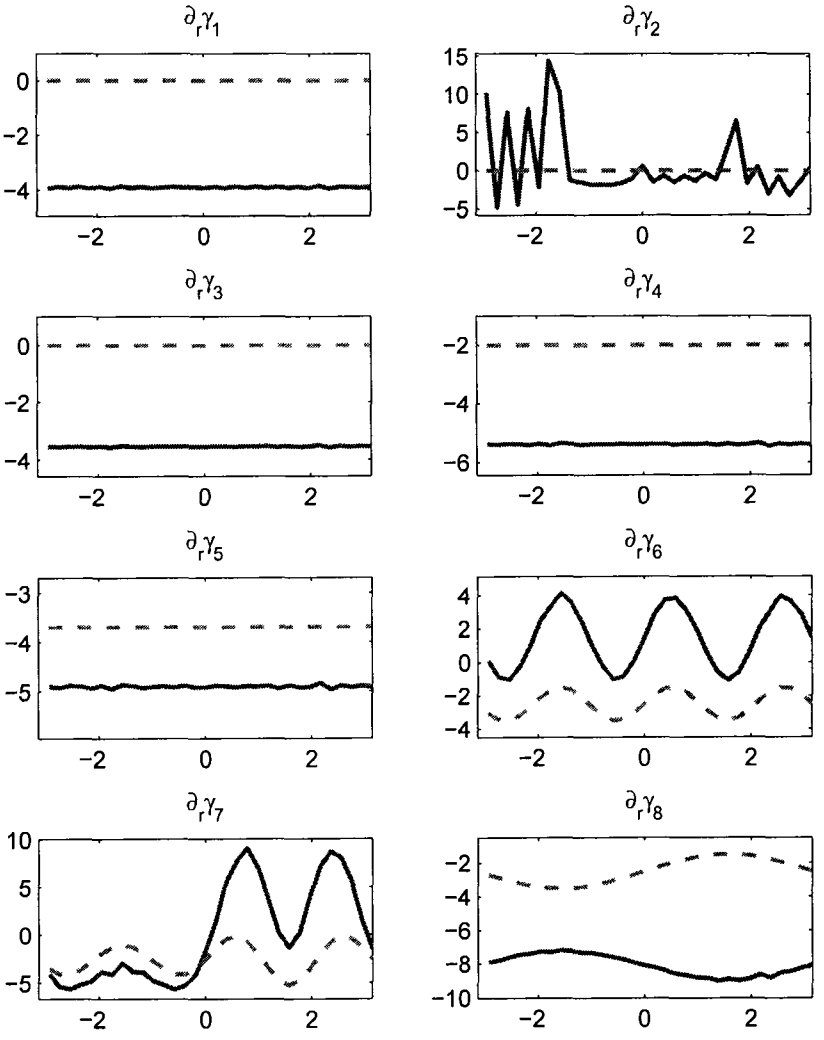

Figure 11.4: Illustrations of γ_6 and γ_7.

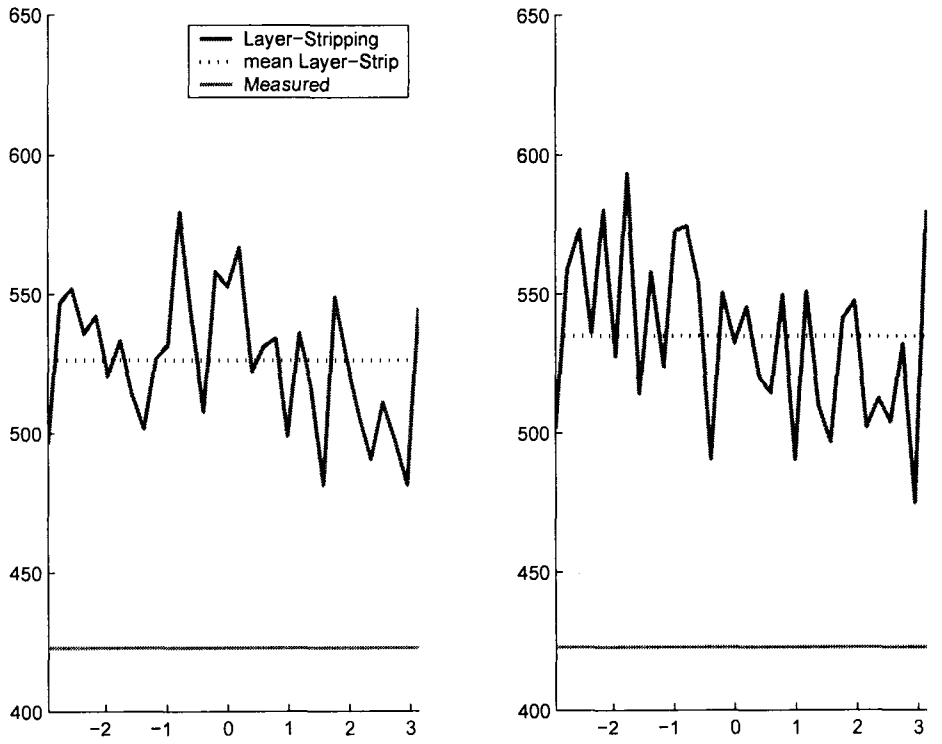

Figure 11.5: Reconstructed conductivity values on the boundary of the tank by layer-stripping. Voltages we taken from ACT3 homogeneous tank (left) and tank with agar heart and lungs (right). The measured conductivity value is 423mS/m.

11.3.2 Experimental Verification

Here we test this method on measured data from the ACT3 system on a circular domain. It is the experiment shown in [37]. We have a circular tank of radius 15cm, electrodes of size 1.6cm high by 2.5cm wide, TCPs with amplitude of 0.2mA, and a 32 electrode system. The tank is filled with saline and the measured conductivity is 424mS/m. There are two sets of measurements. The left plot in Figure 11.5 corresponds to a homogeneous tank, and on the right there is placed an agar heart and lungs in the tank. It appears that there is quite a large error between the recovery and the

measured conductivity found in Figure 11.5. We really don't know whether we expect to see some variation due to electrode effects.

11.4 Conclusions of Layer-Stripping

We see from the simulated data that the layer-stripping algorithm provides accurate conductivity reconstructions. However, when we try to validate this from measured data we do not see the same accuracy. Also the normal derivative of the reconstructed conductivities appeared to be unstable. The current implementation of the layer-stripping algorithm is not practical for reconstructing γ and $\frac{\partial\gamma}{\partial\nu}$ on the boundary. We still hope that there might be a way to regularize the solution or another way to get more stable recoveries, i.e. incorporate electrode effect. If we were able to get stable reconstructions, the generalization of the layer-stripping algorithm to general domains appears relatively straightforward. In addition, having this boundary information should allow the D-bar method to recover more accurate conductivities.

Chapter 12

CONCLUSIONS

This dissertation successfully improved the numerical implementation of the 2-D D-bar method. At this time we have published one paper that showcases some of these improvements [62]. The results of this paper are also included in Section 6.1. It illustrates the use of the finite element method with the complement electrode model and the new calculation of the scattering transform for elliptical domains. It shows clear improvement over using the scattering transform calculated on a circle and using analytic voltages.

The study on the simulated chest was a major part of this dissertation. This work included the implementation of the D-bar method with general current patterns (CPs). This is a small, but important improvement that allows the D-bar method to use data from a variety of sources. In addition to reconstructions on simulated chests with many different sets of CPs, the chest study included a thorough discussion on distinguishabilities for a variety of CPs, modeling assumptions, and the study of the effects on reconstructions from errors in data. The study of modeling assumptions has given us more insight into the importance of proper domain modeling, and the study with simulated data errors has shown us some of the limits of reconstructions using t^{exp} with the D-bar method.

Incorporating the analytic solution on a general domain and the corresponding analytic optimal CPs did not result in dramatic improvements with the D-bar method. However, this does not necessarily imply that there would not be striking improvements with other reconstruction algorithms. Nevertheless, we can conclude from our solution that trigonometric CPs are very close to optimal CPs for chest-shaped domains. Hence, the use of TCPs on chest-shaped domains is a practically choice.

Lastly, using the layer-stripping method we provided good conductivity reconstructions on the boundary for simulated data. However, the algorithm had problems with measured data and with recovering $\frac{\partial \gamma}{\partial \nu}$ on the boundary. We are hopeful that the problems can be overcome by an incorporation of FEMCEM into the method and/or regularization in the calculation of $R_{\gamma,r}$ from the Ricatti equation. Once this has been achieved we can complete the implementation of Step 1 of Nachman's method, which should further improve reconstructions.

Appendix A

FUNCTION SPACES

$\mathbf{L_p}$ spaces

It is defined as the following

$$L_p(\Omega) = \{u : \int_\Omega |u|^p < \infty\}, \forall p > 0,$$

with the following norm

$$|u|_{L_p} = (\int_\Omega |u|^p)^{\frac{1}{p}}.$$

Sobolev spaces

We define a Sobolev space as the following $W^{k,p}$ that consists of all locally summable functions $u : \Omega \to \mathbb{R}$ such that for each multiindex α with $|\alpha| \leq k, D^\alpha$ exists in the weak sense and belongs to $L^p(\Omega)$, in other words we have

$$W^{k,p}(\Omega) = \{u \in L^p : \forall |\alpha| \leq k, \partial_x^\alpha u \in L^p(\Omega)\}$$

We define the norm of $u \in W^{k,p}$ as the following,

$$||u||_{W^{k,p}}(\Omega) := \begin{cases} \left(\sum_{|\alpha|\leq k} \int_\Omega |D^\alpha u|^p dx\right)^{\frac{1}{p}} & 1 \leq p < \infty \\ \sum_{|\alpha|\leq k} ess\ sup_U |D^\alpha u| & p = \infty \end{cases}$$

Hilbert Spaces [22]

The definition of a **Hilbert space** *is a Banach space endowed with an inner*

product which generates the norm. Where a **Banach space** *is a complete, normed, linear space.*

Some examples are the following:

a. The space $H^0 = L^2(\Omega)$ is a Hilbert space, with

$$(f, g) = \int_\Omega fgdx.$$

b. The Sobolev space $H^1(\Omega)$ is a Hilbert Space, with

$$(f, g) = \int_\Omega fg + Df \cdot Dgdx.$$

c. If $p = 2$ we have $H^k(\Omega) = W^{k,2}(\Omega)$, $k = 0, 1, 2, ...$

We can define a Hilbert space more generally for $s \geq 0$, as the following

$$H^s = \{u \in L^2 : (1 + |z|^2)^{\frac{s}{2}} \hat{u}(z) \in L^2\},$$

where $\hat{u}(z)$ is the Fourier Transform of u, with a norm

$$||u||_s^2 = \int_\Omega (1 + |z|^2)^s \hat{u}(z)dz,$$

and

$$(u, v)_s = \int_\Omega (1 + |z|^2)^s \hat{u}(z)\hat{v}(z)dz.$$

Appendix B

SHORT CALCULATIONS

B.1 Converting Δ to general domain shape coordinates coordinates

First, recall the coordinates defined by (3.3), i.e.

$$\begin{aligned} x &= \eta r(\theta) cos(\theta), \\ y &= \eta r(\theta) sin(\theta). \end{aligned}$$

We use a standard approach to change the coordinates [56]. We need scaling factors

$$h_\eta = \left| \left(\frac{\partial x}{\partial \eta}, \frac{\partial y}{\partial \eta} \right) \right| = \sqrt{(r^2(\theta) cos^2(\theta) + r^2(\theta) sin^2(\theta))} = r$$

and

$$\begin{aligned} h_\theta &= \left| \left(\tfrac{\partial x}{\partial \theta}, \tfrac{\partial y}{\partial \theta} \right) \right| \\ &= \left[(\eta r'(\theta) cos(\theta) - \eta r(\theta) sin(\theta))^2 + (\eta r'(\theta) sin(\theta) + \eta r(\theta) cos(\theta))^2 \right]^{\frac{1}{2}} \\ &= \eta \sqrt{(r')^2 + r^2 - 2rr' cos(\theta) sin(\theta) + 2rr' sin(\theta) cos(\theta)} \\ &= \eta \sqrt{(r')^2 + r^2}. \end{aligned}$$

Therefore our ∇u has the form

$$\begin{aligned} \nabla u &= \tfrac{1}{h_\eta} u_\eta \hat{e}_\eta + \tfrac{1}{h_\theta} u_\theta \hat{e}_\theta \\ &= \tfrac{1}{r} u_\eta \hat{e}_\eta + \tfrac{1}{\eta \sqrt{(r')^2 + r^2}} u_\theta \hat{e}_\theta \end{aligned} \tag{B.1}$$

Then to completely find the Laplace we use the formula

$$\nabla \cdot [v_1 \ v_2] = \frac{1}{h_\eta h_\theta}\left[\frac{\partial}{\partial \eta}(v_1 h_\theta) + \frac{\partial}{\partial \theta}(v_2 h_\eta)\right].$$

If we simplify notation by defining

$$p(\theta) = \frac{\sqrt{(r')^2 + r^2}}{r} \tag{B.2}$$

we get

$$\nabla \cdot \nabla u = \frac{1}{r\eta\sqrt{(r')^2 + r^2}}\left[p(\theta)\frac{\partial}{\partial \eta}(\eta u_\eta) + \frac{1}{\eta}\frac{\partial}{\partial \theta}\left(\frac{1}{p(\theta)}u_\theta\right)\right] \tag{B.3}$$

Since in our case the Laplace is equal to zero we can eliminate common factors. Now, we have

$$\nabla \cdot \nabla u = p\frac{\partial}{\partial \eta}(\eta u_\eta) + \frac{1}{\eta}\frac{\partial}{\partial \theta}\left(\frac{1}{p}u_\theta\right) = 0$$

B.2 Find the constants for the inhomogeneous domain

If we look at (3.17) we see we need

$$-\gamma_1 \alpha n \sum_{n=0}^{\infty} D_n \eta^{\alpha n} g(\theta) = -\alpha \sum_{n=0}^{\infty} \left(nE_n\eta^{\alpha n} - nH_n\eta^{-\alpha n}\right) g(\theta)$$

If we look at all of our boundary conditions we have,

$$\begin{aligned}
\gamma_1 D_n \eta_1^{\alpha n} &= E_n\eta_1^{\alpha n} - H_n\eta_1^{-\alpha n}, \quad \text{from (3.17)},\\
D_n\eta_1^{\alpha n} &= E_n\eta_1^{\alpha n} + H_n\eta_1^{-\alpha n}, \quad \text{from (3.16)},\\
\tfrac{1}{A}T_n &= \alpha n(E_n - H_n), \qquad \text{from (3.2)}.
\end{aligned}$$

We can solve this simple system of linear equations for D_n, E_n, and H_n. We get

$$\begin{aligned}
D_n &= \frac{\eta_1^{-\alpha n}((\gamma_1-1)-(1+\gamma_1))\frac{1}{A\alpha n}T_n}{(1-\gamma_1)\eta_1^{\alpha n}-(1+\gamma_1)\eta_1^{-\alpha n}}\\
E_n &= \frac{-(1+\gamma_1)\eta_1^{-\alpha n}\frac{1}{A\alpha n}T_n}{(1-\gamma_1)\eta_1^{\alpha n}-(1+\gamma_1)\eta_1^{-\alpha n}} \qquad \text{(B.4)}\\
H_n &= \frac{(\gamma_1-1)\frac{1}{A\alpha n}T_n\eta_1^{\alpha n}}{(1-\gamma_1)\eta_1^{\alpha n}-(1+\gamma_1)\eta_1^{-\alpha n}}
\end{aligned}$$

Finally, we have our solution if we plug our expressions for A_n, B_n, and C_n into (3.18) and (3.19).

B.3 Conductivity to the Schrödinger equation

We begin with the Schrödinger equation

$$(-\Delta + q)\widetilde{u} = 0 \tag{B.5}$$

and substitute the following equations, $q = \gamma^{-\frac{1}{2}}\Delta(\gamma^{\frac{1}{2}})$ and $\widetilde{u} = \gamma^{\frac{1}{2}}u$, into the Schrödinger equation to transform to the conductivity equation,

$$\nabla \cdot (\gamma \nabla u) = 0 \tag{B.6}$$

We begin by substituting to get

$$(-\Delta + q)\widetilde{u} = (-\Delta + \gamma^{-\frac{1}{2}}\Delta(\gamma^{\frac{1}{2}}))\gamma^{\frac{1}{2}}u = 0.$$

Expanding this we have

$$-\Delta\gamma^{\frac{1}{2}}u + \gamma^{-\frac{1}{2}}\Delta(\gamma^{\frac{1}{2}})\gamma^{\frac{1}{2}}u = -\Delta\gamma^{\frac{1}{2}}u + \Delta(\gamma^{\frac{1}{2}})u = 0.$$

We can expand the Laplacian operator

$$-\nabla \cdot (\gamma^{\frac{1}{2}}\nabla u + u\nabla\gamma^{\frac{1}{2}}) + \Delta(\gamma^{\frac{1}{2}})u = 0.$$

Expanding further we have

$$-\nabla\gamma^{\frac{1}{2}} \cdot \nabla u - \gamma^{\frac{1}{2}}\nabla \cdot \nabla u - \nabla u \cdot \nabla\gamma^{\frac{1}{2}} - u\nabla \cdot \nabla\gamma^{\frac{1}{2}} + \Delta(\gamma^{\frac{1}{2}})u = 0.$$

The last two terms on the right cancel out, we can combine two of the three remaining terms, and we are left with

$$-2\nabla(\gamma^{\frac{1}{2}}\nabla u) - \gamma^{\frac{1}{2}}\nabla \cdot \nabla u = 0.$$

Let's multiply the equation by $\gamma^{\frac{1}{2}}$ to get

$$-2\gamma^{\frac{1}{2}}\nabla(\gamma^{\frac{1}{2}}\nabla u) - \gamma\Delta u = 0. \tag{B.7}$$

One can notice that if we expand the conductivity problem we have

$$\nabla \cdot (\gamma \nabla u) = \nabla \gamma \cdot \nabla u + \gamma \Delta u = 0 \tag{B.8}$$

This looks close to what we have above in (B.7). We can rewrite the first term of the expanded conductivity problem (B.8) as the following

$$\nabla \gamma \cdot \nabla u = \nabla (\gamma^{\frac{1}{2}} \gamma^{\frac{1}{2}}) \cdot \nabla u = 2\gamma^{\frac{1}{2}} \nabla \gamma^{\frac{1}{2}} \cdot \nabla u \tag{B.9}$$

If we plug (B.9) into (B.7) we have

$$-\nabla \gamma \cdot \nabla u - \gamma \Delta u = 0.$$

This is clearly the expanded version of the conductivity equation (B.8) which completes the derivation linking the Schrödinger equation to the conductivity equation.

B.4 Understanding Λ_q and Λ_γ relation

The relationship between Λ_q and Λ_γ given in [64] is

$$\Lambda_q = \gamma^{-\frac{1}{2}} \left(\Lambda_\gamma + \frac{1}{2} \frac{\partial \gamma}{\partial \nu} \right) \gamma^{-\frac{1}{2}}. \tag{B.10}$$

One can verify this expression by a simple calculation. If we apply Λ_q to ψ then we expect to get

$$\Lambda_q \psi = \left. \frac{\partial \psi}{\partial \nu} \right|_{\partial \Omega}. \tag{B.11}$$

So let us apply $\psi = \gamma^{\frac{1}{2}} u$ to (B.10), we get

$$\begin{aligned}
\Lambda_q(\gamma^{\frac{1}{2}} u) &= \gamma^{-\frac{1}{2}} \left(\Lambda_\gamma + \tfrac{1}{2}\tfrac{\partial \gamma}{\partial \nu}\right) \gamma^{-\frac{1}{2}} (\gamma^{\frac{1}{2}} u) \\
&= \gamma^{-\frac{1}{2}} \Lambda_\gamma u + \tfrac{1}{2}\gamma^{-\frac{1}{2}} \tfrac{\partial \gamma}{\partial \nu} u \\
&= \gamma^{-\frac{1}{2}} \gamma \tfrac{\partial u}{\partial \nu} + \tfrac{1}{2}\gamma^{-\frac{1}{2}} \tfrac{\partial \gamma}{\partial \nu} u \\
&= \gamma^{\frac{1}{2}} \tfrac{\partial u}{\partial \nu} + \tfrac{1}{2}\gamma^{-\frac{1}{2}} \tfrac{\partial \gamma}{\partial \nu} u \\
&= \tfrac{\partial (\gamma^{\frac{1}{2}} u)}{\partial \nu} \\
&= \tfrac{\partial \psi}{\partial \nu}
\end{aligned}$$

B.5 Short discussion on Alessandrini's identity

Alessandrini's identity is

$$\langle u_0, (\Lambda_q - \Lambda_0) u \rangle = \int_\Omega q u u_0 dx \tag{B.12}$$

We show a calculation of it, its connection to the scattering transform, and its connection to the equation (4.15).

B.5.1 Verifying Alessandrini's identity

As a good exercise we include the derivation/calculation of Alessandrini's identity. Let's assume we are given u_0 and u that satisfy

$$\Delta u_0 = 0, \tag{B.13}$$

$$-\Delta u + qu = 0, \tag{B.14}$$

respectively. Now, let's multiply (B.13) by u, (B.14) by u_0, add, and integrate. We get

$$\int_\Omega u \Delta u_0 - u_0 \Delta u + q u u_0 dx = 0.$$

Let's integrate by parts and simplify

$$\begin{aligned} \int_{\partial\Omega} u\frac{\partial u_0}{\partial \nu} - u_0\frac{\partial u}{\partial \nu} ds + \int_\Omega \left[-(\nabla u \cdot \nabla u_0) + (\nabla u_0 \cdot \nabla u) + quu_0\right] dx &= 0, \\ \int_{\partial\Omega} (u\Lambda_0 u_0 - u_0\Lambda_q u)\, ds + \int_\Omega quu_0 dx &= 0, \end{aligned} \tag{B.15}$$

using the definition of the Dirichlet-to-Neumann map. If we were to redo the above calculation with $q = 0$ we would obtain

$$\int_{\partial\Omega} (u\Lambda_0 u_0 - u_0\Lambda_0 u)\, ds = 0. \tag{B.16}$$

If we subtract (B.15) from (B.16) we get

$$\begin{aligned} \int_{\partial\Omega} (u_0\Lambda_q u - u\Lambda_0 u_0)\, ds - \int_{\partial\Omega} (u\Lambda_0 u_0 - u_0\Lambda_0 u)\, ds &= \int_\Omega quu_0 dx, \\ \int_{\partial\Omega} (u_0\Lambda_q u - u_0\Lambda_0 u)\, ds &= \int_\Omega quu_0 dx. \end{aligned} \tag{B.17}$$

Clearly, giving us (B.12).

B.5.2 Scattering Transform

Alessandrini's identity connects, in our case, two forms of the scattering transform. One is how it is defined (4.7), i.e.

$$t(k) \equiv \int_{\mathbb{R}^2} e_k(x)\mu(x,k)q(x)dx, \quad k \in \mathbb{C}\backslash 0,$$

the other the equation we use to compute it (4.16), i.e.

$$t(k) = \int_{\partial\Omega} e^{i\bar{k}\bar{x}}(\Lambda_q - \Lambda_0)\psi(\cdot,k)d\sigma.$$

One can clearly see if plug in $e^{i\bar{k}\bar{x}}$ for u_0 and $\psi(x,k)$ for u into (B.12) then we have the connection.

B.5.3 Discussion on (4.15)

Recall the equation (4.15) for calculating ψ on the boundary

$$\psi(\cdot,k)|_{\partial\Omega} = e^{ikx} - S_k(\Lambda_q - \Lambda_0)\psi(\cdot,k).$$

If we choose $u = \psi$, $u_0 = G_k(x-y)$, and plug into (B.12). We get

$$\begin{aligned}\langle G_k(x-y), (\Lambda_q - \Lambda_0)\psi\rangle &= \int_\Omega q\psi G_k(x-y)dx \\ &= G_k * (q\psi)\end{aligned}$$

Using the Lippmann-Schwinger equation, i.e.

$$\psi = e^{ikx} - G_k * (q\psi)$$

we get

$$\begin{aligned}e^{ikx} - \psi &= \langle G_k(x-y), (\Lambda_q - \Lambda_0)\psi\rangle \\ \psi(x,k) &= e^{ikx} - \int_{\partial\Omega} \left(G_k(x-y), (\Lambda_q - \Lambda_0)\psi(y,k)\right) ds(y)\end{aligned}$$

B.6 Discussion on the easy end of the D-bar method

We state that all we need to do to finish the D-bar method is to take the limit in (4.20), i.e.

$$\lim_{k\to 0} \mu(x,k) = \gamma^{\frac{1}{2}}(x).$$

Let's review what we do know. We know the relation between μ and ψ by (4.3), i.e.

$$\mu(x,k) \equiv e^{-ikx}\psi(x,k).$$

Thus if we take the limit as k goes to zero in (4.3) we get

$$\lim_{k\to 0} \mu(x,k) = \psi(x,0).$$

This is not the conductivity we want, but it is the solution of the Schrödinger equation. The trick is that $\sqrt{\gamma}$ satisfies the Schrödinger equation, as can be seen below

$$\begin{aligned}(-\Delta + q)\sqrt{\gamma} &= 0 \\ -\Delta\sqrt{\gamma} + \frac{\Delta\sqrt{\gamma}}{\sqrt{\gamma}}\sqrt{\gamma} &= 0 \\ -\Delta\sqrt{\gamma} + \Delta\sqrt{\gamma} &= 0.\end{aligned}$$

The solution to the Schrödinger equation is unique under the class of considered solutions. Thus the limit indeed gives us the conductivity.

B.7 Scaling of Λ operator

In this section we scale the domain by a certain factor b and find the effect on the operator Λ_γ. Let us start by assuming that were are on a scaled domain $\tilde{\Omega}$. We thus have

$$t_{sc}^{exp}(k) = \int_{\partial\tilde{\Omega}} e^{i\bar{k}\bar{z}}(\tilde{\Lambda}_\gamma - \tilde{\Lambda}_1)e^{ikz}d\sigma(z). \tag{B.18}$$

where

$$\partial\tilde{\Omega} = \{r(\theta), \quad 0 \leq \theta \leq 2\pi\}.$$

Note that we are assuming that

$$\partial\Omega = \{R(\theta) = b \cdot r(\theta), \quad 0 \leq \theta \leq 2\pi\}.$$

It is fine to work with this boundary, except we need to scale our operators Λ_γ and Λ_1 properly in order to use measured data from the unscaled experiment. We can use the relation $\tilde{\Lambda}_\gamma = b\Lambda_\gamma$, the relation is shown by the following argument:

$$\langle \Lambda_\gamma f^1, f^2 \rangle_{\partial\Omega} \equiv \int_\Omega \gamma \nabla u^1 \cdot \nabla u^2 dx$$

Applying integration by parts we have

$$\langle \Lambda_\gamma f^1, f^2 \rangle_{\partial\Omega} = -\int_\Omega u^2 \nabla \cdot (\gamma \nabla u^1) dx + \int_{\partial\Omega} \gamma u^2 \frac{\partial u^1}{\partial \nu} d\sigma.$$

The first piece contributes zero because we can assume u^1 satisfies (1.1). Note that $d\sigma = \sqrt{R^2(\theta) + (R'(\theta))^2}$ and $d\tilde{\sigma}$ is derived from $d\sigma$ and shown below

$$\frac{d\sigma}{b} = \sqrt{\frac{R^2(\theta)}{b^2} + \frac{(R'(\theta))^2}{b^2}} = \sqrt{r^2(\theta) + (r'(\theta))^2} = d\tilde{\sigma}.$$

We therefore have

$$\begin{aligned} \langle \Lambda_\gamma f^1, f^2 \rangle_{\partial\Omega} &= b \int_0^{2\pi} \gamma u^2 \tfrac{\partial u^1}{\partial \nu} \tfrac{d\sigma}{b} \\ &= b \int_0^{2\pi} \gamma u^2 \tfrac{\partial u^1}{\partial \nu} d\tilde{\sigma} \\ &= \langle b \Lambda_\gamma f^1, f^2 \rangle_{\partial\tilde{\Omega}} = \langle \tilde{\Lambda}_\gamma f^1, f^2 \rangle_{\partial\tilde{\Omega}}. \end{aligned}$$

Summarizing this result we have

$$t_{sc}^{exp}(k) = b \int_{\partial\tilde{\Omega}} e^{i\bar{k}\bar{z}} (\Lambda_\gamma - \Lambda_1) e^{ikz} d\sigma(z). \tag{B.19}$$

B.8 Calculation of $L_\gamma(m,n)$

In order to calculate $L_\gamma(m,n)$ we first look at the definition (5.10)

$$L_\gamma(m,n) \equiv \left(\phi^m, \left(\frac{R_\gamma}{A} \right)^{-1} \phi^n \right)_L. \tag{B.20}$$

We can also express R_γ^M as an inner product by inverting (B.20), i.e.

$$\begin{aligned} R_\gamma^M &= \left[\left(\phi^m, \left(\tfrac{R_\gamma}{A} \right)^{-1} \phi^n \right)_L \right]^{-1} \\ &\equiv \left(\phi^m, \left(\tfrac{R_\gamma}{A} \right) \phi^n \right)_L \end{aligned}$$

Assuming we are given a set of CPs, T, and measured voltages, V, both of size $L \times L-1$ then R_γ^M is written as

$$R_\gamma^M = T_m^T V_n,$$

where T_m and V_n are the m^{th} and n^{th} columns, respectively, of the corresponding matrices. Thus our matrix representation of the voltage-to-current map L_γ is the following

$$L_\gamma \equiv \left(T^T V\right)^{-1}. \tag{B.21}$$

B.9 Deriving the Formula for $\delta L_{m,n}$

In this section we conclude the calculation of the scattering transform t^{exp}. In this section we conclude the calculation of the scattering transform t^{exp}. We have from (5.4),(5.5), and (5.17)

$$\begin{aligned} t_{sc}^{exp}(k) &\approx \tfrac{b\Delta\theta}{A\gamma_b} \textstyle\sum_{m=0}^{\infty}\sum_{n=0}^{\infty} a_m(\bar{k})a_n(k)(s(\cdot)r^m(\cdot)e^{im\theta}, \left[\left(\tfrac{R_\gamma}{A}\right)^{-1} \right. \\ &\quad \left. - \left(\tfrac{R_1}{A}\right)^{-1}\right](r^n(\cdot)e^{in\cdot}))_L \\ &= \tfrac{b\Delta\theta}{A\gamma_b} \textstyle\sum_{m=0}^{\infty}\sum_{n=0}^{\infty} a_m(\bar{k})a_n(k)\left((s(\cdot)r^m cos(m\cdot), dR(r^n cos(n\cdot)))_L\right. \\ &\quad +i(s(\cdot)r^m(\cdot)cos(m\cdot), dR(r^n(\cdot)sin(n\cdot)))_L \\ &\quad -i(s(\cdot)r^m(\cdot)sin(m\cdot), dR(r^n(\cdot)cos(n\cdot)))_L \\ &\quad \left.+(s(\cdot)r^m(\cdot)sin(m\cdot), dR(r^n(\cdot)sin(n\cdot)))_L\right), \end{aligned}$$

where $dR = \left[\left(\tfrac{R_\gamma}{A}\right)^{-1} - \left(\tfrac{R_1}{A}\right)^{-1}\right]$.

Let's divide this derivation into pieces, first let's look at

$$\begin{aligned} &\tfrac{b\Delta\theta}{A}\textstyle\sum_{m=0}^{\infty}\sum_{n=0}^{\infty} a_m(\bar{k})a_n(k)\left(s(\cdot)r^m(\cdot)cos(m\cdot), \left[\left(\tfrac{R_\gamma}{A}\right)^{-1} \right.\right. \\ &\quad \left.\left. - \left(\tfrac{R_1}{A}\right)^{-1}\right](r^n(\cdot)cos(n\cdot))\right)_L \approx \tfrac{b\Delta\theta}{A}\textstyle\sum_{m=1}^{\frac{L}{2}}\sum_{n=1}^{\frac{L}{2}} a_m(\bar{k})a_n(k)\delta L_{m,n} \\ &= \frac{b\Delta\theta}{A}\left(\sum_{m=1}^{\frac{L}{2}-1}\sum_{n=1}^{\frac{L}{2}-1} a_m(\bar{k})a_n(k)\delta L_{m,n} + a_{\frac{L}{2}}(\bar{k})a_{\frac{L}{2}}(k)\delta L_{\frac{L}{2},\frac{L}{2}}\right. \\ &\quad \left. + \sum_{n=1}^{\frac{L}{2}-1} a_{\frac{L}{2}}(\bar{k})a_n(k)\delta L_{\frac{L}{2},n} + \sum_{m=1}^{\frac{L}{2}-1} a_m(\bar{k})a_{\frac{L}{2}}(k)\delta L_{m,\frac{L}{2}}\right). \end{aligned}$$

Ok, now let's look at the second term in the sum, we need to focus on the sine term in this term

$$\sum_{k=\frac{L}{2}+1}^{L-1} T^k = \sum_{k=\frac{L}{2}+1}^{L-1} Msin\left(\left(k-\frac{L}{2}\right)\theta\right).$$

Let $\tilde{k} = k - \frac{L}{2}$, so $\tilde{k} = 1...\frac{L}{2} - 1$, which gives us that

$$\sum_{k=\frac{L}{2}+1}^{L-1} T^k = \sum_{\tilde{k}=1}^{\frac{L}{2}-1} Msin(\tilde{k}\theta) = \sum_{\tilde{k}=1}^{\frac{L}{2}-1} T^{\tilde{k}}.$$

So for the second term we have

$$\frac{b\Delta\theta}{A\gamma_b}\sum_{m=0}^{\infty}\sum_{n=0}^{\infty} a_m(\bar{k})a_n(k)i\left(s(\cdot)r^m(\cdot)cos(m\cdot), \left[\left(\frac{R_\gamma}{A}\right)^{-1}\right.\right.$$

$$\left.\left. - \left(\frac{R_1}{A}\right)^{-1}\right](r^n(\cdot)sin(n\cdot))\right)_L \approx \frac{b\Delta\theta}{A\gamma_b}\sum_{m=1}^{\frac{L}{2}}\sum_{n=1}^{\frac{L}{2}} a_m(\bar{k})a_n(k)i\delta L_{(m,n+\frac{L}{2})}.$$

Simplifying this further we have

$$= \frac{b\Delta\theta}{A\gamma_b}\sum_{m=1}^{\frac{L}{2}-1}\sum_{n=1}^{\frac{L}{2}-1} a_m(\bar{k})a_n(k)i\delta L_{m,n+\frac{L}{2}} + \frac{\Delta\theta}{A\gamma_b}\sum_{n=1}^{\frac{L}{2}-1} a_{\frac{L}{2}}(\bar{k})a_n(k)i\delta L_{\frac{L}{2},n+\frac{L}{2}}$$

$$= \frac{b\Delta\theta}{A\gamma_b}\left(\sum_{m=1}^{\frac{L}{2}-1}\sum_{n=1}^{\frac{L}{2}-1} a_m(\bar{k})a_n(k)i\delta L_{m,n+\frac{L}{2}} + i\sum_{n=1}^{\frac{L}{2}-1} a_{\frac{L}{2}}(\bar{k})a_n(k)\delta L_{\frac{L}{2},n+\frac{L}{2}}\right).$$

Next, we have the third term. We can see that this is very similar to the second term

$$-\frac{b\Delta\theta}{A\gamma_b}\sum_{m=0}^{\infty}\sum_{n=0}^{\infty} a_m(\bar{k})a_n(k)i\left(sin(m\cdot), \left[\left(\frac{R_\gamma}{A}\right)^{-1} - \left(\frac{R_1}{A}\right)^{-1}\right](cos(n\cdot))\right)_L$$

$$\approx -\frac{b\Delta\theta}{A\gamma_b}\sum_{m=1}^{\frac{L}{2}}\sum_{n=1}^{\frac{L}{2}} a_m(\bar{k})a_n(k)i\delta L_{(m+\frac{L}{2},n)}.$$

Simplifying this further we have

$$= -\frac{b\Delta\theta}{A\gamma_b}\sum_{m=1}^{\frac{L}{2}-1}\sum_{n=1}^{\frac{L}{2}-1} a_m(\bar{k})a_n(k)i\delta L_{m+\frac{L}{2},n} - \frac{\Delta\theta}{A}\sum_{m=1}^{\frac{L}{2}-1} a_m(\bar{k})a_{\frac{L}{2}}(k)i\delta L_{m+\frac{L}{2},\frac{L}{2}},$$

$$= -\frac{b\Delta\theta}{A\gamma_b}\left(\sum_{m=1}^{\frac{L}{2}-1}\sum_{n=1}^{\frac{L}{2}-1} a_m(\bar{k})a_n(k)i\delta L_{m+\frac{L}{2},n} - i\sum_{m=1}^{\frac{L}{2}-1} a_m(\bar{k})a_{\frac{L}{2}}(k)\delta L_{m+\frac{L}{2},\frac{L}{2}}\right).$$

The last term that we are worried about is

$$\frac{b\Delta\theta}{A\gamma_b}\sum_{m=0}^{\infty}\sum_{n=0}^{\infty} a_m(\bar{k})a_n(k)\left(sin(m\cdot), \left[\left(\frac{R_\gamma}{A}\right)^{-1} - \left(\frac{R_1}{A}\right)^{-1}\right](sin(n\cdot))\right)_L$$

$$\approx \frac{b\Delta\theta}{A\gamma_b}\sum_{m=1}^{\frac{L}{2}}\sum_{n=1}^{\frac{L}{2}} a_m(\bar{k})a_n(k)\delta L_{m+\frac{L}{2},n+\frac{L}{2}}.$$

Simplifying this further we have

$$= \frac{b\Delta\theta}{A\gamma_b}\sum_{m=1}^{\frac{L}{2}-1}\sum_{n=1}^{\frac{L}{2}-1} a_m(\bar{k})a_n(k)\delta L_{m+\frac{L}{2},n+\frac{L}{2}}.$$

Now let's put all four terms together

$$t_{sc}^{exp}(k) = \frac{b\Delta\theta}{A\gamma_b}\left(\sum_{m=1}^{\frac{L}{2}-1}\sum_{n=1}^{\frac{L}{2}-1} a_m(\bar{k})a_n(k)\left(\delta L_{m,n} + \delta L_{m+\frac{L}{2},n+\frac{L}{2}}\right.\right.$$

$$\left. + i\left(\delta L_{m,n+\frac{L}{2}} - \delta L_{m+\frac{L}{2},n}\right)\right) + \sum_{n=1}^{\frac{L}{2}-1} a_{\frac{L}{2}}(\bar{k})a_n(k)\left(\delta L_{\frac{L}{2},n} + i\delta L_{\frac{L}{2},n+\frac{L}{2}}\right)$$

$$\left. + \sum_{m=1}^{\frac{L}{2}-1} a_m(\bar{k})a_{\frac{L}{2}}(k)\left(\delta L_{m,\frac{L}{2}} - i\delta L_{m+\frac{L}{2},\frac{L}{2}}\right) + a_{\frac{L}{2}}(\bar{k})a_{\frac{L}{2}}(k)\delta L_{\frac{L}{2},\frac{L}{2}}\right).$$

Let us now summarize what we have found. We have found a computable form of t^{exp} defined as (5.18), although we are in fact computing a scaled version, t_{sc}^{exp}. Thus we have a numerical solution of (4.16) and it is now possible to compute the solution of the D-bar equation, (4.18). Since we compute a scaled scattering transform we need only reconstruct the D-bar equation on that corresponding domain.

B.10 Construction of NOCP3

This section discusses the third method of finding the NOCPs discussed in [86]. In this method we get around the computationally expensive task of inverting the matrix A from (3.34). This is done by constructing a Hadamard matrix of size $L \times L$, orthogonalizing it, and computing the following

$$\begin{aligned} V(\gamma_{test}) - V(\gamma_0) &= \mathbf{L}T, \\ (V(\gamma_{test}) - V(\gamma_0))\,T^T &= \mathbf{L}TT^T, \\ (V(\gamma_{test}) - V(\gamma_0))\,T^T &= \mathbf{L}, \end{aligned} \tag{B.22}$$

where T is the matrix of CPs. This gives an approximation of $\mathbf{L}$. We get our set of NOCP3s by MATLAB's *eig* command on the matrix (B.22). The choice of CPs does effect the quality of constructed NOCPs. However, we chose the Hadamard matrix because it provided empirically good results.

B.11 Some details of the Layer-stripping algorithm

B.11.1 Computation of $w_{m,n}$

Let's discuss the details of computing $w_{m,n}$. We begin with (11.20), which is

$$w_{m,n}(r) = \frac{1}{2\pi}\int_{-\pi}^{\pi} e^{-im\theta}\frac{1}{r}R_{\gamma,r}(e^{in\cdot})(\theta)d\theta.$$

Recall, that if we have data on a circle of radius r then we have the relation

$$\frac{1}{r}R_{\gamma,r} = R_{\gamma,1} = R_\gamma.$$

Thus, $w_{m,n}(r)$ is equivalent to $w_{m,n}(1)$. We want to discretize the integral (11.20) by a finite sum. We write it as an inner product

$$w_{m,n}(1) \approx \frac{1}{2\pi r}\sum_{l=1}^{L} e^{-im\theta_l}R_{\gamma,r}(e^{in\cdot})(\theta_l)\Delta\theta = \frac{1}{Lr}\left(e^{im\cdot}, R_{\gamma,r}(e^{in\cdot})\right)_L \tag{B.23}$$

where $\Delta\theta = \frac{2\pi}{L}$ and the inner product is defined

$$(f,g) = \sum_{l=1}^{L} \overline{f(\theta_l)} g(\theta_l).$$

Next by using Euler's formula, $e^{ix} = cos(x) + isin(x)$ we have

$$\begin{aligned}(e^{im\cdot}, R_{\gamma,r}(e^{in\cdot}))_L = & \ (cos(m\cdot) + isin(m\cdot), R_{\gamma,r}(cos(n\cdot) + isin(n\cdot)))_L \\ = & \ (cos(m\cdot), R_{\gamma,r}cos(n\cdot))_L + i\,(cos(m\cdot), R_{\gamma,r}sin(n\cdot)))_L \\ & -i\,(sin(m\cdot), R_{\gamma,r}cos(n\cdot))_L + (sin(m\cdot), R_{\gamma,r}sin(n\cdot))_L\end{aligned} \tag{B.24}$$

Since, we want to apply CPs to $R_{\gamma,r}$ we recall our TCPs,

$$T_l^k = \begin{cases} Mcos(k\theta_l), & k = 1, ..., \frac{L}{2} \\ Msin((k - \frac{L}{2})\theta_l), & k = \frac{L}{2} + 1, ..., L - 1, \end{cases} \tag{B.25}$$

where $\theta_l = \frac{2\pi l}{L}$. In order to get the TCPs into the formulation, we use the gap model by dividing by A, the area of an electrode, and get

$$\begin{aligned}(cos(m\cdot), R_{\gamma,r}cos(n\cdot))_L &= A\left(\frac{T^m}{M}, \left(\frac{R_{\gamma,r}}{A}\right)\frac{T^n}{M}\right)_L \\ &= \frac{A}{M^2}\left(T^m, \left(\frac{R_{\gamma,r}}{A}\right)T^n\right)_L \equiv \tilde{R}_r^M(m,n).\end{aligned} \tag{B.26}$$

If we combine (B.26) and (B.24) we get our approximation for $w_{m,n}$ given as

$$\begin{aligned}w_{m,n} \approx & \ \frac{1}{Lr}\Big[\tilde{R}^M(m,n) + \tilde{R}^M(m + \tfrac{L}{2}, n + \tfrac{L}{2}) \\ & + i\left(\tilde{R}^M(m, n + \tfrac{L}{2}) - \tilde{R}^M(m + \tfrac{L}{2}, n)\right)\Big].\end{aligned} \tag{B.27}$$

B.11.2 Calculation of $w_{n,m}(a_1)$

This computation is a little tricky so we include some of the details here. Looking closely at (11.31) we know $w_{m,n}(1)$, Δ, a_0. We need to calculate

ρ_k and γ_k. It should be clear that the coefficients of ρ_k are described in (11.30), i.e. we see

$$\rho_k = \begin{cases} N w_{N-k,N} & \text{if } k < 0, \\ \frac{N}{2}(w_{-N,-N} + w_{N,N}) & \text{if } k = 0, \\ N w_{k-N,-N} & \text{if } k > 0. \end{cases} \tag{B.28}$$

Next we have to calculate the Fourier coefficients for γ_k, $-N \leq k \leq N$. That is, we calculate

$$\gamma_k = \frac{1}{2\pi} \int_{-\pi}^{\pi} \gamma(\theta) e^{-ik\theta}, \text{ for } -N \leq k \leq N.$$

We have $\gamma(\theta)$ by reciprocating the Fourier series generated by the coefficients in (B.28).

B.11.3 Discussion on units

We are very interested in the units that are outputted from this method, so we should keep careful track of the units that we input into the algorithm. We have current in mA, voltages in mV, and length in meters. Thus when we look at the equation

$$\rho\ (\Omega)(meters) = \frac{Vl}{A}\ \frac{(mVolts)(meters)}{(mAmps)} \tag{B.29}$$

we expect our output to be in Ωm. We want units of mS/m. Therefore, we will take the reciprocal of the resistivity and multiply by 1000,

$$\gamma\ \frac{(mSiemens)}{(meters)} = \frac{1}{\rho} \cdot 1000, \tag{B.30}$$

to get our desired conductivity in the right units.

Appendix C

PRACTICAL DETAILS

C.1 Conductivity Values

Conductivity values are another non-trivial aspect of modeling a domain properly. We provide a list of conductivity values in Table C.1 from [27]. The problem of measuring conductivity values is not so easy. Clearly, one cannot measure accurately the conductivity of a human lung when one is alive, and after one passes the conductivity values of human tissue changes within a few hours of death. There is also a dependence on the frequency used to measure the conductivity. Lastly, certain tissues are quite anisotropic, e.g., the heart and muscle. If these tissues are modeled as isotropic not much is known about the error caused by the simplification.

Table C.1: Conductivity values in the human body [27].

Tissue	Frequency	Cond. (mS/cm)
lung (inspiration)	unknown	0.4
lung (expiration)	unknown	1.0
dog lung (inspiration)	100kHz	0.65
dog lung (expiration)	100kHz	0.82
heart (longitudinal)	unknown	6.3
heart (transversal)	unknown	2.3
bone	unknown	0.06
human thorax (bone)	Low	0.063
" (dog-longitudinal)	d.c. pulse 0.1sec	3.97
" (dog-transversal)	d.c. pulse 0.1sec	1.78
skel. muscle(dog-ave)	Low	1.053
" (longitudinal)	Low	3.333
" (transverse)	Low	0.625
fat	unknown	0.36
fat	1Mhz	0.459
fat	200Mhz	0.2-2/3
blood	unknown	6.7
blood	1kHz	6.06
blood	120kHz	6.49

C.2 Calculating chest boundary function

We use a Fourier series in order to construct a parameterized boundary from the measure data. The details of the derivation were found in Hemant Jain's PhD thesis [40] and are additionally shown below. Let us take M terms for the Fourier series. Then $r(\theta)$ is given as,

$$r(\theta) = r_0 + \sum_{m=1}^{M} (a_m^c cos(m\theta) + a_m^s sin(m\theta)) \tag{C.1}$$

Denote the unknown parameters by vector $\vec{a}$, i.e.

$$\vec{a} = [r_0 \quad a_1^c \quad a_2^c \cdots a_M^c \quad a_1^s \quad a_2^s \cdots a_M^s]^T$$

Now, $r(\theta)$ can be represented in the vector form,

$$r(\theta) = [1 \quad cos(\theta) \quad cos(2\theta) \cdots cos(M\theta) \quad sin(\theta) \quad sin(2\theta) \cdots sin(M\theta)]\vec{a} \tag{C.2}$$

An error functional is defined as follows,

$$e(\vec{a}, \vec{r}^{meas}) = \sum_{n=1}^{N} (r(\theta_n) - r_n^{meas})^2 \tag{C.3}$$

This error function can be minimized with respect to $\vec{a}$ which gives the following matrix equation,

$$[Q][Q]^T \vec{a} = [Q]\vec{r}^{meas} \tag{C.4}$$

Here $[Q]$ is a $(2M + 1)$xN matrix which is obtained from the measured angles $\vec{\theta}$. It is defined as follows,

$$[\mathrm{Q}] = \begin{bmatrix} 1 & 1 & \dots & 1 \\ cos(\theta_1) & cos(\theta_2) & \dots & cos(\theta_N) \\ cos(2\theta_1) & cos(2\theta_2) & \dots & cos(2\theta_N) \\ \vdots & \vdots & & \vdots \\ cos(M\theta_1) & cos(M\theta_2) & \dots & cos(M\theta_N) \\ sin(\theta_1) & sin(\theta_2) & \dots & sin(\theta_N) \\ sin(2\theta_1) & sin(2\theta_2) & \dots & sin(2\theta_N) \\ \vdots & \vdots & & \vdots \\ sin(M\theta_1) & sin(M\theta_2) & \dots & sin(M\theta_N) \end{bmatrix}$$

Parameters $\vec{a}$ are computed using the following equation

$$\vec{a} = [[Q][Q]^T]^{-1}[Q]\vec{r}^{meas} \tag{C.5}$$

Thus given our measurements we, after some time tuning to the proper M, have a smooth parameterized boundary of the domain.

Bibliography

[1] A. Adler, R. Guardo, and Y. Berthiaume. Impedance imaging of lung ventilation: Do we need to account for chest expansion. *IEEE Trans. Biomedical Engineering*, 43(4):414–420, 1996.

[2] G. Alessandrini. Stable determination of conductivity by boundary measurements. *Appl. Anal.*, 27(1-3):153–172, 1988.

[3] A. Allers and F. Santosa. Stability and resolution analysis of a linearized problem in electrical impedance tomography. *Inverse Problems*, 7(4):515–533, 1991.

[4] K. Astala and L. Päivärinta. Calderón's inverse conductivity problem in the plane. *Ann. of Math. (2)*, 163(1):265–299, 2006.

[5] D.C. Barber and B.H. Brown. Applied potential tomography. *J. Phys. E.: Sci Instrum*, 17:723–733, 1984.

[6] D.C. Barber and B.H. Brown. Recent developments in applied potential tomography. In *APT Information Processing in Medical Imaging*, pages 106–121. S. L. Bacharach, Dordrecht, 1986.

[7] D.C. Barber and A.D. Seagar. Errors in reconstruction of resistivity images using a linear reconstruciton technique. *Clin. Phys. Physiol. Meas.*, 9:101–104, 1988.

[8] R. Beals and R.R. Coifman. Scattering, transformations spectrales, et equations d'evolution non lineaires. *I,II, Seminaire Goulaouic-Meyer-Shwartz*, Expose 22, 1980-1.

[9] R. Beals and R.R. Coifman. The D-bar approach to inverse scattering and nonlinear evolutions. *Phys. D*, 18(1-3):242–249, 1986. Solitons and coherent structures (Santa Barbara, Calif., 1985).

[10] J. Bikowski and J. Mueller. 2d eit reconstruction using calderón's method. *Inverse Problems and Imaging*, submitted.

[11] L. Borcea. Electrical impedance tomography. *Inverse Problems*, 18(6):R99–R136, 2002.

[12] W. Breckon and M Pidcock. Data errors and reconstruction algorithms in electrical impeddance tomography. *Clin. Phys. Physiol. Meas.*, 9:105–109, 1988.

[13] R.M. Brown and G.A. Uhlmann. Uniqueness in the inverse conductivity problem for nonsmooth conductivities in two dimensions. *Comm. Partial Differential Equations*, 22(5-6):1009–1027, 1997.

[14] A.P. Calderón. On an inverse boundary value problem. In *Seminar on Numerical Analysis and its Applications to Continuum Physics (Rio de Janeiro, 1980)*, pages 65–73. Soc. Brasil. Mat., Rio de Janeiro, 1980.

[15] M. Cheney and D. Isaacson. Distinguishability in impedance imaging. *IEEE Transactions on Biomedical eng.*, 39:852–860, 1992.

[16] M. Cheney, D. Isaacson, and E.L. Isaacson. Exact solutions to a linearized inverse boundary value problem. *Inverse Problems*, 6:923–934, 1990.

[17] M. Cheney, D. Isaacson, J.C. Newell, S. Simske, and J. Goble. Noser: An algorithm for solving the inverse conductivity problem. *Int J. Imag Sys Tech*, 2:66–75, 1990.

[18] K-S. Cheng, D. Isaacson, J.C. Newell, and David G. Gisser. Electrode models for electric current computed tomography. *IEEE Trans on Bio Eng.*, 36(9):918–924, 1989.

[19] H. Cornean, K. Knudsen, and S. Siltanen. Towards a d-bar reconstruction method for three-dimensional eit. *Comm. Partial Differential Equations*, 29, 2004.

[20] D. Dobson and F. Santosa. Resolution and stability analysis of an inverse problem in electrical impedance tomography: dependence on the input current patterns. *SIAM J. Appl. Math.*, 54:1542–1560, 1994.

[21] P.M. Edic, G.J. Saulnier, J.C. Newell, and D. Isaacson. A real-time electrical impedance tomograph. *IEEE Trans. Biomed. Eng.*, 42(9):849–859, 1995.

[22] L.C. Evans. *Partial differential equations*, volume 19 of *Graduate Studies in Mathematics*. American Mathematical Society, Providence, RI, 1998.

[23] B. Eyuboglu and T. Pilkington. Comments on distinguishability in electrical impedance tomography. *IEEE Trans. Biomed. Eng.*, 40:1328–1330, 1993.

[24] L.D. Faddeev. Increasing solutions of the schrödinger equation. *Sov.-Phys. Dokl.*, 10:1033–1035, 1966.

[25] E. Francini. Recovering a complex coefficient in a planar domain from the Dirichlet-to-Neumann map. *Inverse Problems*, 16(1):107–119, 2000.

[26] C.S. Gardner, J.M. Greene, M.D. Kruskal, and R.M. Miura. Method for solving the korteweg-de vries equation. *Phys. Rev. Lett.*, 19:1095–1097, 1967.

[27] L.A. Geddes and L.E. Baker. The specific resistance of biological material - a compendium of data for the biomedical engineer and physiologist. *Mde. & Biol. Engng.*, 5:271–293, 1967.

[28] E. Gersing, B. Hoffman, and M. Osypka. Influence of changing peripheral geometry on electrical impedance tomography measurements. *Medical and Biological Engineering and Computing*, 34:359–361, 1996.

[29] E. Gersing and M. Osypka. Eit using magnitude and phase in an extended frequency range. *Physiol. Meas.*, 15:A21–A28, 1994.

[30] D.B. Geselowitz. An application of electrocardiographic lead theory to impedance plethysmography. *IEEE Trans. Biomed. Eng.*, BME-18:38–41, 1971.

[31] D.G. Gisser, D. Isaacson, and J. C. Newell. Theory and performance of an adaptive current tomography. *Clin. Phys. Physiol. Meas.*, 9:A35–A41, 1988.

[32] A. Greenleaf, M. Lassas, and G. Uhlmann. Anisotropic conductivities that cannot be detected by eit. *Phys. Meas.*, 24:413–419, 2003.

[33] L.M. Heikkinen, T Vilhunen, R. West, and M. Vauhkonen. Simultaneous reconstruction of electrode contact impedances and internal electrical properties: Ii. laboratory experiments. *Meas. Sci. Technol.*, 13:1855–1861, 2002.

[34] P. Hua, E.J. Woo, J.G. Webster, and W.J. Tompkins. Iterative reconstruction methods using regularization and optimal current patterns in electrical impedance tomography. *IEEE Trans. on Med. Imag*, 10(4):621–628, 1991.

[35] D. Isaacson. Distinguishability of conductivities by electric current computed tomography. *IEEE Trans. Med. Imaging*, 5:91–95, 1986.

[36] D. Isaacson and M. Cheney. Effects of measurement precision and finite numbers of electrodes on linear impedance imaging algorithms. *SIAM J. Appl. Math.*, 51(6):1705–1731, 1991.

[37] D. Isaacson, J.L. Mueller, J.C. Newell, and S. Siltanen. Reconstructions of chest phatoms by the d-bar method for electrical impedance tomography. *IEEE Trans Med Imaging*, 23(7):821–828, 2004.

[38] D. Isaacson, J.L. Mueller, J.C. Newell, and S. Siltanen. Imaging cardiac activity by the d-bar method for electrical impedance tomography. *Physiol. Mea.*, 27, 2006.

[39] David Isaacson and Margaret Cheney. Current problems in impedance imaging. In *Inverse problems in partial differential equations (Arcata, CA, 1989)*, pages 141–149. SIAM, Philadelphia, PA, 1990.

[40] H. Jain. *Electrical impedance tomography of conductivity and permittivity distributions in arbitrary geometries using regularized algorithms.* PhD thesis, Rensselaer Polytechnic Institute, New York, 1997.

[41] H. Jain, D. Isaacson, P.M. Edic, and J.C. Newell. Electrical impedance tomography of complex conductivity distributions with noncircular boundary. *IEEE Trans. Biomed. Eng.*, 44(11):1051–1060, 1997.

[42] J.P. Kaipio, V. Kolehmainen, E. Somersalo, and M. Vauhkonen. Statistical inversion and Monte Carlo sampling methods in electrical impedance tomography. *Inverse Problems*, 16(5):1487–1522, 2000.

[43] K.Y. Kim, B.S. Kim, M.C. Kim, and Vauhkonen. Image reconstruction in time-varying electrical impedance tomography based on the extended kalman filter. *Meas. Sci Technol.*, 12:1032–1039, 2001.

[44] Y. Kim, J.G. Webster, and Tompkins W.J. Electrical impedance imaging of the thorax. *J. Microwave Power*, 18:245–257, 1983.

[45] K. Knudsen. Reconstruction of less regular conductivities in the plane. *Comm. Partial Differential Equations*, 29, 2004.

[46] K. Knudsen, J. Mueller, and S. Siltanen. Numerical solution method for the dbar-equation in the plane. *Aalborg Univeristy*, 2003.

[47] K. Knudsen and A. Tamasan. A new direct method for reconstructing conductivities in the plane. *Physiological Measurements*, 24, 2003.

[48] R. Kohn and M. Vogelius. Determining conductivity by boundary measurements. *Comm. Pure Appl. Math.*, 37(3):289–298, 1984.

[49] R.V. Kohn and M. Vogelius. Determining conductivity by boundary measurements. II. Interior results. *Comm. Pure Appl. Math.*, 38(5):643–667, 1985.

[50] A. Koksal and B. Eyuboglu. Determination of optimum injected current patterns in electrical impedance tomography. *Physiol. Mea.*, 16:A99–A109, 1995.

[51] V. Kolehmainen, M. Lassas, and P. Ola. The inverse conductivity problem with an imperfectly known boundary. *SIAM J. Appl. Math.*, 66(2):365–383 (electronic), 2005.

[52] V. Kolehmainen, M. Vauhkonen, P.A. Karjalainen, and J.P. Kaipio. Assessment of errors in static electrical impedance tomography with adjacent and trigonometric current patterns. *Physiological Measurement*, 18.

[53] C.J. Kotre. A sensitivity coefficients method for the reconstruction of eletrical impedance tomograms. *Clin. Phys. Physiol. Meas.*, 10:275–281, 1989.

[54] M. Lassas, J. Mueller, and S. Siltanen. Mapping properties of the nonlinear fourier transform in dimension two. *Communications in Partial differential Equations*, 32:591–610, 2007.

[55] J. Lehr. A vector derivation useful in impedance plethysmographic field calculation. *IEEE Trans. Biomed. Eng.*, BME-19:156–157, 1972.

[56] P.C. Mathews. *Vector Calculus.* Springer, New York, 1998.

[57] E. McAdams, J. Jossinet, A. Lackermeier, and F. Risacher. Factors affecting electrode-gel-skin interface impedance in electrical impedance tomography. *Med. Biol. Eng. Comput.*, 34:397–408, 1996.

[58] V. Molebny, W. Lionheart, P. Vovk, Y. Ykytenko, and V. Gouz. Sensor position measurement for electroimpedance tomograph. *Proc. 1st Int. Conf. on Bioelectromagnetism*, pages 177–178, 1996.

[59] J.L. Mueller and S. Siltanen. Direct reconstructions of conductivities from boundary measurements. *SIAM J. Sci. Comput.*, 24(4):1232–1266 (electronic), 2003.

[60] J.L. Mueller, S. Siltanen, and D. Isaacson. A direct reconstruction algorithm for electrical impedance tomography. *IEEE Trans. Med. Imag.*, 21(6):555–559, 2002.

[61] T. Murai and Y. Kagawa. Electrical impednace computed tomography based on a finite element method. *IEEE Trans. Biomed. Eng.*, BME-32:177–184, 1985.

[62] E.K. Murphy, J.L. Mueller, and J.C. Newell. Reconstructions of conductive and insulating targets using the d-bar method on an elliptical domain. *Physiol. Mea.*, 28:S101–S114, 2007.

[63] A.I. Nachman. Reconstructions from boundary measurements. *Ann. of Math. (2)*, 128(3):531–576, 1988.

[64] A.I. Nachman. Global uniqueness for a two-dimensional inverse boundary value problem. *Ann. of Math. (2)*, 143(1):71–96, 1996.

[65] G. Nakamura, S. Siltanen, K. Tanuma, and S. Wang. Numerical recovery of conductivity at the boundary from the localized Dirichlet to Neumann map. *Computing*, 75(2-3):197–213, 2005.

[66] J. Newell, D. Isaacson, and D. Gisser. Rapid assessment of electrode characteristics for impedance imaging. *IEEE Trans. Biomed. Eng.*, 37:735 – 738, 1990.

[67] D. Panescu, J. Webster, and R. Stratbucker. A nonlinear finite element model of the electrode-electrolyte skin system. *IEEE Trans. Biomed. Eng.*, 41:681–687, 1994.

[68] P-O. Person and G. Strang. A simple mesh generator in matlab. *SIAM Review*, 46(2), 2004.

[69] S. Seynejad and H. Fahimi. A new method for finding the exact electrode location and bodyperimeter used for eit. *Proc. 14th Int. Conf. IEEE Eng. Med. Biol. Society*, page 58, 1992.

[70] S. Siltanen. *Electrical Impedance Tomography and Faddeev's Green functions.* PhD thesis, Helsinki University of Technology, Finland, 1999.

[71] S. Siltanen, J. Mueller, and D. Isaacson. An implementation of the reconstruction algorithm of A. Nachman for the 2D inverse conductivity problem. *Inverse Problems*, 16(3):681–699, 2000.

[72] S. Siltanen, J.L. Mueller, and D. Isaacson. Reconstruction of high contrast 2-D conductivities by the algorithm of A. Nachman. In *Radon transforms and tomography (South Hadley, MA, 2000)*, volume 278 of *Contemp. Math.*, pages 241–254. Amer. Math. Soc., Providence, RI, 2001.

[73] S.J. Simske. An adaptive current determination and a one-step reconstruction technique for a current tomography system. Master's thesis, R.P.I, Troy, N.Y., 1987.

[74] E. Somersalo, M. Cheney, and D. Isaacson. Existence and uniqueness for electrode models for electric current computed tomography. *SIAM J. Appl. Math.*, 52(4):1023–1040, 1992.

[75] E. Somersalo, M. Cheney, D. Isaacson, and E. Isaacson. Layer stripping: a direct numerical method for impedance imaging. *Inverse Problems*, 7:899–926, 1991.

[76] J. Sylvester. An anisotropic inverse boundary value problem. *Comm. Pure Appl. Math.*, 43(2):201–232, 1990.

[77] J. Sylvester. A convergent layer stripping algorithm for the radially symmetric impedance tomography problem. *Comm. Partial Differential Equations*, 17(11-12):1955–1994, 1992.

[78] J. Sylvester and G. Uhlmann. A global uniqueness theorem for an inverse boundary value problem. *Ann. of Math. (2)*, 125(1):153–169, 1987.

[79] J. Sylvester and G. Uhlmann. Inverse boundary value problems at the boundary—continuous dependence. *Comm. Pure Appl. Math.*, 41(2):197–219, 1988.

[80] F.C Trigo, R. Gonzalez-Lima, and M.B.P. Amato. Electrical impedance tomography using the extended kalman filter. *IEEE Trans. on Biomed. Eng*, 51(1):72–81, 2004.

[81] G. Vainikko. Fast solvers of the Lippmann-Schwinger equation. In *Direct and inverse problems of mathematical physics (Newark, DE, 1997)*, volume 5 of *Int. Soc. Anal. Appl. Comput.*, pages 423–440. Kluwer Acad. Publ., Dordrecht, 2000.

[82] M. Vauhkonen, P.A. Karjalainen, and J.P. Kaipio. A kalman filter approach to track fast impedance chages in electrical impedance tomography. *IEEE Trans. on Biomed. Eng*, 45(4):486–493, 1998.

[83] P.J. Vauhkonen, M. Vauhkonen, T. Savolainen, and J.P. Kaipio. Three-dimensional electrical impedance tomography based on the complete model. *IEEE Trans on Bio Eng.*, 46(9):1150–1160, 1999.

[84] R.M. West, R.G. Aykroyd, S. Meng, and R.A. Williams. Markov chain monte carlo techniques and spatialtemporal modelling for medical eit. *Physiological Measurement*, 25:181–194, 2004.

[85] E.J. Woo, R. Pallas-Areny, J.G. Webster, and W.J. Tompkins. Using walsh functions in electrical impedance tomography. *Annual International Conference of the IEEE Engineering in Medicine and Biology Society*, 12:124–125, 1990.

[86] E.J. Woo, R. Pallas-Areny, J.G. Webster, and W.J. Tompkins. Using walsh functions in electrical impedance tomography. *Annual Int. Conf. IEEE Eng. in Med. and Bio. Sci.*, 12(1), 1990.

[87] T.J. Yorkey, J.G. Webster, and W.J. Tompkins. Comparing reconstruction algorithms for electrical impedance tomography. *IEEE Trans. Biomed. Eng.*, BME-34:843–852, 1987.